

AD-A184 693

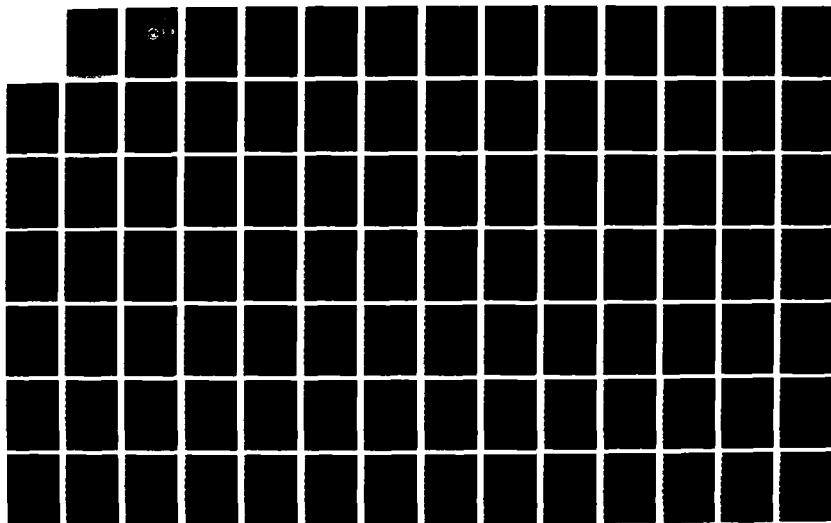
UNDERWATER ACOUSTIC BACKSCATTER FROM A MODEL OF ARCTIC
ICE OPEN LEADS AND PRESSURE RIDGES(U) NAVAL
POSTGRADUATE SCHOOL MONTEREY CA M J BROWNE JUN 87

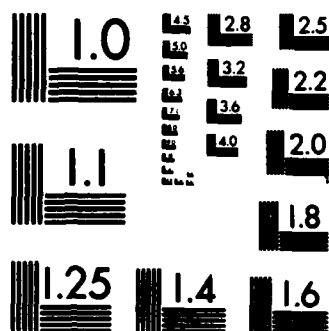
1/2

UNCLASSIFIED

F/G 28/1

NL





MICROCOPY RESOLUTION TEST CHART
NATIONAL BUREAU OF STANDARDS-1963-A

AD-A184 693

DTIC FILE COPY

2

NAVAL POSTGRADUATE SCHOOL

Monterey, California



DTIC
ELECTE
SEP 22 1987
S D
C&D

THESIS

UNDERWATER ACOUSTIC BACKSCATTER
FROM A
MODEL OF ARCTIC ICE OPEN LEADS AND
PRESSURE RIDGES

Michael Joseph Browne

June 1987

Thesis Advisor:

Herman Medwin

Approved for public release; distribution is unlimited.

87 9 15 066

87 9 15 066

REPORT DOCUMENTATION PAGE

1a REPORT SECURITY CLASSIFICATION UNCLASSIFIED			1b RESTRICTIVE MARKINGS		
2a SECURITY CLASSIFICATION AUTHORITY			3 DISTRIBUTION/AVAILABILITY OF REPORT Approved for public release; distribution is unlimited.		
2b DECLASSIFICATION/DOWNGRADING SCHEDULE			5 MONITORING ORGANIZATION REPORT NUMBER(S)		
4 PERFORMING ORGANIZATION REPORT NUMBER(S)			7a NAME OF MONITORING ORGANIZATION Naval Postgraduate School		
6a NAME OF PERFORMING ORGANIZATION Naval Postgraduate School		6b OFFICE SYMBOL (if applicable) 61		7b ADDRESS (City, State, and ZIP Code) Monterey, California 93943-5000	
6c ADDRESS (City, State, and ZIP Code) Monterey, California 93943-5000		8a NAME OF FUNDING/SPONSORING ORGANIZATION		9 PROCUREMENT INSTRUMENT IDENTIFICATION NUMBER	
8b ADDRESS (City, State, and ZIP Code)		8b OFFICE SYMBOL (if applicable)		10 SOURCE OF FUNDING NUMBERS	
				PROGRAM ELEMENT NO PROJECT NO TASK NO WORK UNIT ACCESSION NO	
11 TITLE (Include Security Classification) UNDERWATER ACOUSTIC BACKSCATTER FROM A MODEL OF ARCTIC ICE OPEN LEADS AND PRESSURE RIDGES					
12 PERSONAL AUTHOR(S) Browne, Michael J.					
13a TYPE OF REPORT Master's Thesis		13b TIME COVERED FROM TO		14 DATE OF REPORT (Year Month Day) 1987 June	
15 PAGE COUNT 160					
16 SUPPLEMENTARY NOTATION					
17 COSAT CODES			18 SUBJECT TERMS (Continue on reverse if necessary and identify by block number)		
FIELD	GROUP	SUB-GROUP	Underwater Acoustics, Arctic Ice, Backscatter, Mode Conversion, Diffraction		
19 ABSTRACT (Continue on reverse if necessary and identify by block number)					
<p>The behavior of monostatic backscatter from Arctic open leads and pressure ridges has been studied by using scale models in the laboratory under controlled conditions. The experiments were performed in an anechoic tank using pulsed transmissions from underwater point sources to measure the backscatter from several different floating acrylic plate models. The physical properties of Arctic ice were modeled by the selection of the acrylic material, and the geometrical properties of the ice in features were accurately scaled in the laboratory by maintaining the appropriate dimension-to-wavelength ratios. The characteristic behavior of the</p>					
20 DISTRIBUTION/AVAILABILITY OF ABSTRACT <input checked="" type="checkbox"/> UNCLASSIFIED/UNLIMITED <input type="checkbox"/> SAME AS RPT <input type="checkbox"/> DTIC USERS			21 ABSTRACT SECURITY CLASSIFICATION UNCLASSIFIED		
22a NAME OF RESPONSIBLE INDIVIDUAL Herman Medwin			22b TELEPHONE (Include Area Code) (408) 646-2385		22c OFFICE SYMBOL 61 Md

19. ABSTRACT (continued)

backscatter was explained using both diffraction theory and mode-conversion concepts. It was generally observed that a significant amount of the incident acoustic energy resulted in solidborne vibrations and propagating waves within the floating plate. The ability of those vibrations to reradiate energy into the water resulted in greater backscatter than predicted from the trailing edge of an open lead and piston-like radiation from the pressure ridge models.

Accession For	
NTIS CRA&I	<input checked="" type="checkbox"/>
DTIC TAB	<input type="checkbox"/>
Unannounced	<input type="checkbox"/>
Justification	
By	
Distribution/	
Availability Codes	
Dist	Avail and/or Special
A-1	



Approved for public release; distribution is unlimited.

Underwater Acoustic Backscatter
from a
Model of Arctic Ice Open Leads and Pressure Ridges

by

Michael Joseph Browne
Lieutenant, United States Navy
B.S., United States Naval Academy, 1980

Submitted in partial fulfillment of the
requirements for the degree of

MASTER OF SCIENCE IN ENGINEERING ACOUSTICS

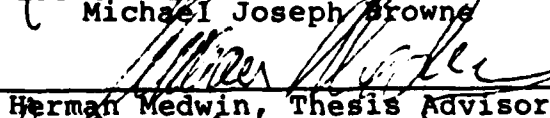
from the

NAVAL POSTGRADUATE SCHOOL
June 1987

Author:

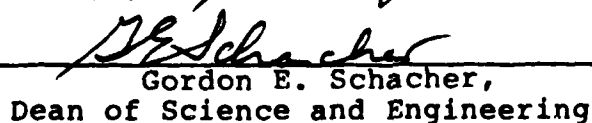

Michael Joseph Browne

Approved by:


Herman Medwin, Thesis Advisor


Robert H. Bourke, Second Reader


Steven L. Garrett, Chairman, Engineering
Acoustics Academic Committee


Gordon E. Schacher,
Dean of Science and Engineering

ABSTRACT

The behavior of monostatic backscatter from Arctic open leads and pressure ridges ^{was} has been studied by using scale models in the laboratory under controlled conditions. The experiments were performed in an anechoic tank using pulsed transmissions from underwater point sources to measure the backscatter from several different floating acrylic plate models. The physical properties of Arctic ice were modeled by the selection of the acrylic material, and the geometrical properties of the ice in features were accurately scaled in the laboratory by maintaining the appropriate dimension-to-wavelength ratios. The characteristic behavior of the backscatter was explained using both diffraction theory and mode-conversion concepts. It was generally observed that a significant amount of the incident acoustic energy resulted in solidborne vibrations and propagating waves within the floating plate. The ability of those vibrations to reradiate energy into the water resulted in greater backscatter than predicted from the trailing edge of an open lead and piston-like radiation from the pressure ridge models.

TABLE OF CONTENTS

I.	INTRODUCTION.....	14
II.	RESEARCH FACILITIES AND EQUIPMENT.....	17
	A. OCEAN ACOUSTICS WAVE FACILITY TANK AND LABORATORY.....	17
	B. TRANSMIT AND RECEIVE SYSTEMS.....	20
	1. Hewlett Packard Function Generator, Model 3314A.....	20
	2. Nicolet FFT Wave Analyzer, Model 660 B...	20
	3. Interference Technology Timing Simulator, Model RS-648.....	21
	4. Ithaco Low Noise Pre-Amplifier, Model 1201.....	21
	5. Celesco LC-10 Hydrophone.....	21
	C. SIGNAL PROCESSING EQUIPMENT.....	22
III.	DESCRIPTION OF PHYSICAL MODELS.....	24
	A. MODELS OF SMOOTH ICE AND ARCTIC POLYNYAS.....	25
	B. MODEL OF A PRESSURE RIDGE.....	32
IV.	THEORY.....	36
	A. DIFFRACTION THEORY.....	36
	B. MODE CONVERSION THEORY.....	42
	1. Compressional Waves.....	44
	2. Shear Waves.....	46
	3. Flexural Waves.....	46
V.	FLEXURAL WAVE ATTENUATION.....	48
	A. EXPERIMENTAL PROCEDURE.....	48

B.	RESULTS AND DISCUSSION.....	50
VI.	BACKSCATTER AT A RIGHT ANGLE WEDGE (ARCTIC OPEN LEAD).....	57
A.	BACKSCATTER FROM AN UNDERWATER WEDGE.....	57
1.	Experimental Procedure.....	57
2.	Results and Discussion.....	61
B.	BACKSCATTER FROM THE ARCTIC LEAD.....	64
1.	Experimental Procedure.....	65
2.	Results and Discussion.....	68
C.	MODE CONVERSION STUDY OF A FLOATING PLATE....	79
1.	Experimental Procedure.....	79
2.	Results and Discussion.....	81
VII:	ELEVATION ANGLE DEPENDENCE OF BACKSCATTER FROM A RIDGE.....	89
A.	EXPERIMENTAL PROCEDURE.....	89
B.	"TYPICAL" RIDGE RESULTS.....	97
1.	Horizontal Probe.....	97
2.	Vertical Probe.....	99
3.	Frequency Dependence.....	102
4.	Elevation Angle Dependence.....	105
C.	"LARGE" RIDGE RESULTS.....	109
1.	Horizontal Probe.....	109
2.	Vertical.....	111
3.	Frequency Dependence.....	117
4.	Elevation Angle Dependence.....	121
D.	"STEEP" RIDGE RESULTS.....	124
1.	Horizontal Probe.....	124

2. Vertical Probe.....	129
3. Frequency Dependence.....	132
4. Elevation Angle Dependence.....	132
E. SUMMARY OF RIDGE RESULTS.....	135
1. Horizontal Probe.....	135
2. Vertical Probe.....	136
3. Frequency Dependence.....	137
4. Elevation Angle Dependence.....	138
VIII: CONCLUSIONS.....	140
APPENDIX A: PLANAR TRANSDUCER FOR MODE CONVERSION STUDY.....	144
APPENDIX B: FLEXURAL WAVE THEORY.....	152
LIST OF REFERENCES.....	156
INITIAL DISTRIBUTION LIST.....	158

LIST OF TABLES

TABLE I:	EQUIPMENT LIST.....	18
TABLE II:	COMPARISON OF THE PHYSICAL PROPERTIES OF ARCTIC ICE TO THE ACRYLIC MODEL LABORATORY CONDITIONS.....	26
TABLE III:	COMPARISON OF THE DIMENSIONS OF THE THREE PRESSURE RIDGE MODELS FOR A 1/8" PLATE THICKNESS.....	34
TABLE IV:	SOURCE/RECEIVER POSITIONS FOR THE ARCTIC OPEN LEAD EXPERIMENT.....	71
TABLE V:	PREDICTED AND MEASURED ARRIVAL TIMES FOR PLATE COMPRESSIONAL WAVE RERADIATION.....	84
TABLE VI:	MEASURED HEAD WAVE AMPLITUDES.....	88

LIST OF FIGURES

2.1	Schematic diagram of the signal processing flow path.....	19
3.1	Cross-section of the pressure ridge model.....	34
4.1	Wedge geometry for Equations (4.1) through (4.3).....	38
4.2	Three Biot-Tolstoy wedges of a ridge keel and the time domain impulse response.....	40
4.3	Transmission from one medium to another at oblique incidence.....	45
5.1	Flexural wave speed.....	51
5.2	Attenuation characteristic for 10 kHz.....	53
5.3	Attenuation characteristic for 15 kHz.....	54
5.4	Attenuation characteristic for 20 kHz.....	55
5.5	Attenuation vs. frequency in a 1/8" floating acrylic plate.....	56
6.1	Experimental set-up for the underwater wedge....	59
6.2	Backscattered waveform from an underwater wedge.....	60
6.3	Backscattered waveform from an underwater wedge.....	60
6.4	Diffraction loss from an acoustically non-rigid wedge.....	62
6.5	Experimental set-up for Arctic open lead.....	66
6.6	Sample waveform for the Arctic lead experiment ($f = 46$ kHz).....	69
6.7	Geometry for the Arctic open lead experiment....	70

6.8	Sample waveform for the Arctic lead experiment (f = 78 kHz).....	73
6.9	Vector subtraction of diffraction from the total signal backscattered from the edge of the floating plate.....	75
6.10	BSS due to compressional and shear wave reradiation (f = 46 kHz).....	76
6.11	BSS due to compressional and shear wave reradiation (f = 62 kHz).....	77
6.12	BSS due to compressional and shear wave reradiation (f = 78 kHz).....	78
6.13	Experimental set-up for the mode conversion study.....	80
6.14	Source pressure vs. position.....	83
6.15	Head wave amplitudes for mode conversion experiment.....	87
7.1	Subtraction technique used in backscatter measurements.....	91
7.2	Source/receiver geometry with respect to the pressure ridge model for four experiments.....	93
7.3	Spectral response for a finite wedge.....	95
7.4	Typical received waveform for horizontal probe using "typical" ridge.....	98
7.5	BSS vs. range for probe using "typical" ridge...	100
7.6	Typical received waveform for vertical probe using "typical" ridge.....	101
7.7	BSS vs. depth for vertical probe using "typical" ridge.....	103
7.8	dB (ref mirror) vs. depth for vertical probe using "typical" ridge.....	104
7.9	Geometry for radiation from a rectangular piston.....	106

7.10	Elevation angle dependence of BSS for the "typical" ridge.....	108
7.11	Typical received waveform for horizontal probe using "large" ridge.....	110
7.12	BSS vs. range for horizontal probe using "large" ridge.....	112
7.13	Typical received waveform for vertical probe using "large" ridge.....	114
7.14	Divergence characteristic of diffraction from crest of "large" ridge.....	115
7.15	BSS v. depth for vertical probe using "large" ridge.....	116
7.16	dB (ref mirror) vs. depth for vertical probe using "large" ridge.....	118
7.17	Comparison of two waveforms for vertical probe using "large" ridge.....	119
7.18	Typical received waveform for frequency dependence using "large" ridge.....	120
7.19	BSS vs. frequency for frequency dependence using "large" ridge.....	122
7.20	BSS vs. phase difference frequency dependence using "large" ridge.....	123
7.21	Elevation angle dependence of BSS for the "large" ridge.....	125
7.22	Typical received waveform for horizontal probe using "steep" ridge.....	126
7.23	BSS vs. range for horizontal probe using "steep" ridge.....	128
7.24	Typical received waveform for vertical probe using "steep" ridge.....	130
7.25	BSS vs. depth for vertical probe using "steep" ridge.....	131

7.26	dB (ref mirror) vs. depth for vertical probe using "steep" ridge.....	133
7.27	Elevation angle dependence of the total back- scatter strength for the "steep" ridge.....	134
7.28	Total experimental backscatter compared to diffraction theory.....	140

ACKNOWLEDGEMENT

The writer wishes to express his appreciation to Professor Herman Medwin of the Physics Department, U.S. Naval Postgraduate School, for his encouragement and guidance during the preparation of this thesis; to Professor Robert H. Bourke for sharing his knowledge of the Arctic; to Dr. Becken and Dr. Tancrell of the Raytheon Corporation for making possible the construction of the PVDF transducer; to Mr. Ken Reitzel for his physical insight and assistance in the laboratory; to Mr. George Jaksha for his material and service support; to Kevin Johnson and Pat Denny for the use of some of their figures; and to my wife, Lisa, for her love and understanding during some long hours in the laboratory.

The financial support of the Office of Naval Research is acknowledged.

I. INTRODUCTION

The purpose of this thesis is to examine two particular aspects of underwater acoustic scatter from the Arctic ice canopy. The motivation for this study came from previous laboratory experiments during which some unexplained phenomena were observed.

The method used in this research is to supplement available theory of scatter by the use of scale models constructed of a material that effectively represents the known physical properties of Arctic ice. Understanding sound propagation in the Arctic is important for naval applications. In a recent Naval Postgraduate School thesis by Denny and Johnson (1986), a study of broad scope was made to determine the importance of various characteristics of the ice canopy on the overall level of low frequency backscatter from the ice. In the case of ice ridges and the ice edge at an open lead (or polynyas), the Biot-Tolstoy theory for diffraction from an infinite, rigid wedge was applied in an attempt to predict the amount of energy which would be backscattered from these acoustically significant features of the ice.

The first series of experiments in the present work explore the sound backscattered from the edge of an ice floe

at a polynya. An open lead or polynya in the ice cover is an area where there is no ice. Although definitions vary, leads are generally cracks in the ice of length much greater than the width of the crack, and polynyas are vast areas of open water beyond the edge of an ice floe.

Experiments performed by Denny and Johnson (1986), and independent measurements performed for the purpose of this thesis, have shown that more energy than predicted by the Biot-Tolstoy theory may be backscattered from the ice edge of the laboratory model of a polynya. Evidence will be presented to show Arctic ice and the acrylic ice model are acoustically non-rigid, so some of the sound energy incident on the plate generates solid-borne compressional and shear waves which propagate along the plate and radiate energy back into the water when they reach a discontinuity, such as the end of an ice floe at a polynya. This reradiated energy, when superimposed with the actual diffraction, is the cause of the received backscattered signals being larger than that predicted by theory alone.

The second set of experiments considers the sound backscattered from acrylic models of an ice ridge. The interaction of adjacent ice floes forms pressure ridges in the ice canopy. The thickness of the interacting ice and the magnitude of the compressive and shear forces exerted on the ice floes will determine the size of the keel depth

(below the ice canopy) and the sail height (above the ice canopy). For the laboratory model, the ice ridge is assumed to be a wedge of triangular cross section mounted below an acrylic plate. The sound energy backscattered from a wedge, as described by the Biot-Tolstoy theory, is the superposition of the reradiated energy from each line along the crest of the wedge. The experiments were designed to determine what part of the wedge contributes the predominant backscattered energy, how the size and orientation of the wedge affects the amount of energy which is reradiated, and how reflection, diffraction, and mode-converted energy share in the total backscatter over a range of sound frequencies and incident angles.

II. RESEARCH FACILITIES AND EQUIPMENT

A. OCEAN ACOUSTICS WAVE FACILITY TANK AND LABORATORY

The Ocean Acoustics Wave Facility at the Naval Postgraduate School, previously used in the study of air-water interactions on the ocean surface, contains an anechoic tank in which this experiment was conducted. The tank was large enough to facilitate the use of sinusoidal pulses of energy to measure diffraction without interference from reflections due to the sides or bottom of the tank. The dimensions of the tank are 10 feet in length and width, 9.5 feet in depth. The bottom of the tank and all four sides are lined with redwood absorbing wedges which result in a low noise environment and less reverberation of sound in the tank. Signal averaging was performed using a very short pulse repetition time in order to eliminate the effects of random background noise.

The equipment used in the laboratory is listed in Table I. Figure 2.1 illustrates the equipment set-up used during the performance of both experiments. All of the equipment used is available on the commercial market with the exception of the 12 element polyvinylidene fluoride (PVDF) planar transducer which was designed for future waveguide experiments, but found some application here. The design and operation for the PVDF transducer is described in

TABLE I

EQUIPMENT LIST

<u>Abbreviation</u>	<u>Nomenclature</u>
Timing Simulator	Interface Technology Timing Simulator/Word Generator, Model RS-648
Function Generator	Hewlett Packard Function Generator, Model HP-3314A
Power Amplifier	Hewlett Packard Power Amplifier, Model HP-467A
Source or Receiver	Celeco LC-10 Hydrophone
Pre-Amplifier	Ithaco Low Noise Pre-Amplifier, Model 1201
Nicolet	Nicolet Dual Channel FFT Analyzer, Model HP-465A
Voltage Amplifier	Hewlett Packard Voltage Amplifier, Model HP-465A
Signal Processor	IBM PC/XT with Computerscope ISC-16 Data Acquisition and Analysis Package
Scope	Kikusui Oscilloscope, Model COS 5060

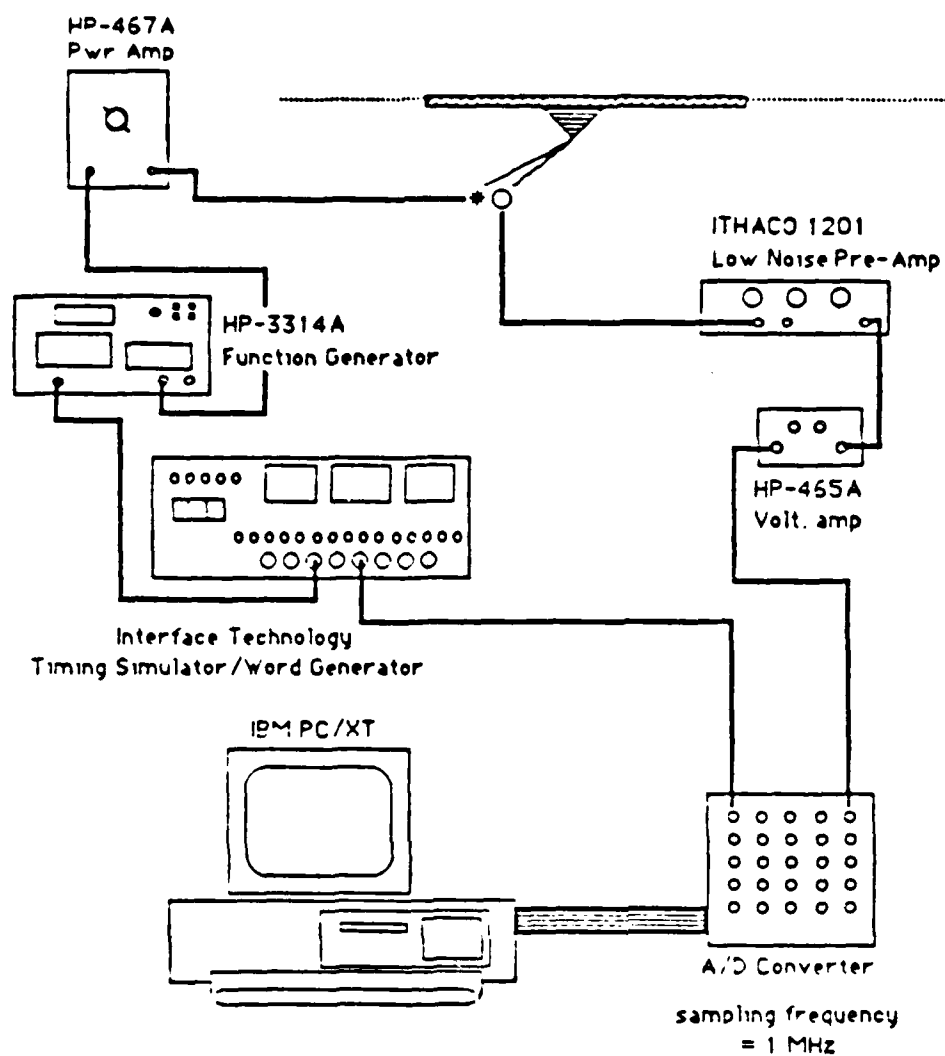


Figure 2.1: Schematic diagram of the signal processing flow path.

Appendix A. Additional information concerning the equipment used for transmitting and receiving acoustic signals, and for performance of the signal processing are described in Sections B and C of this chapter.

B. TRANSMIT AND RECEIVE SYSTEMS

1. Hewlett Packard Function Generator, Model 3314A

The 3314A function generator is a digital, multimode, programmable signal generator with preset Sine, Triangle, and Squarewave functions and programmable arbitrary waveforms. The frequency range is from 1 mHz to 19.99 MHz, and the maximum output voltage is 10 volts zero-to-peak. While using repeated bursts of sound energy for the purpose of signal averaging, the function generator was operated in the N CYCLE MODE, in which N complete cycles of the designated waveform were generated by the function generator at the start of each pulse repetition period.

2. Nicolet FFT Wave Analyzer, Model 660 B

The Nicolet wave analyzer is a self-contained, programmable signal processing system which performs analog to digital conversion internally. The display screen allows real-time observation of either the received time signal or its frequency spectrum. The Nicolet wave analyzer is limited to a sampling frequency of 250 kHz and a time window of 4 msec. When utilized in parallel with the IBM signal processing equipment, the Nicolet was useful for initial detection of the signal of interest.

3. Interface Technology Timing Simulator, Model RS-648

The timing simulator was used to establish the pulse repetition rate used for signal averaging by triggering the function generator, the Nicolet, the Ithaco pre-amplifier, and the signal processing equipment in the proper sequence. The timing simulator has the ability to produce TTL pulses sufficient for a 50 nanosecond timing resolution.

4. Ithaco Low Noise Pre-Amplifier, Model 1201

The Ithaco pre-amplifier provided the filtering and amplification necessary to detect the small magnitude, coherent transient signals backscattered from different features of the acrylic ice model. Signal filtering in the bandpass range of 3 kHz to 100 kHz helped to reduce the level of background noise, and signal amplification at gains ranging from 100 to 10,000 times magnification permitted detection of even the smallest signals which were reradiated from the model.

5. Celesco LC-10 Hydrophone

Celesco LC-10 hydrophones were used both as transmitters and receivers. The LC-10 hydrophone is small enough to simulate a point source of sound, in which $ka \ll 1$ (where k = wave number, a = linear dimension of the transducer). The LC-10 hydrophone has a fast response; transducer rise and decay times are short enough to permit detection of short pulsed signals free of transducer reverberation or ringing. Short duration pulses were used

to ensure that received signals from propagation paths of similar length would be separable in time and free of unwanted interference. The LC-10 also has the advantage of a flat free-field voltage response and an omnidirectional directivity pattern within ± 2 dB over a frequency range of 30 kHz to 100 kHz. When measuring the relative amplitude of different signals at a given frequency, it was not necessary to know the absolute calibration of the hydrophone. The LC-10 does have low output power, but this disadvantage was not a limitation because the hydrophone was used at short ranges in a low ambient noise environment.

C. SIGNAL PROCESSING EQUIPMENT

The primary signal processing for the experiment was performed on an IBM PC/XT personal computer using a Computerscope Model ISC-16 Signal Processing system. The Computerscope ISC-16 system is a fully integrated hardware and software package designed to permit the IBM PC to perform as a data acquisition and analysis laboratory instrument. The ISC-16 system contains a 16 channel analog to digital converter, an external instrument interface, and the Scope Driver software. The system can receive 16 channels of data input at an aggregate sampling rate of 1 MHz. Digital conversion with 12 bit accuracy is achieved over an input range of ± 10 volts. The Scope Driver software permits the IBM PC to operate like a digital storage

oscilloscope with the ability to obtain graphical output on a dot matrix printer or an X/Y plotter.

III. DESCRIPTION OF PHYSICAL MODELS

In order to accurately model the way sound in the Arctic Ocean interacts with the ice cover, it was necessary to know the physical properties of the ice and to find a material with similar properties to use in the laboratory. Since information available from the literature of Arctic scientists is extensive (but sometimes conflicting since conditions in the Arctic are so variable) it was possible to compile data for the average material properties in the Arctic. For a model designed to simulate the scattering properties of low frequency sound from the ice canopy, the typical values of the characteristic properties of sea ice are sufficient to acoustically model the backscattering from Arctic ice, since local variations in the ice properties typically extend over lengths small in comparison to a wavelength.

Acrylic was chosen as the material for the model because most of its bulk properties fall within the range of physical properties measured in Arctic sea ice. The longitudinal wave speed and flexural wave speed (scaled for the appropriate thickness), the Poisson ratio, and the characteristic impedance (ρc) for acrylic are all very similar to ice. The acrylic plate density is about 25% too high, and compressional and shear wave attenuations in the

acrylic are higher than in ice, but these differences are acceptable. Table II summarizes the comparison between Arctic ice conditions and the laboratory model of an acrylic sheet floating in a fresh water tank.

A. MODELS OF SMOOTH ICE AND ARCTIC POLYNYAS.

For a scale model to accurately represent the real physical situation, there must exist physical and geometric similarity between the two situations. Physical similarity was assured when acrylic was chosen as the modeling material, since its bulk properties closely resemble those of Arctic ice, as described in the last section. Geometric similarity is achieved by maintaining a constant ratio of wavelengths to thicknesses and distances between the Arctic and the laboratory situations. Medwin et al. (1984) successfully demonstrated the accuracy of this modeling technique, and similarly in this experiment, the ratio of the acoustic wavelength (λ) to the ice thickness (h) must be the same for the Arctic and the laboratory situations.

The low frequency range of interest for sound propagation in the Arctic ocean is 50 to 400 Hz. Assuming a typical Arctic level ice thickness of 2 m, then the 3/8" acrylic plate (9.5 mm) used as a model of smooth ice corresponds to a scale ratio of approximately 200:1.

TABLE II
COMPARISON OF THE PHYSICAL PROPERTIES OF
ARCTIC ICE TO THE ACRYLIC MODEL LABORATORY
CONDITIONS

<u>PROPERTIES</u> CHARACTERISTIC	<u>ARCTIC</u>		<u>LAB</u>	<u>MODEL/ICE RATIO</u>
	RANGE*	TYPICAL**	MODEL***	
1. YOUNG'S MOD E, (Pa x 10 ⁹)	1.7-9.0	4.1	5.3	0.32-1.70
*Weeks, 1976. **Typical value. ***Measured laboratory value.				
2. DENSITY, ρ_2 (kg/m ³)	760-960	930	1148	1.20-1.51
*Ackley et al., CRREL Report 76-18, 1976. **Ackley et al., CRREL Report 76-18, 1976. ***Measured laboratory value.				
3. POISSON'S RATIO, σ	0.30-0.36	0.33	0.316	0.88-1.05
*Schwartz and Weeks, 1977. **Schwartz and Weeks, 1977. ***Measured laboratory value.				

TABLE II (page 2 of 5)

<u>PROPERTIES</u>	<u>ARCTIC</u>		<u>LAB</u>	<u>MODEL/ICE RATIO</u>
	RANGE*	TYPICAL**	MODEL***	
4. BULK COMPRESSIONAL WAVE SPEED (m/s)	2800-3500	3150	2545	0.73-0.91
*Hunkins, 1960. **Hunkins, 1960. ***Measured laboratory value				
5. COMP. WAVE ATTENUATION (α_c) (dB/m), F(kHz)	0.3F-0.05F	0.06F	0.42F	1.41-8.48
*McCammon and McDaniel, 1985. **McCammon and McDaniel, 1985. ***Measured laboratory value.				
6. BULK SHEAR WAVE SPEED (m/s)	1500-1860	1700	1373	0.74-0.92
*Hunkins, 1960. **Hunkins, 1960. ***Measured laboratory value.				

TABLE II (page 3 of 5)

<u>PROPERTIES</u>	<u>ARCTIC</u>		<u>LAB</u>	<u>MODEL/ICE</u> <u>RATIO</u>
	<u>CHARACTERISTIC</u>	<u>RANGE*</u>	<u>TYPICAL**</u>	
	7. SHEAR WAVE ATTENUATION (α_s) (dB/m), F(kHz)	1.8F-0.30F	0.36F	0.47-2.37
	*McCammon and McDaniel, 1985. **McCammon and McDaniel, 1985. ***Measured laboratory value.			
	8. BULK CHAR. IMP. $\rho_2 c_2$, (kg/m ² -s) x 10 ⁶	2.13-3.36	2.93	0.87-1.37
	*Calculated using: $\rho_2 = 760$ to 960 kg/m ³ , and $c_2 = 2800$ to 3500 m/s. **Calculated using: $\rho_2 = 930$ kg/m ³ and $c_2 = 3150$ m/s. ***Calculated using: $\rho_2 = 1148$ kg/m ³ and $c_2 = 2545$ m/s.			
	9. FLEXURAL WAVE SPEED (m/s)	252-2357	898-1270	700-1150
	* Calculated using: $v = (2\pi fh)^{1/2} B$ (m/s), where: $h_{\min} = 0.5$ m, $h_{\max} = 6.0$ m $f_{\min} = 50$ Hz, $f_{\max} = 140$ Hz $B_{\min} = 20.17$ $B_{\max} = 32.44$ where B is the flexural wave constant (m/s) ^{1/2} . **Calculated using $h = 2.0$ m and $B = 25.34$ (m/s) ^{1/2} . ***Calculated using $h = 0.00318$ m and $B = 23.98$ (m/s) ^{1/2} .			
				0.49-2.78

TABLE II (page 4 of 5)

<u>PROPERTIES</u>	<u>ARCTIC</u>		<u>LAB</u>	<u>MODEL/ICE RATIO</u>
	<u>RANGE*</u>	<u>TYPICAL**</u>	<u>MODEL***</u>	
CHARACTERISTIC				
10. FLEXURAL WAVE ATTENUATION (dB/m), F(kHz)	Data not available		1.5F	
***Measured laboratory value.				
11. PLATE THICKNESS, h(m)	0.5-6.0	2.0	0.00318	1.600
*Ackley et al., CRREL Report 76-18, 1976. Wadhams et al., 1985. **Wadhams et al., 1985. ***Measured laboratory value.				
12. THICKNESS/WAVELENGTH h/λ	0.007-0.1	0.09	0.04-0.11	0.4-1.2
*Calculated using $h = 2.0$ m and $f = 50$ to 140 Hz. **Calculated using $h = 2.0$ m and $f = 95$ Hz. ***Calculated using $h = 0.00318$ m and $f = 30$ to 80 kHz.				
13. VEL. RATIO c_2/c_1 (ICE/WATER)	1.94-2.36	2.19	1.72	1.13-1.37
*Calculated using: $c_{\min} = 2800$, $c_{\max} = 3500$ (m/s) $c_{\min} = 1440$, $c_{\max} = 1485$ (m/s)				
Calculated using: $c_1 = 1440$, $c_2 = 3150$ (m/s). *Calculated using: $c_1 = 1481$, $c_2 = 2545$ (m/s).				

TABLE II (page 5 of 5)

<u>PROPERTIES</u>	<u>ARCTIC</u>		<u>LAB</u>	<u>MODEL/ICE RATIO</u>
	<u>RANGE*</u>	<u>TYPICAL**</u>		
CHARACTERISTIC			MODEL***	
14. TEMPERATURE T, °C	(-1.6) to (-1.8)	20		
*Weeks, 1976.				
***Measured laboratory value.				
15. SOUND SPEED c_1 , (m/s)	1440-1485	1440	1481	1.00-1.03
*NAVOCEANO TECHNOTE, 1974.				
**NAVOCEANO TECHNOTE, 1974.				
***Measured laboratory value.				
16. DENSITY ρ_1 , (kg/m ³)	1000-1040	1026	1000	0.96-1.00
*Myers et al., 1969.				
**Myers et al., 1969.				
***Measured laboratory value.				
17. FREQUENCY RANGE OF INTEREST F, (KHz)	0.05-0.14		30-80	600:1

Consequently, for the 9.5 mm plate, the following frequency ratios apply:

Arctic frequency (Hz)	Lab frequency (kHz)
50 Hz	10 kHz
400 Hz	80 kHz

For the 1/8" (3.175 mm) acrylic plate, a similar correspondence results. Also, the scaled wavelength to thickness ratio will be met for the two situations since the speed of sound, c , in water agrees within 2% between Arctic ocean conditions and the fresh water in the laboratory. Then,

$$\text{wavelength } (\lambda) = \text{speed of sound } (c) / \text{frequency } (f)$$

$$\text{and} \quad c_{(\text{arctic})} = c_{(\text{laboratory})}$$

$$\text{so} \quad [h/\lambda]_{(\text{ice})} = [h/\lambda]_{(\text{laboratory})}$$

since the frequency and thickness were scaled by the same factor.

In the low frequency regime, if the roughness elements on the smooth Arctic ice are small compared to a wavelength, they are not acoustically significant and can be ignored. For the same reason, it was not necessary to introduce roughness elements on the acrylic model of smooth ice. The Arctic polynya, the large expanse of open water beyond the edge of an ice flow, was modeled by a single edge of a large acrylic plate. The length of the plate edge was 1.5 m (10 to 80 acoustic wavelengths, depending on the frequency used)

so that the ends of the plate would not interfere with the diffraction from the edge of interest.

Finally, since the density of the acrylic is greater than the density of water, it was necessary to build-up the edge of the plate to keep it afloat. By gluing a 3/8" high lip around the outside edge of the acrylic sheet, the plate resembled a flat-bottomed boat floating on the water. Since the lip was glued to the top side of the plate, the edge of the plate which caused the incident sound to be diffracted was undisturbed.

B. MODEL OF A PRESSURE RIDGE

When pressure ridges are formed by the interaction of adjacent ice floes, the keel depth will naturally be a function of the ice thickness which formed the ridge. The data compiled by Hibler et al. (1972) from visual measurements above the ice, and the submarine underice profiles from below, resulted in a statistical model of pressure ridge keel depths and ice keel spatial density. To ensure that only pressure ridges are considered in the profiles, the data distribution only included pressure ridges which were greater than a predetermined cutoff height or depth. The average pressure ridge keel depth reported, from the set of all ridges greater than 6.1 m, was 9.6 m in the Central Arctic and 11.4 m in the Canadian Archipelago. The average reported spatial distribution of pressure ridges was 4.3 ridges/km in the Central Arctic and 9.6 ridges/km in the

Canadian Archipelago. Unfortunately, no data were reported for the average length of an ice keel. This type of data is not available from submarine underice profiles.

For the purposes of this experiment, three different pressure ridges were built to study the effects of height and slope on the amount of energy backscattered from the ridge. Figure 3.1 shows a cross sectional view of the model for the "typical" pressure ridge, including the significant dimensions and the scaled dimension. It is the same ridge used by Denny and Johnson in their study of the backscatter from a ridge. The dimensional data for all these pressure ridges are presented in Table III. With the "typical" pressure ridge as a reference, the "large" ridge was made with the same slope but twice the height, while the "steep" ridge was made with the same height but twice the slope.

The scaled dimensions of the "typical" pressure ridge were designed to match those of a typical multi-year pressure ridge, while the "steep" and "large" ridges represent possible ridges specifically designed to study the dependence of backscatter on height and slope. Each keel was manufactured by gluing flat strips of acrylic together, then machining the entire piece to the specified dimensions. The ridges were glued to a smooth acrylic sheet using an acrylic solvent (K-Lux™ solvent cement for acrylic).

It is noteworthy that the fabrication of the "steep" and the "large" ridges did not include a ridge sail above the

TABLE III
COMPARISON OF THE DIMENSIONS
OF THE THREE PRESSURE RIDGE MODELS
FOR A 1/8" PLATE THICKNESS

<u>DIMENSION</u>	<u>RIDGES</u>		
	<u>TYPICAL RIDGE</u>	<u>LARGE RIDGE</u>	<u>STEEP RIDGE</u>
Keel Base	2-3/8" (36.2 m)	4-3/4" (72.4 m)	27/32" (18.1 m)
Height	5/8" (9.5 m)	1-1/4" (19.0 m)	5/8" (9.5 m)
Angle	28°	28°	56°
Sail Base	3/4" (11.4 m)	(N/A)	(N/A)
Height	3/16" (2.9 m)	(N/A)	(N/A)
Angle	26°	(N/A)	(N/A)

(Dimensions in parentheses are scaled to the Arctic model assuming a frequency ratio of 600:1.)

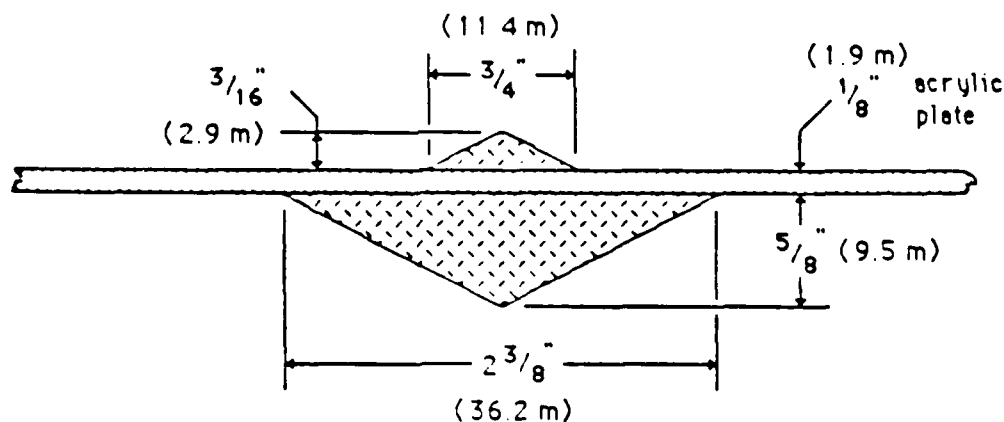


Figure 3.1: Cross section of the pressure ridge model used to measure forward and back scatter from a ridge keel. Dimensions in parentheses are scaled to the Arctic model. All materials are acrylic.

plate. Although the sail is a visually predominant feature in the Arctic (and on the "typical" ridge), it is assumed to be acoustically insignificant for the purpose of diffraction and backscatter from the ice keel. Additionally, it was not necessary to place roughness elements on the faces of the pressure ridges since, for low frequency propagation of sound in the Arctic, the roughness elements are small compared to a wavelength and, therefore, are also assumed acoustically insignificant. This may not be the case and will be examined in future experiments.

IV. THEORY

A. DIFFRACTION THEORY

A physical explanation for the mechanism which causes diffraction is best described using Huygens' principle, as described by Clay and Medwin (1977). Huygens' principle states that each point of an advancing wavefront is a source of secondary waves which move forward as spherical wavelets in an isotropic medium, and the outer surface enveloped by all of the wavelets defines the new wavefront. Consequently, when an acoustic wave interacts with an object in the medium, every point on the object will be the site of an expanding spherical Huygens' wavelet. The wave front that envelopes all of the wavelets spreading from the object is called the diffracted wave.

Biot and Tolstoy (1957) derived a closed-form solution to predict the maximum value of the diffracted energy from an infinite rigid wedge due to an impulse point source of known strength. The expression was simplified by Medwin (1981) to consider a point source delta function turned on at time $t = 0$, and to account for the finite size of the wedge using digital techniques. The result is the simplified expression in cylindrical co-ordinates for the diffracted pressure from a wedge, Equation 4.1:

$$p(t) = [-(S\rho c/4\pi e_w)\{B\}\exp(-\pi y/e_w)]/(rr_0 \sinh y) \quad (4.1)$$

$$\{B\} = \frac{\sin[(\pi/e_w)(\pi \pm \theta \pm \theta_0)]}{1 - 2 \exp(-\pi y/e_w) \cos[\pi/e_w(\pi \theta \pm \theta \pm \theta_0)] + \exp(-2\pi y/e_w)} \quad (4.2)$$

$$y = \cosh^{-1} \left[\frac{c^2 t^2 - (r^2 + r_0^2 + z^2)}{2rr_0} \right] \quad (4.3)$$

The diffracted pressure at time t is $p(t)$, ρ is the density of the medium, c is the sound speed in the medium, S is the source strength. The angle of the wedge measured in the fluid region is e_w , the source coordinates are $(r_0, \theta_0, 0)$ and the receiver coordinates are (r, θ, z) . The term for $\{B\}$ is written for simplicity as $(\pi \pm \theta \pm \theta_0)$, and actually represents the sum of the four possible combinations of $\pm \theta$ and $\pm \theta_0$. Figure 4.1 shows the geometry for the wedge.

For a point source turned on at time $t = 0$, the sound diverges spherically and intersects the ridge first at the least time path, then along the crest of the ridge as the wave diverges. Sound energy diffracts all along the crest of the ridge and propagates to the receiver according to Huygens' principle. The earliest arrival occurs at the least time, τ_0 , given by

$$\tau_0 = [(r + r_0)^2 + z^2]^{1/2} / c$$

Diagram illustrating the Least Time Path for a ray diffracting around a vertical edge. A source on the left emits a ray that reflects off the edge at a point labeled $Z=0$ and reaches a receiver labeled RCYR on the right. The horizontal distance from the source to the reflection point is r_0 , and the horizontal distance from the reflection point to the receiver is r . The vertical distance from the edge to the receiver is z . The path is labeled "Least Time Path".

38

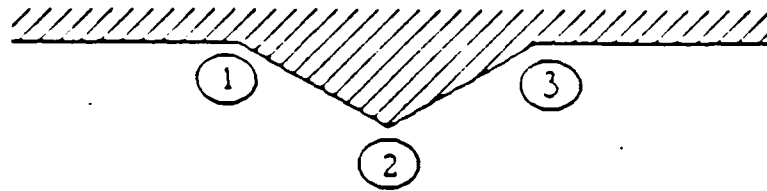
The maximum pressure is received at this least time, while pressure received from other paths falls off exponentially with time corresponding to the greater path length and weaker diffraction at oblique angles.

Novarini and Medwin (1985) demonstrated the use of the "wedge assemblage" method as an accurate way of modeling the diffraction from a conjoint assemblage of rigid or pressure-release crests and troughs. Similarly, the total response for the diffracted pressure from the three Biot-Tolstoy wedges which form the ice keel in the acrylic model will be the linear superposition of three properly timed wedge impulse responses (assuming for simplicity that the wedges are rigid or pressure-release). Figure 4.2 shows the pressure due to three rigid wedges which form the model of the ice keel. The wedges are also assumed to be sufficiently spaced to permit superposition of the individual responses.

In the case of backscatter, the geometry is simplified since $r = r_0$, $\theta = \theta_0$, and $z = 0$. In this case, from Equation (4.3),

$$y(t = \tau_0) = \cosh^{-1} \left[\frac{(r + r)^2 - 2r^2}{2r^2} \right] = \cosh^{-1}(1) = 0$$

(a)



(b)

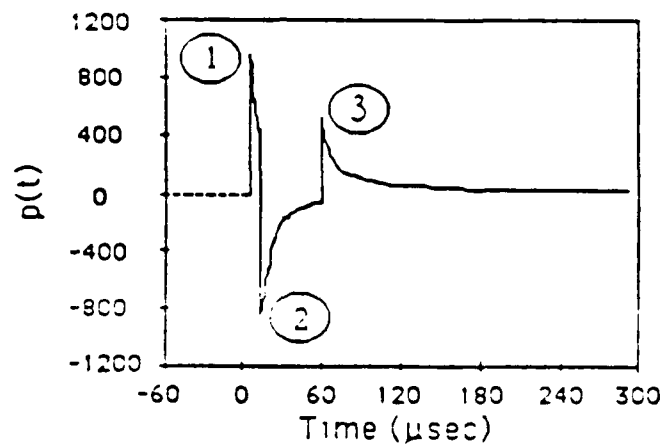
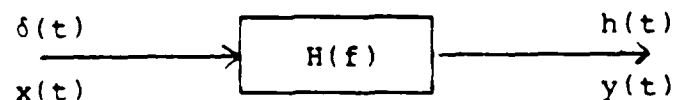


Figure 4.2: (a) Diagram showing the three Biot-Tolstoy wedges that make up the model of the ridge keel. (b) Time domain impulse response calculated using Biot-Tolstoy theory and superposition. Relative times of arrival for a backscattering geometry.

Since $p(t) \propto [\sinh(y)]^{-1}$, $p(t) \rightarrow \infty$ at $t = \tau_0$, as expected. Since digital signal processing is used, Medwin (1982) has shown that, in many cases, the initial impulse can be approximated by a large finite value corresponding to the adjacent sampling interval, Δt :

$$\frac{p(t = \tau_0)}{p(t = \tau_0 + \Delta t)} = 1.366$$

Finally, in spite of the fact that the Biot-Tolstoy theory predicts the diffracted energy from a wedge due to an impulse of sound, the theory can be used to predict the diffracted energy when the input is not an impulse by relying on linear systems theory. If the ice keel is considered to be a linear system whose output is the diffracted pressure, then for an impulse source $\delta(t)$, the diffracted pressure given by the Biot-Tolstoy theory is the impulse response $h(t)$. The transfer function of the filter, $H(f)$, is the fourier transform of $h(t)$.



In the experiments, a pulsed sinusoid $x(t)$ is used as the input instead of an impulse source, so the output diffracted pressure response is the convolution of $x(t)$ with $h(t)$.

$$p(t) = x(t) * h(t)$$

Converting to the frequency domain by the convolution theorem:

$$P(f) = X(f) H(f)$$

As shown by Denny and Johnson (1986), the pressure response in the frequency domain relative to the direct free-field transmission at a reference range R is the filter transfer function times the reference range:

$$P_{REL}(f) = \frac{P_S(f)}{P_{REF}(f)} = \frac{X(f)H(f)}{X(f)/R_0} = H(f)R_0$$

Consequently, for a known input signal to the linear filter $H(f)$, the output response can be obtained relative to the response over a reference distance even if the input was not an impulse.

B. MODE CONVERSION THEORY

When a sound wave interacts with a solid structure, some of the energy may be transmitted from one medium to the other causing longitudinal and transverse vibrations in the solid, and this process is sometimes called mode conversion. As described by Beranek (1971), when steady state is reached, the vibration field will build up to a level at which the power from the source balances the power losses in the system. If a burst of sound interacts with a solid, a similar energy balance can be performed to account for the

disposition of the incident energy which gets reflected, transmitted, or causes vibration in the solid.

For a wave to propagate in a solid, liquid, or a gas, the medium must be capable of alternately storing energy in kinetic and potential forms. Potential energy is stored when part of the medium has undergone elastic deformation; kinetic energy is stored in the movement of particles which have mass. A fluid does not support shear motion, but can undergo compression, so only compressional waves exist in a fluid.

A solid can store energy in both compression and shear, so many different types of waves (representing various combinations of compression and shear) can propagate in a solid. For the flat plate used in the model of the Arctic ice, the solid or body waves of interest are compressional, shear, and flexural waves. A compressional wave is a longitudinal wave in the solid, such that deformations occur parallel to the direction of propagation of the wave, and the potential energy is only stored in compression. A shear wave is a transverse wave in the solid, such that deformations occur perpendicular to the direction of propagation of the wave, and the potential energy is only stored in shear. A flexural wave is a bending wave in which the potential energy is stored in a combination of compression and shear as the plate bends about its neutral axis (where there is no deformation).

1. Compressional Waves

When a compressional wave propagates in a solid body whose dimensions are large compared to a wavelength, the wave will travel at the bulk speed of sound which is dependent only on the material properties of that solid:

$$C_B = \left[\frac{Y(1 - \sigma)}{\rho(1 + \sigma)(1 - 2\sigma)} \right]^{1/2}$$

where Y = Young's Modulus (N/m^2), σ = Poisson's ratio, ρ = density of the material (kg/m^3). For the acrylic, using the values from Table II, $c_B = 2545$ m/sec. By Snell's Law, an incident plane wave at the boundary of the ice-water interface will be refracted into the second medium according to the ratio of the sound speeds. Assuming that Huygens' principle applies, the wavelet initially produced at the acrylic boundary from the incident plane wave in the water responds to the bulk speed in the acrylic since it is unaware of the finite plate thickness, as shown in Figure 4.3. In this case, the critical angle θ_c is

$$\theta_c = \sin^{-1} \left(\frac{c_1}{c_2} \right) = \sin^{-1} \left(\frac{c_w}{c_B} \right) = 37^\circ$$

(grazing angle = 53°)

At this critical angle, the energy transmitted into the acrylic is parallel to the surface, and will propagate as a longitudinal wave at the plate speed given by:

$$C_p = \left[\frac{Y}{\rho(1 - \sigma^2)} \right]^{\frac{1}{2}} = 2257 \text{ m/sec}$$

Similar results occur in an Arctic ice sheet at angles and speeds which maybe determined for the wide range of physical parameters that characterize Arctic ice (see Table II).

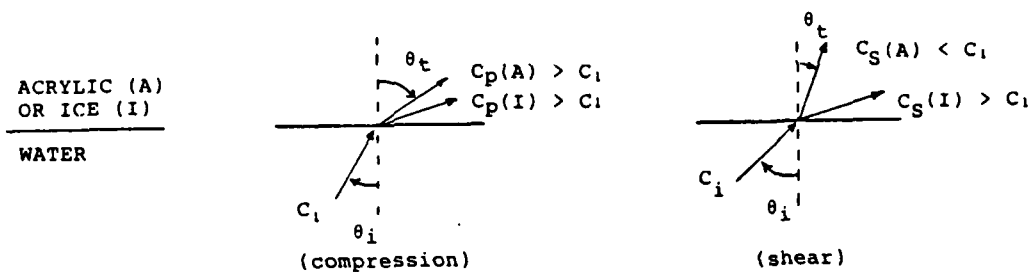


Figure 4.3: Transmission from one medium to another at oblique incidence.

c_i = speed of sound in water
 c_p = compressional wave speed in a plate
 c_s = shear wave speed in a plate
 θ_i = angle of incidence
 θ_t = angle of transmission

(NOTE: Reflected rays, which occur in all cases, are not shown for simplicity.)

2. Shear Waves

A shear wave will be generated in a solid in the same manner described above for compressional waves if the shear speed is greater than the speed of sound in the adjacent medium, which is the case for shear waves in much of the Arctic ice. In the acrylic model, the shear wave speed is less than the speed of sound in water, so refraction into the plate occurs at angles less than the incident angle. (Figure 4.3) Since a shear wave is a transverse wave, optimum excitation of shear waves will occur when the acoustic energy in the water interacts with the floating ice plate or acrylic sheet at normal incidence.

Considering Huygens' principle, for a plane wave in water at normal incidence, the wavelets transmitted into the acrylic cause vibrations perpendicular to the plate surface, resulting in transverse waves that propagate along the plate at the shear wave speed, $c_s = 1373$ m/sec. In the Arctic, the typical shear wave speed is greater than or equal to the speed of sound in water, so shear waves in the ice plate will be excited by the same method described for compressional waves.

3. Flexural Waves

The theory of flexural waves and the derivation of flexural wave phase and group speeds are presented in Appendix B. A few points are in order here pertinent to the study of mode conversion.

When an incident acoustic wave strikes the plate causing vibrations, flexural waves may begin to propagate, in addition to the waves described above. The boundary condition for sound transmission between two media is that the horizontal wave numbers, k_f in the plate, and k_o in the fluid, must be equal to satisfy Snell's Law. When $k_f = k_o$, the compressional wave sound speed in water equals the flexural wave speed in the ice, and the situation is called coincidence. In the case of an acrylic plate or Arctic ice floating on water, the flexural wave speed is always less than the speed of sound in water, so the coincidence condition is never satisfied. Consequently, flexural waves cannot be efficiently generated by an incident acoustic plane wave. However, a source of diverging waves near a plate containing surface roughness elements can generate flexural waves (Denny and Johnson, 1986). As an additional consequence, if a flexural wave is generated in an acrylic or Arctic ice plate, it cannot reradiate energy efficiently back into the water in the form of compressional waves (except perhaps at a discontinuity) since the horizontal wave numbers cannot be matched.

V. FLEXURAL WAVE ATTENUATION

The ineffective transfer of acoustic energy from the waterborne compressional wave to the ice medium in the form of plate flexural waves was studied by Denny and Johnson (1986). They showed that flexural waves could be driven in the plate and could radiate energy back into the water only when the source was very close to the plate. The flexural wave speed was effectively measured in that experiment, but no attenuation measurements were possible. The purpose of this experiment was to measure the flexural wave attenuation.

A. EXPERIMENTAL PROCEDURE

These measurements were made with the smooth floating plate in the anechoic tank to simulate the level ice model. In the flexural wave speed measurements made by Denny and Johnson (1986), an accelerometer mounted on a small square of plexiglass and bonded to the plate using Tackiwax™ provided an effective means of measuring flexural wave speed. While using the accelerometer, the plate-to-receiver efficiency depended on the quality of the bond. In order to measure attenuation, the receiver had to be constantly repositioned to find the decay of the propagating flexural wave over increasing distances. Since the method of using Tackiwax to stick the accelerometer to the plate could not

be duplicated from range to range with a measurable precision, the accelerometer could no longer be used as a receiver.

The receiver used for the attenuation measurements was a Bruel and Kjaer 1/2" condenser microphone. The source used to excite the flexural waves was a 1" cylindrical hydrophone taken from a sonobuoy, and chosen for use because of its flat face which provided an efficient bond with the underside of the plate. The electrical input to the source was 3 cycles of a 200 volt peak-to-peak sinusoid. The frequency range was limited between 10 kHz and 20 kHz: the lower limit was determined by the maximum allowable pulse length for separating signals in time, while the upper frequency was limited by the microphone frequency response roll-off.

The microphone was suspended from a metal rod spanning the plate and was slid across the plate at a height of 2 mm. Three data runs were conducted, one each at 10, 15, and 20 kHz. For the data collected at 10 and 15 Khz, the receiver was positioned at 10 cm intervals between 1.0 and 1.5 m from the source. At receiver ranges less than 1.0 m, the time of arrival of the airborne sound wave generated by the source (travelling at 343 m/sec) interfered with the plate flexural wave (travelling at speeds less than 650 m/sec) for frequencies less than 15 kHz. At 20 kHz, the attenuation was too great for measurements to begin at 1.0 m from the

source, but the faster flexural wave speed (750 m/sec) provided sufficient signal separation to collect data between 0.5 to 1.0 m. Since the measurements were made in air, it was necessary to collect the data at night when the ambient noise conditions were low. The data were collected and processed using a Hewlett Packard 3561A Dynamic Signal Analyzer, by rms time averaging 1000 sample points to determine the received signal level.

B. RESULTS AND DISCUSSION

As revealed by the experiments of Denny and Johnson (1986), the condition for efficient mode conversion between compressional waves in the water and flexural waves in the acrylic plate (or Arctic ice) is never satisfied. For efficient mode conversion, the horizontal component of the wave number must be matched between the plate and the water, but the condition cannot be met since the flexural wave speed is significantly lower than the speed of sound in water at all frequencies. Nevertheless, by using the transverse accelerometer, it is possible to excite flexural waves in the plate, albeit not efficiently.

Figure 5.1 shows the measured flexural wave group speed based on the pulse time of arrival for the three frequencies tested. The measured wave speeds are less than the theoretical flexural wave group speed due to the mass loading effects of the water on the plate, which is unaccounted for on the theoretical curve.

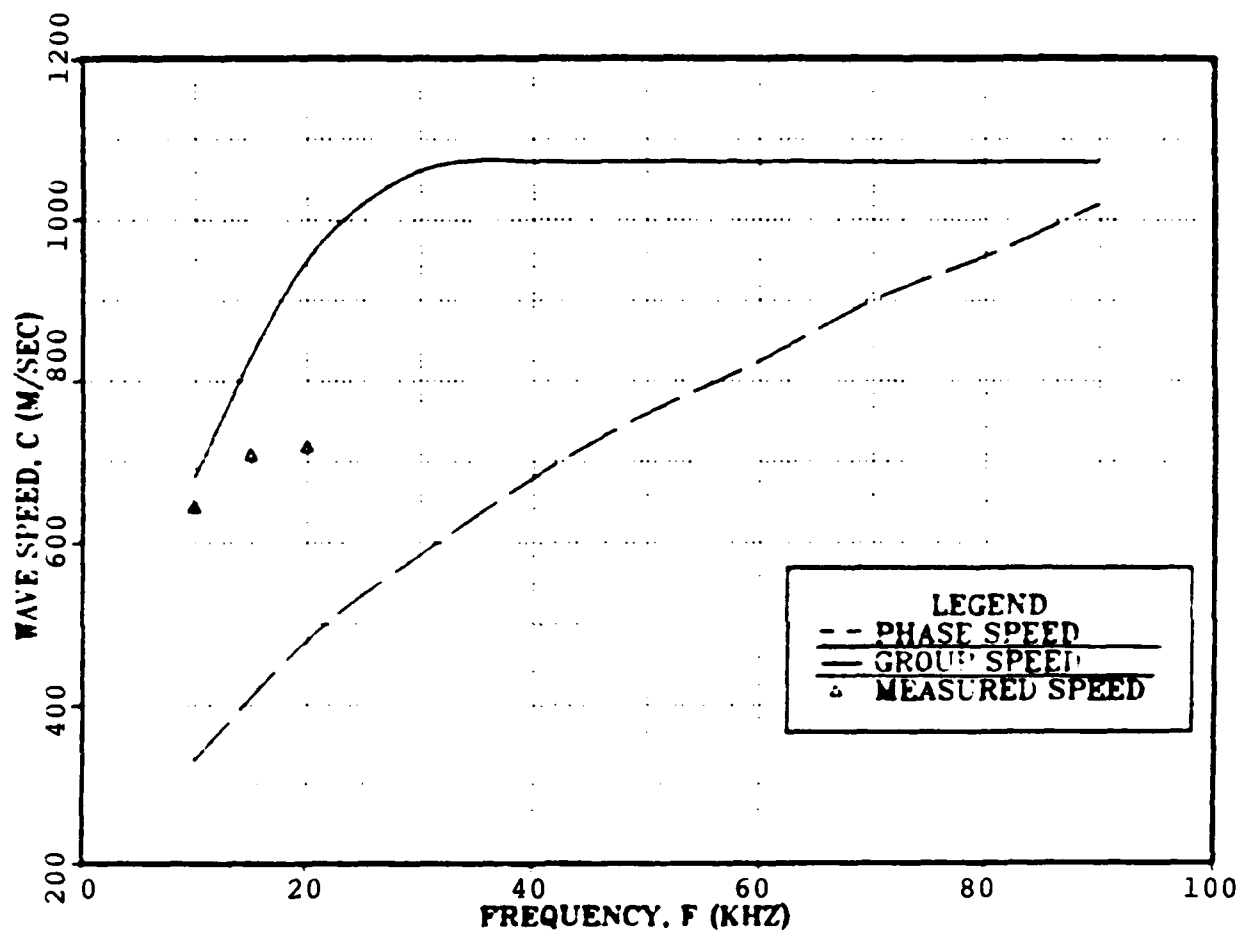


Figure 5.1: Flexural wave speed measured in a 1/8" acrylic plate floating on water.

The attenuation characteristic of the plexiglass was determined by measuring the largest peak-to-peak amplitude of the flexural wave signal, which corresponded to the maximum strength of the flexural wave at that frequency and range from the source. The attenuation (dB/m) for a particular frequency was determined from semi-log plots of received magnitudes versus range, such as in Figure 5.2. Data at longer ranges (e.g., 1.3 m in Figure 5.2) were affected by the noise level and were not considered in the determination of attenuation values. The data obtained at 10, 15, and 20 kHz are plotted on Figures 5.2, 5.3, and 5.4. The cumulative results of those three figures form the attenuation versus frequency curve, Figure 5.5.

The average attenuation of the flexural wave in the acrylic plate was measured to be 1.5 dB/m times the frequency in kHz. Comparison with sea ice values could not be made as no attenuation values could be found in the available literature for Arctic ice flexural waves.

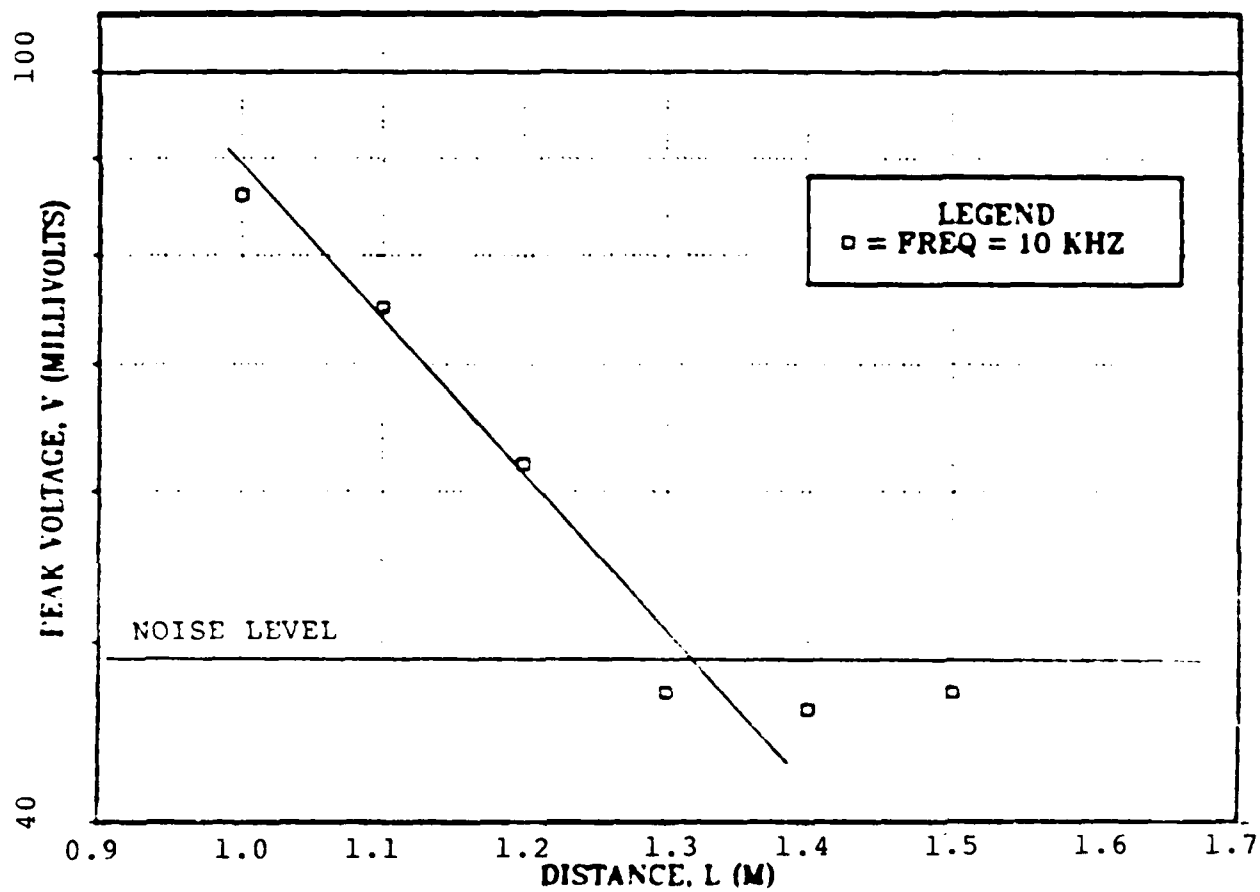


Figure 5.2: Attenuation Characteristic for 10 kHz.

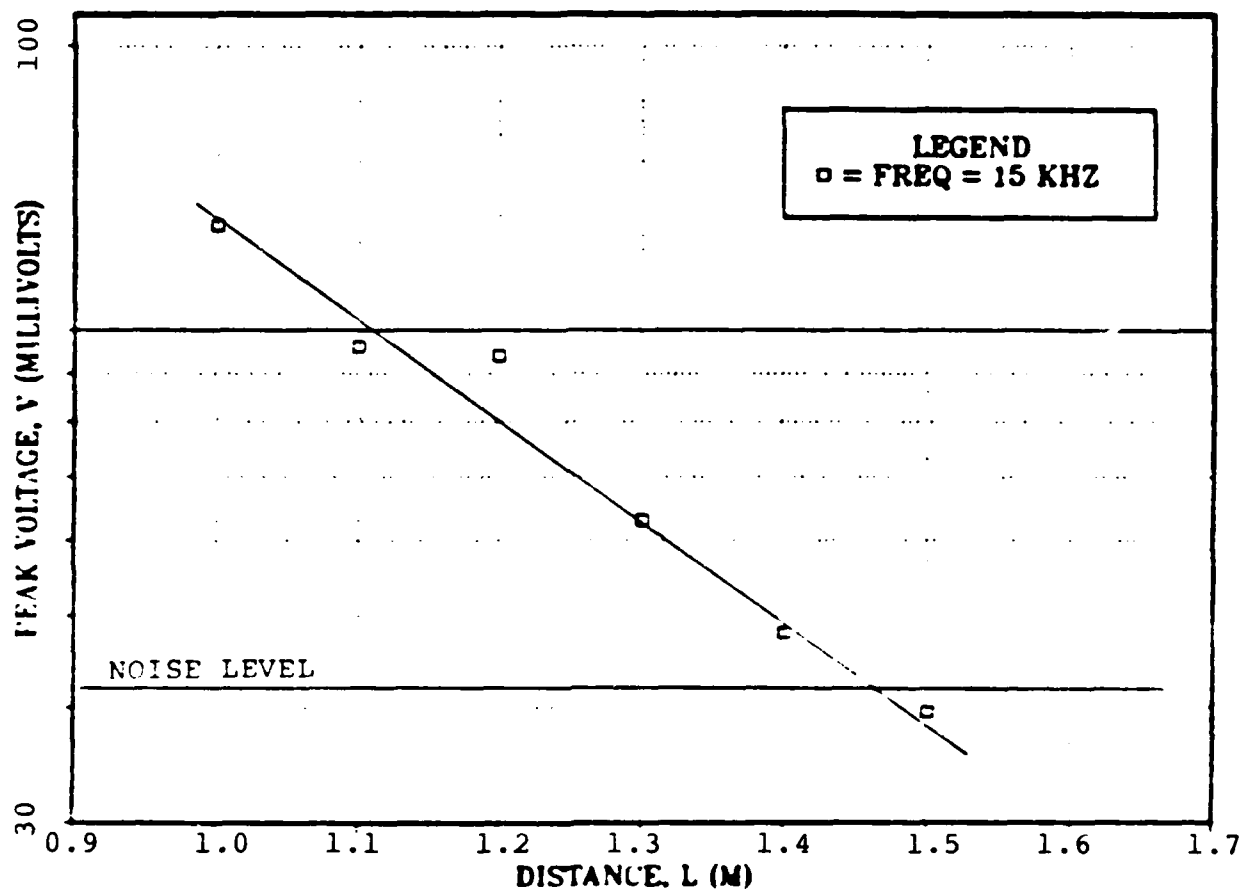


Figure 5.3: Attenuation Characteristic for 15 kHz.

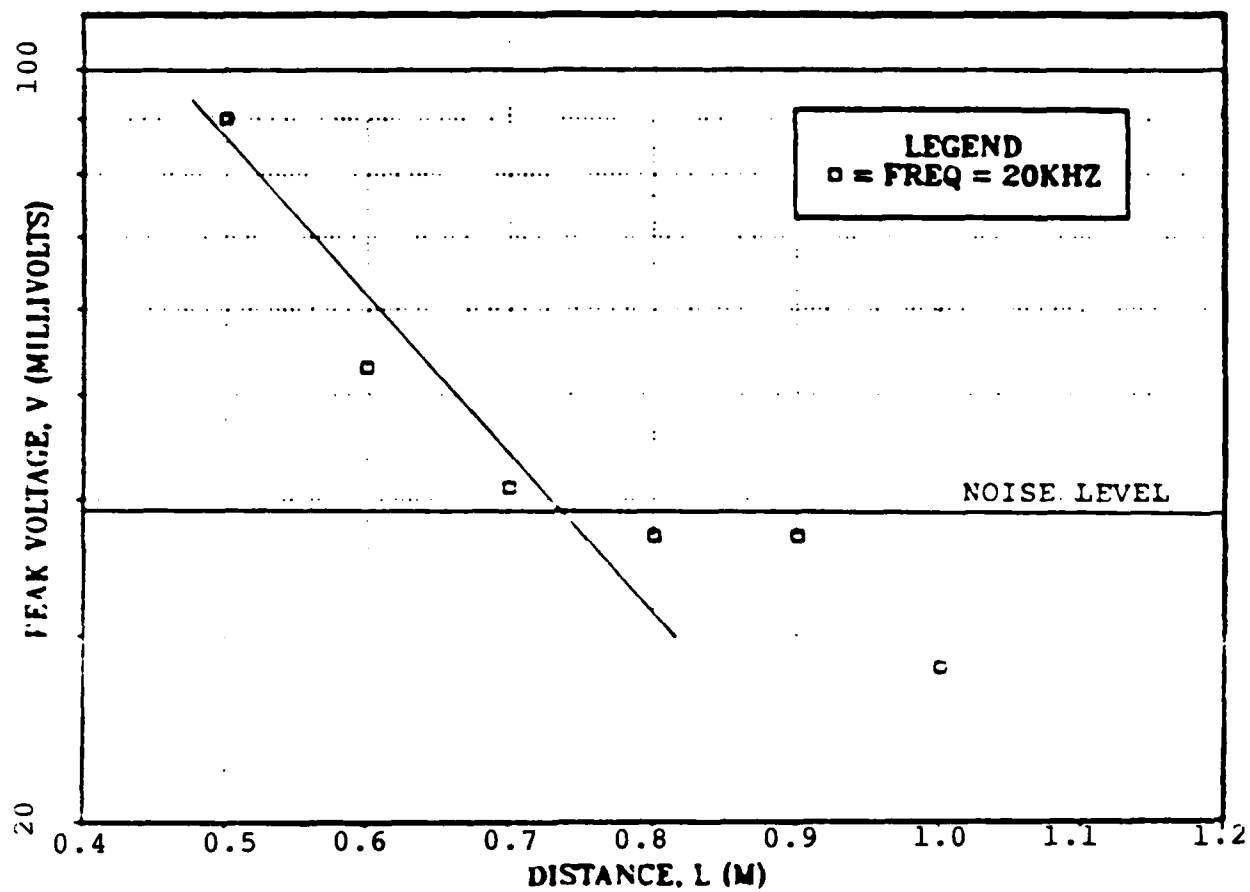


Figure 5.4: Attenuation Characteristic for 20 kHz.

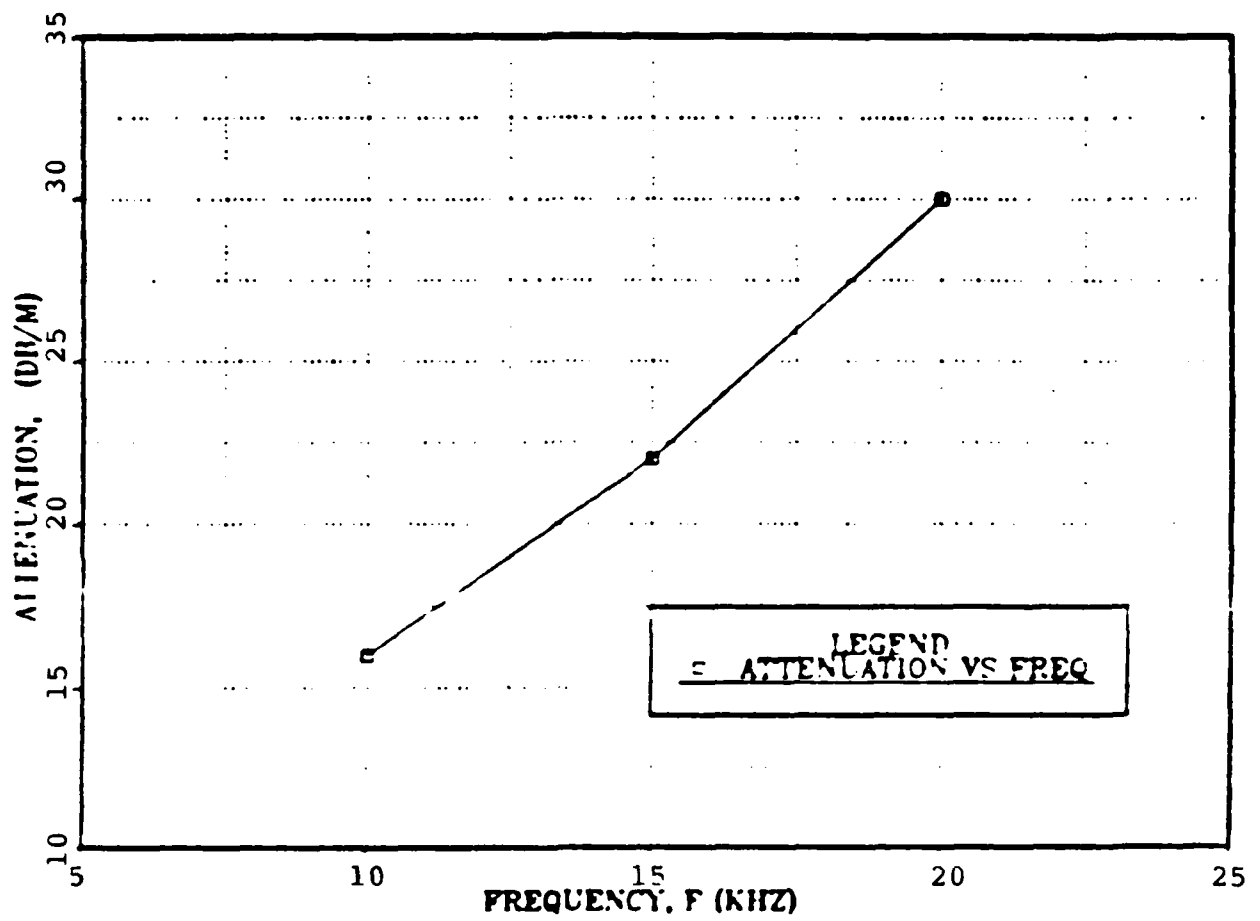


Figure 5.5: Attenuation as a function of frequency for flexural waves in a 1/8" acrylic sheet floating on water.

VI. BACKSCATTER AT A RIGHT ANGLE WEDGE (ARCTIC OPEN LEAD)

A. BACKSCATTER FROM AN UNDERWATER WEDGE

The objective of this experiment was to measure the backscatter from the corner of an acoustically non-rigid, submerged, finite plexiglass wedge, and compare the results with the predictions of the Biot-Tolstoy impulse solution for diffraction of point radiation by an infinite, rigid wedge. Measurements of backscatter from a floating acrylic wedge made by Denny and Johnson (1986) indicated that the Biot-Tolstoy diffraction theory does not accurately predict the amount of backscattered energy. In fact, in some directions more energy was received than predicted, but due to the fact that the acrylic was floating, the effects of the air/water interface near the diffracting corner were unclear. By completely submerging a plexiglass wedge and repeating the measurements, the interactions with the water surface were eliminated so diffraction alone could be measured.

1. Experimental Procedure

The laboratory measurements of the backscatter from the corner of the wedge were performed in the Ocean Acoustics Wave Facility tank described in Chapter II. The wedge

was fabricated out of two pieces of 1/8" plexiglass (70 x 83 cm). Liquid acrylic plastic cement was used to bond the corner of the wedge at a 90° angle; support pieces were cemented to the top and bottom (Figure 6.1). The wedge was suspended vertically in the anechoic tank by four ropes above and was held stationary by two side strings to prevent rotation.

The LC-10 source and receiver were attached to an aluminum rod which was held vertically near the wedge by an extending arm from the side of the tank. Positioning of the source and receiver was accomplished using a 25 cm radius compass marked in 15 increments and centered above the corner of the wedge. The geometry for source/receiver positions was chosen to eliminate interference from undesired edges, since the objective was to measure diffraction only from the wedge corner. The input electrical signal used was 2 cycles of either a 90 or 100 kHz sinusoid. The received diffraction was identified both by its time of arrival and by disturbing the diffracted signal by means of an aluminum sphere placed at the edge. Figure 6.2 shows a typical received waveform, including the direct source-to-receiver path, the specular reflection from the plexiglass plate, and the backscattered signal from the corner of the wedge. Figure 6.3 represents the same geometry with the exception that an aluminum ball has been placed at the edge, and the diffracted signal can be identified by the additional response preceding the diffracted wedge signal.

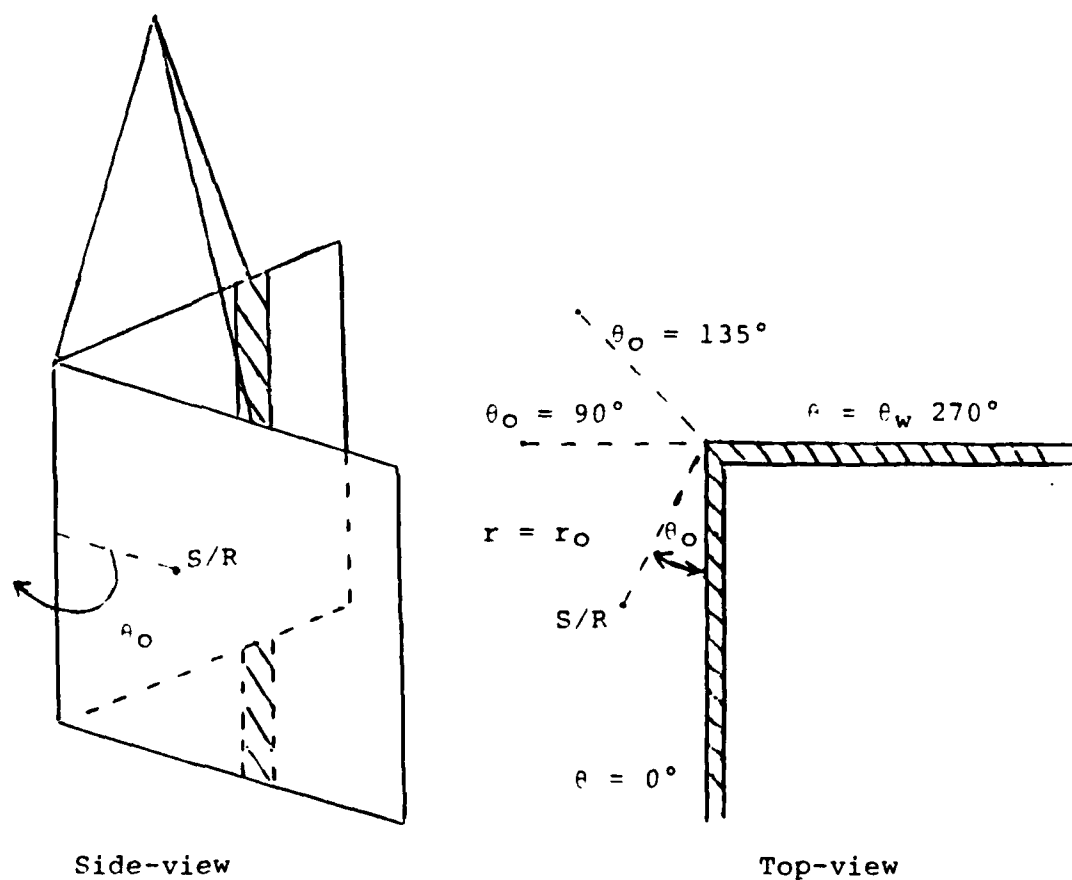


Figure 6.1: Experimental set-up for the underwater wedge. Source/Receiver positioned for monostatic backscatter, ($r = r_0$), ($\theta = \theta_0$). Angle of wedge measured in the fluid region, $\theta_w = 270^\circ$.

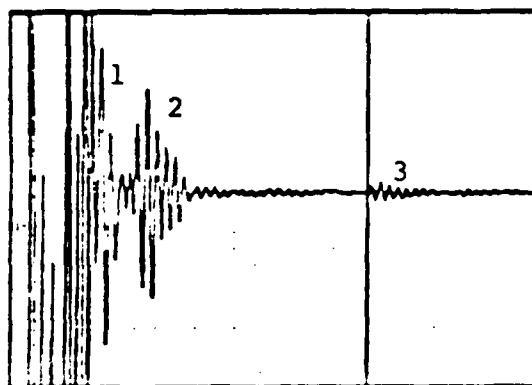


Figure 6.2: Backscattered waveform from an underwater wedge.

- (1) = Direct path between source and receiver
- (2) = Specular reflection from the side of the wedge
- (3) = Diffraction from the edge of interest

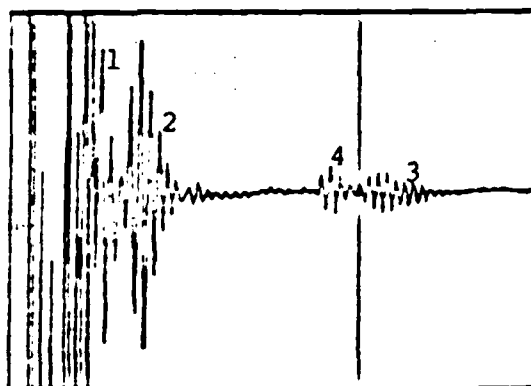


Figure 6.3: Backscattered waveform from an underwater wedge.

- (1) = Direct path between source and receiver
- (2) = Specular reflection from the side of the wedge
- (3) = Diffraction from the edge of interest
- (4) = Diffraction distorted by the aluminum sphere

2. Results and Discussion

Once the backscattered signal was identified, its measurement was simply the maximum peak-to-peak amplitude of the received signal. Backscatter was measured at angles $\theta = \theta_0 = 15^\circ, 30^\circ, 45^\circ, 105^\circ, 120^\circ, 135^\circ$. It was impossible to measure the diffraction between 50° and 95° because the desired signal was hidden by the stronger specular reflection from the plexiglass plate. It was unnecessary to measure the backscatter for angles greater than 135° because of the symmetric geometry. The backscattered signal was identified using the aluminum sphere for each repositioning of the source/receiver.

The results of the measured backscatter are plotted in terms of diffraction loss in dB referenced to spherical divergence over the same $(r + r_0)$ range as a function of angle from the side of the wedge (Figure 6.4). A single theoretical curve for the Biot-Tolstoy predicted diffraction loss from a rigid wedge is plotted for comparison. (A single theoretical curve is sufficient because the predicted diffraction loss at 90 and 100 kHz are almost identical). Notice that the measured backscattered amplitude is greater than predicted for angles corresponding to backscatter from the trailing edge of an ice lead ($\theta = \theta_0 = 15^\circ, 30^\circ, 45^\circ$). Also note that the measured signal is less than predicted for those angles corresponding to large backscatter from the leading edge of an ice lead ($\theta = \theta_0 = 105^\circ, 120^\circ, 135^\circ$).

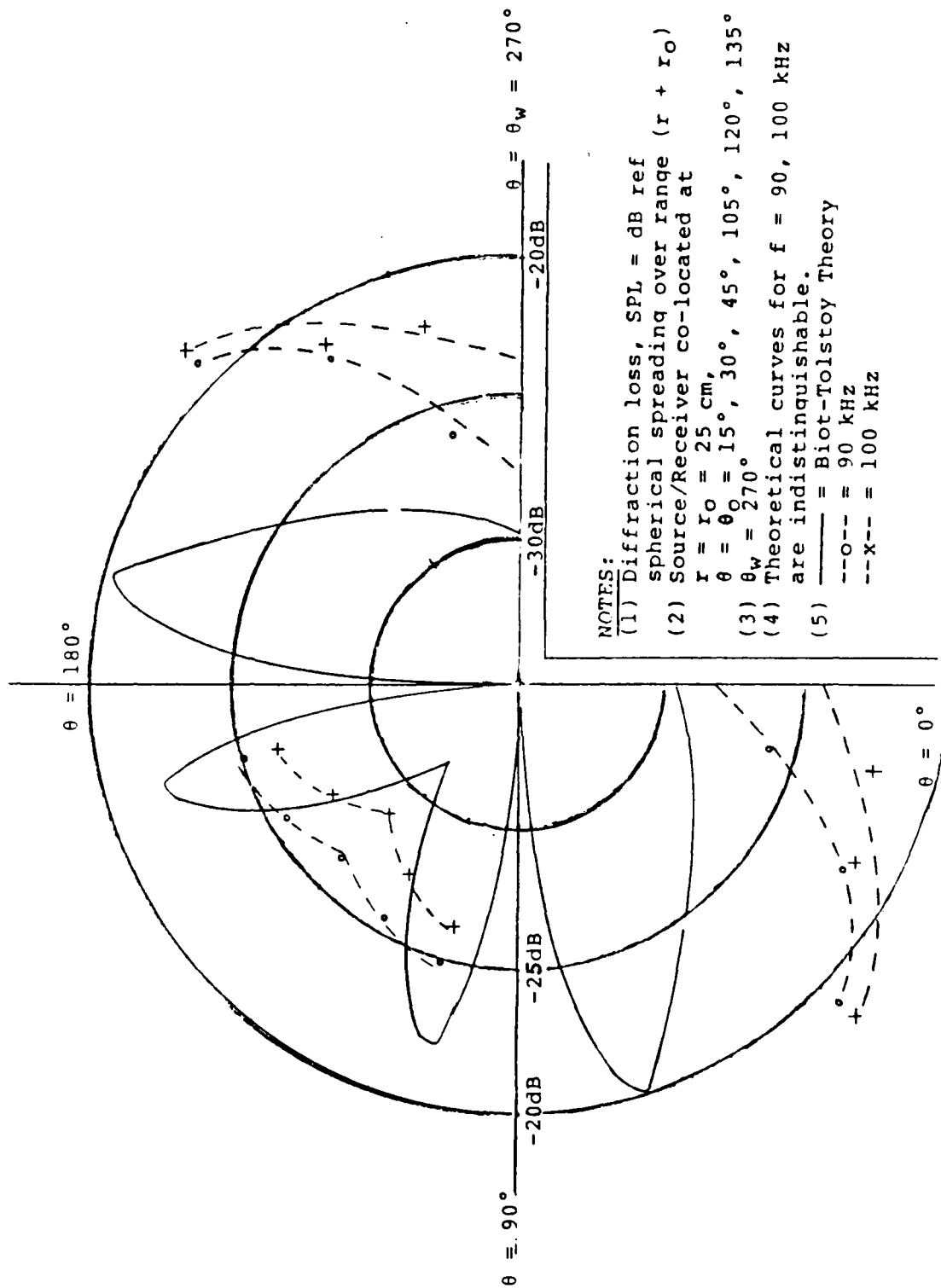


Figure 6.4: Diffraction Loss from an acoustically non-rigid wedge.

The experimental results shown in Figure 6.4 can be explained by the penetrability of the wedge causing mode conversion. For the angles corresponding to backscatter from the trailing edge of an ice lead ($\theta = \theta_0 = 15^\circ, 30^\circ, 45^\circ$), some of the acoustic energy incident on the plate face is mode-converted and causes both longitudinal and transverse vibrations in the plexiglass. Compressional and shear waves propagate in the plate and radiate energy back into the water upon reaching the corner of the wedge. The speeds of propagation are such that compressional wave reradiation occurs at nearly the same time as diffraction from the corner, so a superimposed signal is received which is larger than that predicted by rigid impenetrable diffraction theory alone.

For angles corresponding to backscatter from the leading edge of an ice lead ($\theta = \theta_0 = 105^\circ, 120^\circ, 135^\circ$), some of the incident acoustic energy is again mode-converted into vibrations of the plexiglass wedge. As above, from an energy conservation point of view, less energy is available to be diffracted since mode conversion has occurred. However, in this case, compressional and shear waves propagate along the plexiglass sheets away from the corner, and hence there is no opportunity for reradiation from a discontinuity to be superimposed with the diffraction. Consequently, the measured diffraction is less than predicted.

The finite size of the source and receiver may be one possible explanation for the excess diffraction measured at

$\theta = \theta_0 = 120^\circ, 135^\circ$. A true point source/receiver would be able to measure the actual diffracted pressure in the trough of the theoretical curve, whereas the finite LC-10 source/receiver mounting was 2.3 cm wide at a range of 25 cm, so the acoustic signal was measured over a 5.3° sector centered at $\theta = \theta_0 = 135^\circ$, and not at a point.

B. BACKSCATTER FROM THE ARCTIC LEAD

The experiments performed on the underwater 270° acrylic wedge (Chapter VI, Part A) and measurements made by Denny and Johnson (1986), indicated that during lagging edge backscatter, more energy was received from the edge of an acrylic wedge than was predicted by the Biot-Tolstoy diffraction theory. The difference is due to the mode converted energy which reradiates from discontinuities into the water (in some cases at the same time as diffraction from the plate edge).

The objective of this experiment was to obtain backscatter measurements from the edge of the floating acrylic plate which models a smooth Arctic plate for a point source and receiver positioned monostatically beneath the plate. It is a repeat of one experiment performed by Denny and Johnson (1986), but by judicious choice of source/receiver positions, taking into consideration the theoretical paths and speeds of propagation for the different types of waves, it was possible to separate in time the received

signals corresponding to the diffraction, compressional, and shear waves which radiated from the plate edge back into the water for certain geometries. At the remaining angles, complex phasor subtraction provided the separation.

1. Experimental Procedure

The laboratory measurements of the plate edge diffraction, and of the plate compressional and shear waves which reradiate from the plate edge were made in the Ocean Acoustics Wave Facility tank described in Chapter II. The source and receiver were mounted together on nylon strings threaded through a series of eye screws forming a pulley arrangement. One end of the pulley was fixed at the surface of the water near the center of the tank, while the other end was attached to the bottom of a pole positioned in a vertical guide along one side of the tank. Source/receiver positioning was then accomplished by setting the depth of the pole at one end, and adjusting the pulley mechanism to move the hydrophones along line AB, as shown in Figure 6.5.

The floating acrylic plate was positioned above the source/receiver without disturbing the pulley arrangement, and was held in a fixed position by clamping its outer edges to the sides of the tank. The source/receiver was positioned 60 cm from the plate edge, and subsequent positions were chosen along the same arc of 60 cm radius. The exact position relative to the diffracting edge was determined acoustically by measuring the travel time of the vertically

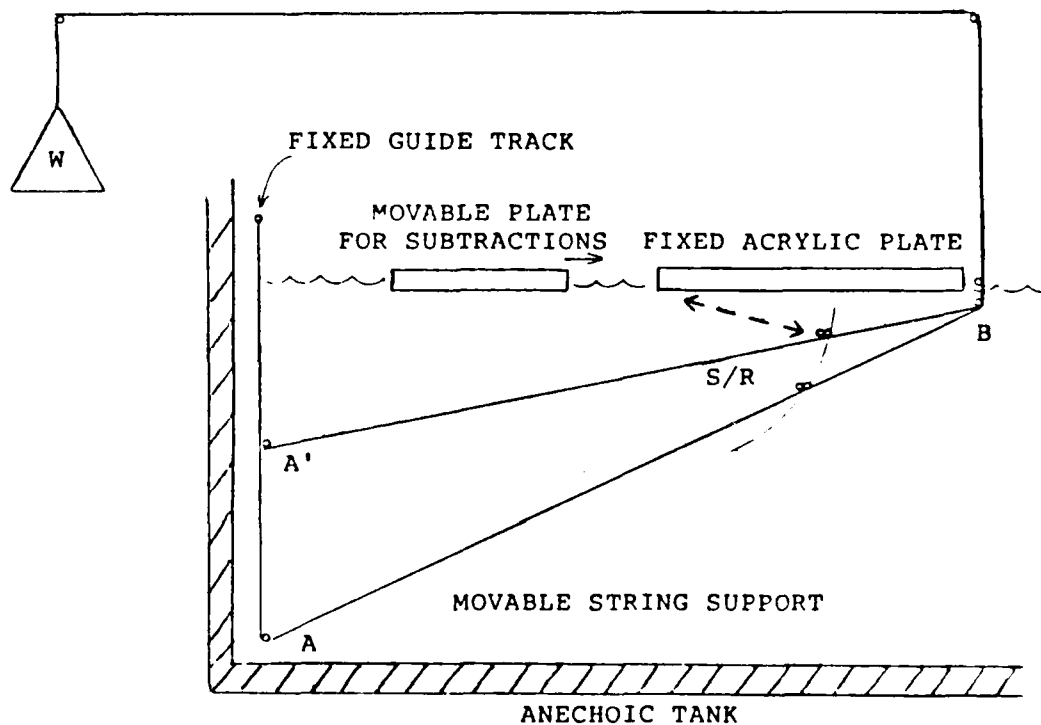


Figure 6.5: Experimental set-up for the Arctic open lead. Source/Receiver positioned for monostatic backscatter, ($r = r_0$), ($\theta = \theta_0$). Two positions are shown.

propagating reflection from the plate and the travel time of the signal which diffracted from the edge of the plate. Once positioned, the source and receiver remained fixed while data were collected for all frequencies of interest.

Since diffraction occurred not only from the plate edge of interest shown in Figure 6.5, but also from the two sides and the back edge of the floating plate, it was necessary to subtract the effects of the three unwanted edges which interfered with the diffraction of interest. By clamping a second, identical plate to the edge of interest, the measurement for the same source/receiver position was repeated without disturbing the first plate. The received signal then obtained contained no diffraction from the edge of interest, and diffraction from the three interfering edges was identical to the initial measurement. By a point-by-point computer subtraction of the two signals (one from the single plate, and one from the plates clamped together), the effect of the three interfering edges was eliminated, and only the diffraction and reradiation from the edge of interest remained. The quality of the computer subtraction depended on two crucial points:

- (a) If the original plate was disturbed during the clamping process, the position of the three interfering edges would be slightly altered, and an imperfect subtraction would result.
- (b) If the two plates were not clamped with the same depth of immersion, a discontinuity would be present at that joint, resulting in a small amount of diffraction and reradiation from the discontinuity.

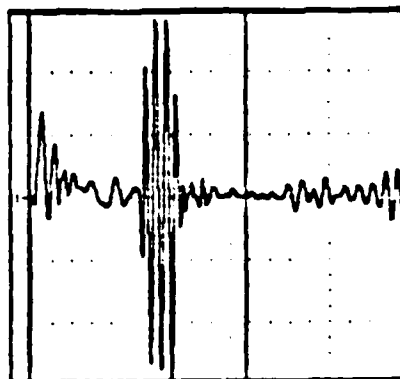
In this case, subtraction would not provide an accurate indication of the diffraction from the edge of the original plate.

Figure 6.6 shows a sample waveform for position R1 and the effectiveness of subtraction for removing reflection and unwanted edge interference from the signals of interest.

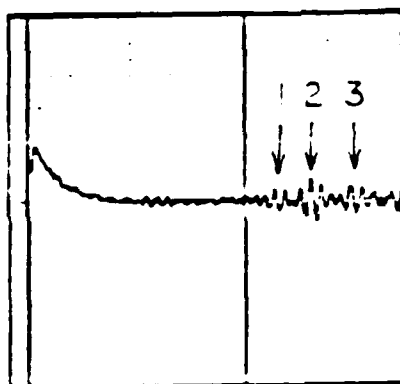
The frequencies chosen for this experiment were those which provided a measurable diffraction from the plate edge, and allowed for simplified signal processing: 3 cycles of a 46.9 kHz sinusoid, 4 cycles of 62.5 kHz, and 5 cycles of 78.1 kHz. The received signal was amplified 100 times and filtered from 3 to 100 kHz by the Ithaco Low Noise Preamplifier, amplified an additional 20 dB, and sent to the analog to digital converter and signal processor. The received time-domain signal was averaged 500 times to eliminate random background noise, and subtracted, as described above, to eliminate the coherent "noise" due to the other three edges. The transient signals of interest were then transformed to the frequency domain using a 64 μ sec time window and a 32-point FFT to obtain their magnitude, since the sampling frequency was 500 kHz.

2. Results and Discussion

Figure 6.7 and Table IV show the geometry and the individual legs of the propagation paths for six source/receiver positions. Using the appropriate values for the speed of sound in water ($c_w = 1481$ m/sec), compressional wave speed in the plate ($c_p = 2257$ m/sec), and the shear



(1.0V scale)



(200 mV scale)

Figure 6.6: Sample waveform for the Arctic lead experiment for $f = 46.9$ kHz. Top picture shows the signal return from the single plate: specular reflection to the left of the cursor, edge diffraction plus interference to the right. Bottom picture shows the subtracted signal after clamping the second plate: specular reflection is eliminated by subtraction, interference is eliminated from the three unwanted edges leaving reradiated signal from the edge of interest.

- (1) = compressional wave reradiation ($t = 680$ μsec)
- (2) = plate edge diffraction ($t = 740$ μsec)
- (3) = plate shear wave reradiation ($t = 830$ μsec)

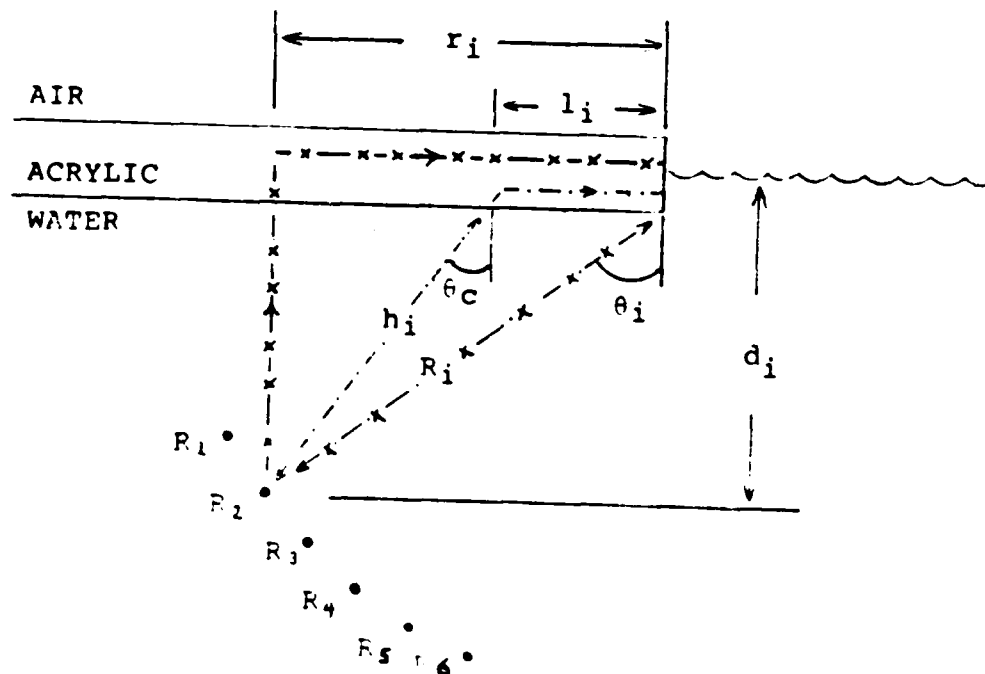


Figure 6.7: Geometry for the Arctic open lead experiment. Source/receiver monostatic backscatter positions $R_1 - R_6$.

θ_c = critical angle for generation of plate compressional waves

- - = path for optimum reradiation of plate compressional wave

- x - = path for optimum reradiation of plate shear wave

TABLE IV
SOURCE/RECEIVER POSITIONS FOR
THE ARCTIC OPEN LEAD EXPERIMENT

	POSITION					
	R1	R2	R3	R4	R5	R6
t_R (μsec)	366	460	540	628	665	693
d_i (m)	0.271	0.341	0.400	0.465	0.493	0.513
t_{TOT} (μsec)	-	838	836	834	-	-
t_C (μsec)	842	-	-	-	-	-
t_d (μsec)	911	-	-	-	825	821
R_i (m)	0.675	0.621	0.619	0.618	0.611	0.608
r_i (m)	0.618	0.519	0.472	0.407	0.361	0.326
θ (deg)	23.7	33.3	40.3	48.8	53.8	57.5
h_i (m)	0.335	0.422	0.494	0.575	0.609	0.634
l_i (m)	0.421	0.271	0.181	0.069	-	-

NOTES:

- (1) A "total" signal is present at positions R2, R3, R4 where the compressional reradiation and diffraction overlap.
- (2) By Snell's Law, compressional signals in the plate can only be generated at positions R1 - R4.
- (3) The diffraction from the plate edge can be measured at position R1 where there is separation from compression, and at R5, R6 where there is no compressional interference.

wave speed ($c_s = 1373$ m/sec), the predicted arrival times for the various propagation paths were calculated using Equations 6.10, 6.11, and 6.12:

$$\text{(Diffracted path)} \quad t_D = 2R_i/c_w \quad (6.10)$$

$$\begin{array}{l} \text{(Optimum path} \\ \text{for compression)} \end{array} \quad t_C = [(h_i + R_i)/c_w] + [l_i/c_p] \quad (6.11)$$

$$\begin{array}{l} \text{(Optimum path} \\ \text{for shear)} \end{array} \quad t_S = [(d_i + R_i)/c_s] + [r_i/c_s] \quad (6.12)$$

A sample waveform with the different separated arrivals is shown in Figure 6.8 where the signals due to the various propagation paths are identified.

For receiver positions R2, R3, and R4 (shown in Figure 6.7), the diffracted energy and the energy reradiated from the plate edge due to the compressional wave were received at nearly the same time, since the higher speed of propagation for the compressional wave offset its greater path length. By expressing each path length in terms of the number of wavelengths travelled by the pulse sound, the path difference corresponded to the relative phase shift between the overlapping arrivals (one wavelength is equivalent to 360° of phase shift). Consequently, the magnitude of the

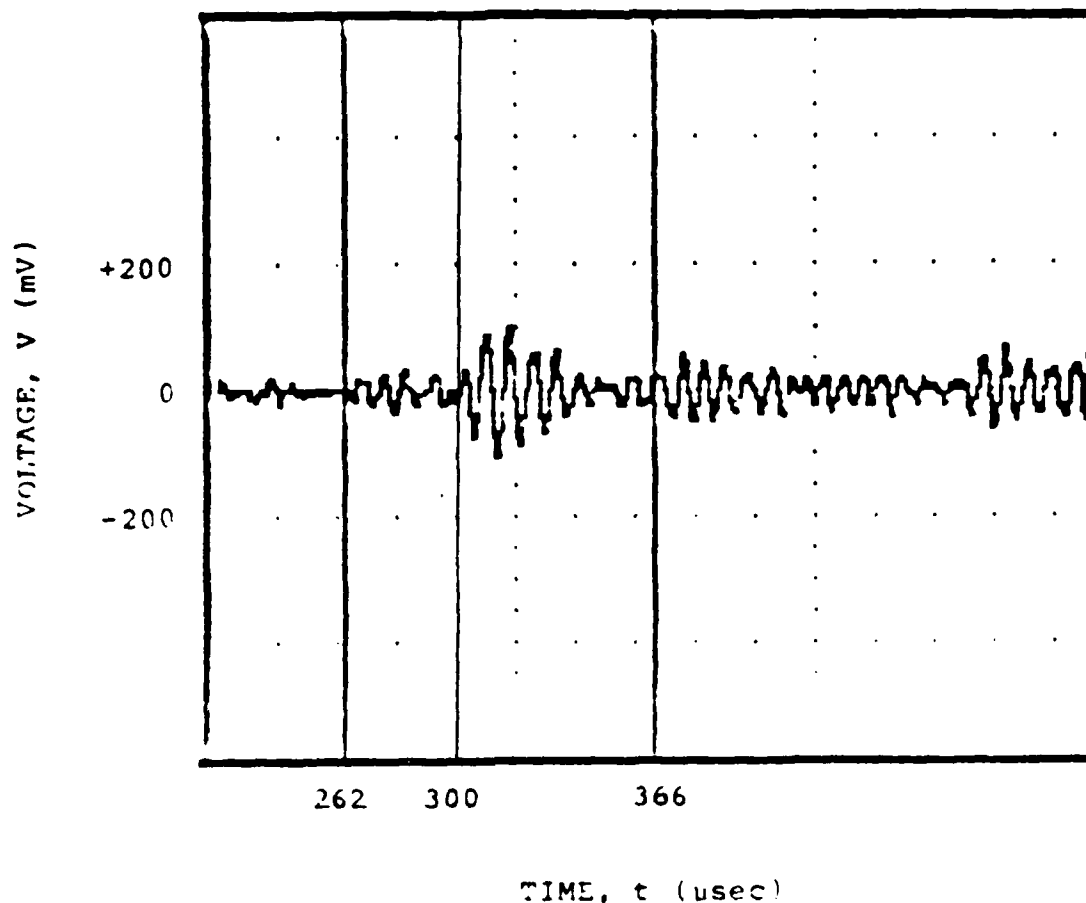


Figure 6.8: Sample waveform at 78 kHz for the Arctic open lead experiment (corresponding to position R1 of Figure 6.7) Starting times are:

- $t = 262 \text{ } \mu\text{sec} \Rightarrow$ Compressional wave reradiation from plate edge
- $t = 300 \text{ } \mu\text{sec} \Rightarrow$ diffraction from plate edge
- $t = 366 \text{ } \mu\text{sec} \Rightarrow$ reradiation from plate edge due to plate shear wave.

(Waveform at the right-hand side of the figure represents interfering noise from a different path.)

compressional wave reradiation could be inferred from a vector addition of signals as shown in Figure 6.9. The phase difference between diffraction and compression was calculated from the difference in path lengths, the magnitude of the diffracted signal was approximated by using the Biot-Tolstoy theory for a single rigid wedge, and the magnitude of the total signal was obtained by transforming the total received transient signal to the frequency domain. The results of these calculations are plotted on the polar diagrams of Figures 6.10 , 6.11, and 6.12. The notes associated with Table IV explain the presence or absence of experimental data points for each source/receiver position. For comparison, the theoretical curve plotted on each figure represents the Biot-Tolstoy predicted diffraction from a rigid wedge.

Observation of the geometries shows that for shallow grazing angles for trailing edge backscatter, it is the compressional path which becomes superimposed with the diffraction; the shear path interferes with diffraction for trailing edge backscatter at nearly normal incidence. Figures 6.10, 6.11, and 6.12 clearly indicate that the Biot-Tolstoy rigid wedge theory, which yields the maximum energy for diffraction, does not account for all of the energy backscattered from the trailing edge of an acoustically non-rigid wedge.

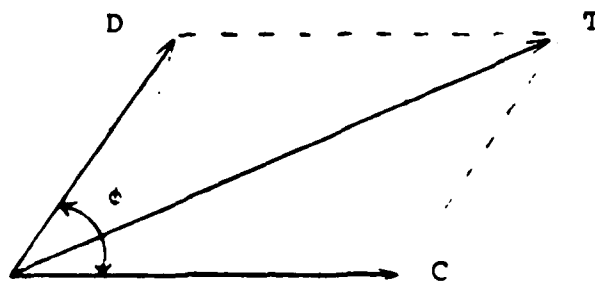


Figure 6.9: Vector subtraction of diffraction from the total signal backscattered from the edge of the floating plate.

T = Total (measured) backscattered signal from the plate edge when compression and diffraction overlap (Positions R2, R3, R4)

C = Compressional signal reradiated from plate edge

D = Theoretical Biot-Tolstoy Diffraction from the plate edge

ϕ = Phase difference between **C** and **D** due to path length difference.

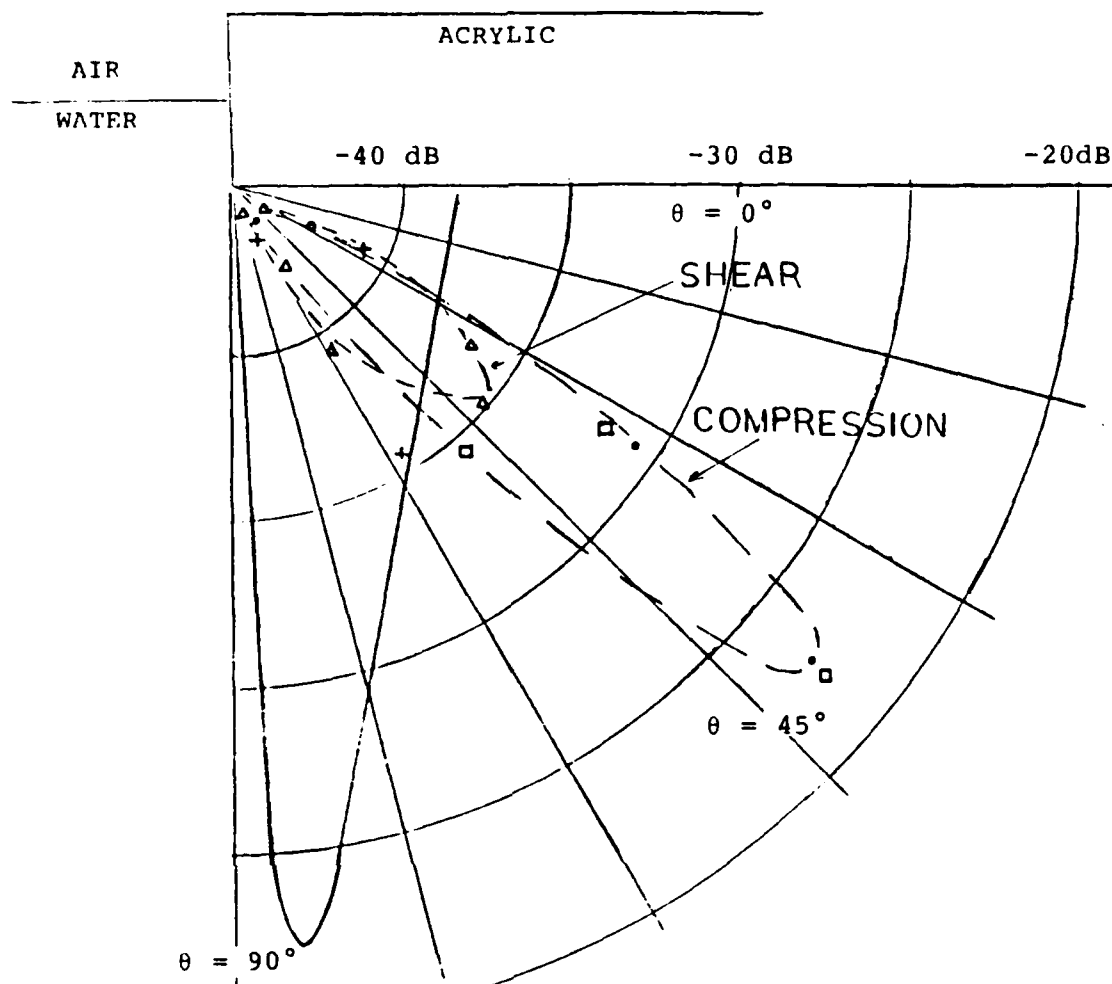


Figure 6.10: BSS due to compressional and shear waves reradiated from an acrylic plate floating on water compared to Biot-Tolstoy predicted diffraction from a single rigid 270° wedge. Frequency, $f = 46.9$ kHz. Diffraction in dB ref spherical spreading over ($r = r_0 = 0.6$ m).

- \square = TOTAL (compression + diffraction)
- \circ = measured compressional wave reradiation
- \bullet = calculated compressional wave reradiation (vector subtraction)
- Δ = measured shear wave reradiation
- \times = measured diffraction
- = Biot-Tolstoy Theory

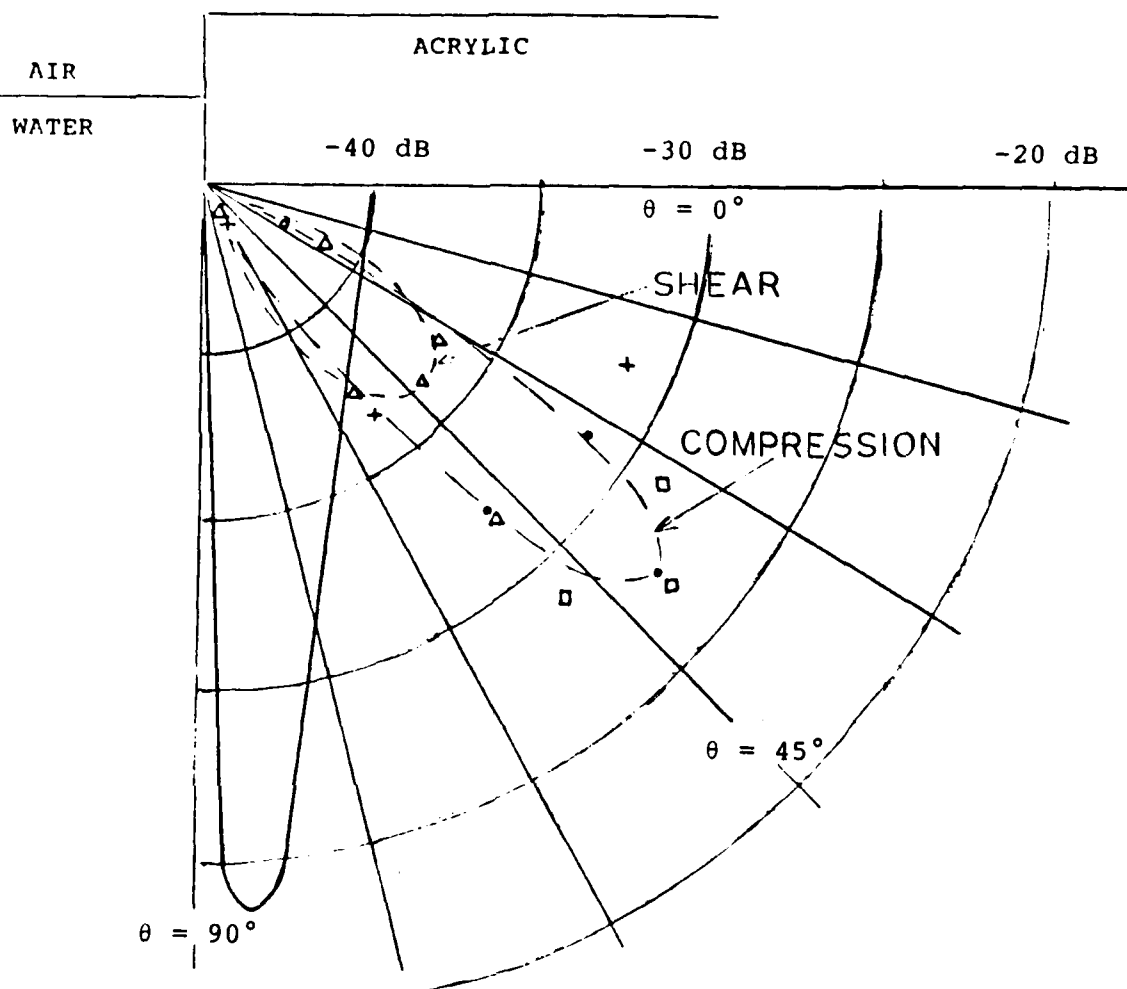


Figure 6.11: BSS due to compressional and shear waves reradiated from an acrylic plate floating on water compared to Biot-Tolstoy predicted diffraction from a single rigid 270° wedge. Frequency, $f = 62.5$ kHz. Diffraction in dB ref spherical spreading over ($r = r_0 = 0.6$ m).

- = TOTAL (compression + diffraction)
- = measured compressional wave reradiation
- = calculated compressional wave reradiation (vector subtraction)
- Δ = measured shear wave reradiation
- x = measured diffraction
- = Biot-Tolstoy Theory

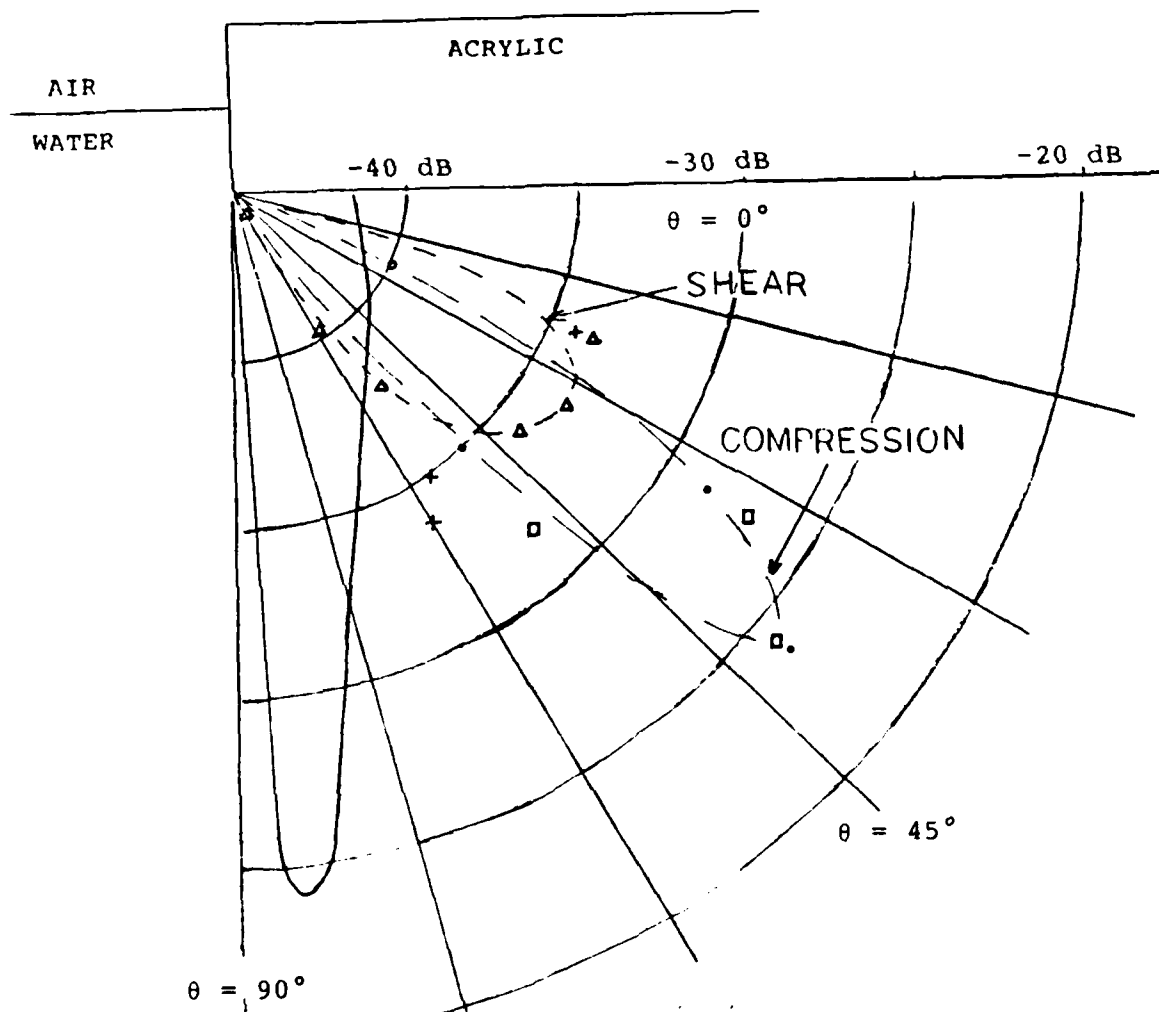


Figure 6.12: BSS due to compressional and shear waves reradiated from an acrylic plate floating on water compared to Biot-Tolstoy predicted diffraction from a single rigid 270° wedge. Frequency, $f = 78.1$ kHz. Diffraction in dB ref spherical spreading over ($r = r_0 = 0.6$ m).

- = TOTAL (compression + diffraction)
- = measured compressional wave reradiation
- = calculated compressional wave reradiation (vector subtraction)
- Δ = measured shear wave reradiation
- x = measured diffraction
- = Biot-Tolstoy Theory

C. MODE CONVERSION STUDY OF A FLOATING PLATE

After the experiment described in Section B successfully generated compressional and shear waves in the floating plate which reradiated from the plate edge separately from the diffraction, the following experiment was devised to study the effects of plate compressional wave reradiation alone. Recall that, for some source/receiver positions in the previous experiment, the compressional reradiation and diffraction overlapped, and the magnitudes of each were identified by the vector subtraction of the arrivals.

1. Experimental Procedure

Figure 6.13 shows the experimental set-up. The source used was the PVDF plane wave transducer described in Appendix A, suspended beneath the floating plate at different angles of incidence with the acrylic surface. The receiver was an LC-10 hydrophone positioned beneath the opposite edge of the plate by an extending arm from the side of the tank. Diffraction from the receiver end of the plate was prevented by inserting a sound reflecting barrier in the direct path between the source and the receiver. The barrier was a 1" thick sheet of Celotex™, covered by a thin sheet of plastic to prevent water penetration and weighted down with 50 pounds of lead to achieve slight negative buoyancy. Celotex, a semi-rigid polyisocyanurate foam-board insulation, has closed pores filled with air, and provided a vertical "pressure-release" boundary beneath the center of

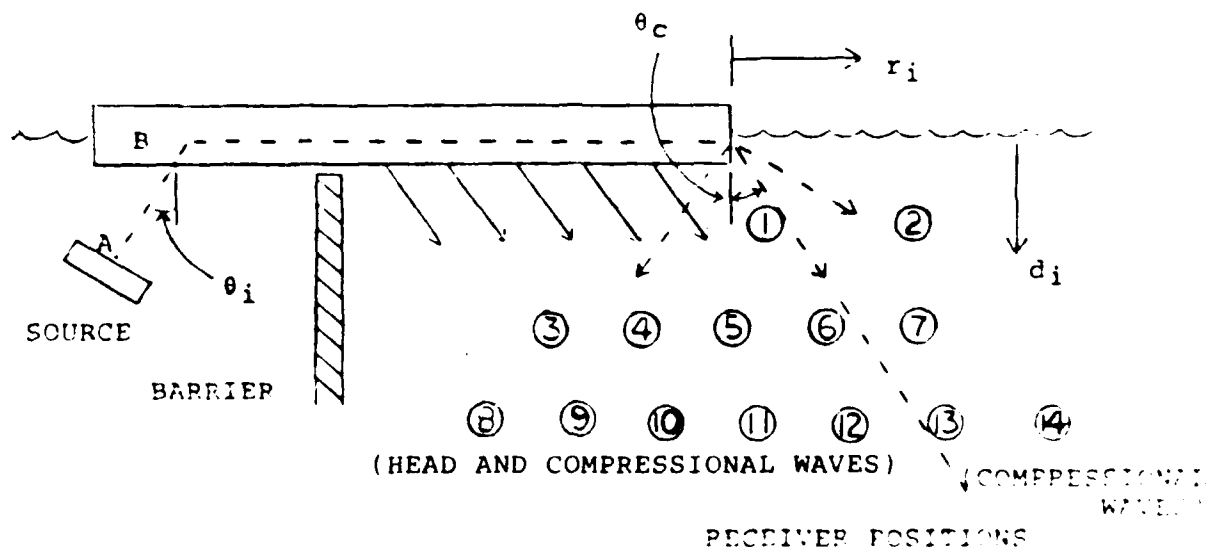


Figure 6.13: Experimental set-up for the mode conversion study.

Source = PZT planar transducer driven with all 12 elements driven with equal amplitude and phase.

Receiver = LC-10 hydrophone at positions $i = 1$ - 14 (distance from plate edge = r ; depth = d)

(NOTE: predicted paths for generation and reradiation of both plate compressional waves and head waves are shown, at the receiver positions indicated in Table V.)

the plate. With this barrier in position, the direct water path from the source to the receiver was attenuated in excess of 50 dB, and the interfering direct and direct/diffracted signals were effectively eliminated.

The source was driven with equal amplitude elements to produce an early uniform plane wave. For two different orientations of the source, the acrylic plate was excited at each of the four (4) frequencies of interest, and reradiation from the plate on the opposite side of the barrier was measured at 14 different receiver positions, varied in both range and depth from the plate edge. The frequencies chosen were 15.6, 23.4, 31.3, and 39.1 kHz, using a burst of 2, 3, 4, or 5 cycles, respectively. They were chosen both for the fact that the signal processing was simplified and for the efficiency of the plate compressional wave excitation at those frequencies. The angle of incidence $\theta_i = 37^\circ$ was chosen as one source orientation because that is the critical angle for generation of compressional waves in the acrylic plate. The angle of incidence $\theta_i = 61^\circ$ was chosen as a compromise between a shallow grazing angle to model convergence zone propagation in the Arctic Ocean and the finite length of the acrylic plate which precluded very shallow grazing angles.

2. Results and Discussion

Figure 6.13 shows a simplified schematic diagram of the source-plate-receiver orientation with the dotted lines

representing the various path lengths of interest. Accurate knowledge of the path lengths was essential to predict the received signal arrival time.

To find the effective starting point of the compressional wave in the plate, the pressure profile was measured above the source at a depth of $1/4$ " below the plate. The 19 cm high source produced a narrow beam which interacted along the bottom of the plate over a 25 to 35 cm length, depending on the source orientation. Figure 6.14 shows the measured pressure profile for the two source orientations. Since the pressure peaked at a specific location beneath the plate, shown on Figure 6.14, that distance from the plate edge was assumed to be the point of maximum excitation of the plate compressional wave, shown as point B on Figure 6.13.

At the receiver end of the plate, it was predicted that the presence of the plate compressional wave would be observed either by reradiation from the edge of the plate as in the previous experiment, or as head wave radiation. Head waves are described by Clay and Medwin (1977) and are well known by geophysicists for a thick, high-speed bottom underlying the lower speed ocean water. A similar situation appears to exist for the high speed compressional wave in the Arctic ice overlaying the lower speed ocean water. Head waves are generated when a sound signal travelling in one medium refracts into a second, higher speed medium by

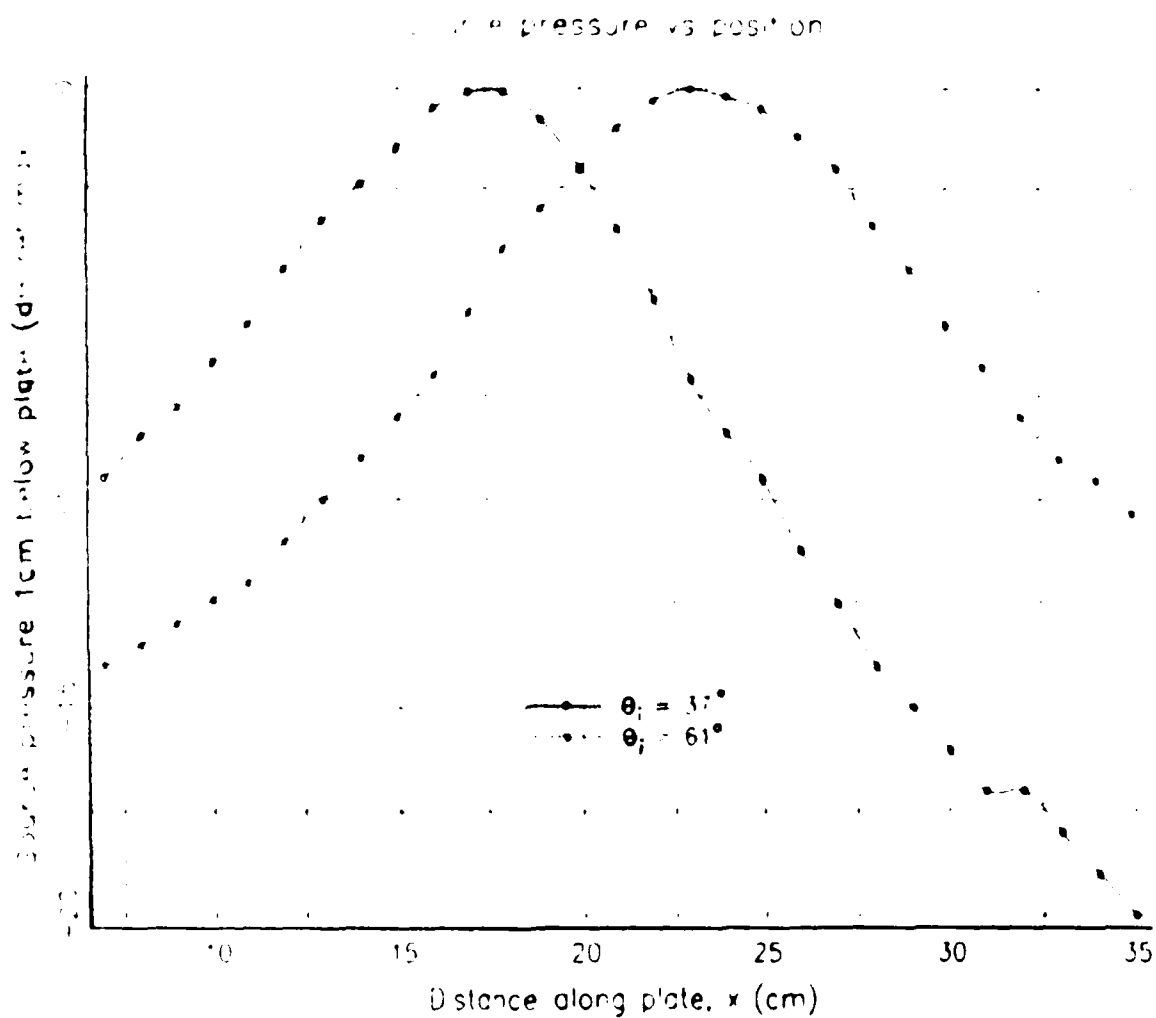


Figure 6.14: Source pressure vs. position.

the critical ray path, causing bulk waves to propagate along the interface at the higher sound speed. The presence of these "lateral waves" is indicated by their reradiation at the critical angle back into the lower speed medium.

Table V lists the predicted arrival times for the head wave and for compressional wave reradiation at the plate edge, as shown in Figure 6.13. The measured arrival times agreed with the path for plate edge reradiation for receiver positions 2, 7, 13, and 14, since those positions were outside the cone of head wave reradiation. All other arrival times agreed more closely with the path for head wave reradiation, and the plate edge radiation was masked by the stronger head wave. Consequently, it was impossible to obtain the desired radiation pattern from the plate edge for which this experiment was designed. However, valuable information was obtained by discovering the presence of the head wave.

Figure 6.15 shows a plot of the head wave spectral density amplitudes in the relative receiver positions for each of the three source frequencies with the source oriented at $\theta_i = 61^\circ$. Although the measured amplitude of the head waves do not precisely agree with the theoretical behavior described in Clay and Medwin (1977) given as

$$\text{amplitude of head wave} \approx x^{\frac{1}{2}} L^{\frac{3}{2}} k^{-1},$$

the character of the reradiation is correct since the

TABLE V

PREDICTED AND MEASURED ARRIVAL TIMES
FOR PLATE COMPRESSIONAL WAVE RERADIATION

Source Angle $\theta_i = 37^\circ$

Arrival time (μsec)

<u>Receiver Position</u>	<u>d(m)</u>	<u>r(m)</u>	<u>Predicted Head Wave</u>	<u>Predicted Plate edge</u>	<u>Actual</u>
1	0.05	0.02	716	728	710
2	0.05	0.10	762	767	761
3	0.11	-0.10	707	792	675
4	0.11	-0.05	711	773	705
5	0.11	0.00	725	766	729
6	0.11	0.05	755	773	757
7	0.11	0.10	787	792	780
8	0.16	-0.20	709	864	664
9	0.16	-0.14	717	835	690
10	0.16	-0.07	722	810	718
11	0.16	0.00	743	800	757
12	0.16	0.07	786	810	800
13	0.16	0.14	830	835	826
14	0.16	0.20	859	864	867

Source Angle $\theta_i = 61^\circ$

Arrival time (μsec)

<u>Receiver Position</u>	<u>d(m)</u>	<u>r(m)</u>	<u>Predicted Head Wave</u>	<u>Predicted Plate edge</u>	<u>Actual</u>
1	0.05	0.02	747	767	719
2	0.05	0.10	794	809	785
3	0.11	-0.10	721	837	691
4	0.11	-0.05	743	821	720
5	0.11	0.00	759	810	743
6	0.11	0.05	796	821	772
7	0.11	0.10	811	837	796
8	0.16	-0.20	733	909	680
9	0.16	-0.14	751	880	704
10	0.16	-0.07	756	854	741
11	0.16	0.00	777	844	768
12	0.16	0.07	818	854	802
13	0.16	0.14	864	880	844
14	0.16	0.20	894	909	879

(NOTE: Actual arrival times represent the average arrival time at that receiver position for the four frequencies of interest.)

amplitudes approximately follow lines of constant pressure. For the parameters given above, x is the horizontal distance between source and receiver, L is the distance that the head wave travels in the plate, and k is the wave number.

The source was oriented to correspond with the critical angle ray path ($\theta_i = 37^\circ$), as well as a shallower angle ($\theta_i = 61^\circ$) at which total internal reflection would also take place, to simulate how sound propagating over long ranges in the Arctic will interact with the ice cover (such as for convergence zones). Mode conversion of the compressional wave in water to the compressional (or lateral) wave in the plate was 40% more efficient when the source was oriented at the critical angle, as indicated by the head wave magnitudes for 15.6 kHz in Table VI. The behavior of the head waves was similar for the other frequencies, suggesting that for convergence zone propagation in the Arctic, both mode conversion and reflection may occur at each interaction with the undersurface of the ice, since head waves were also effectively generated at shallow grazing angles.

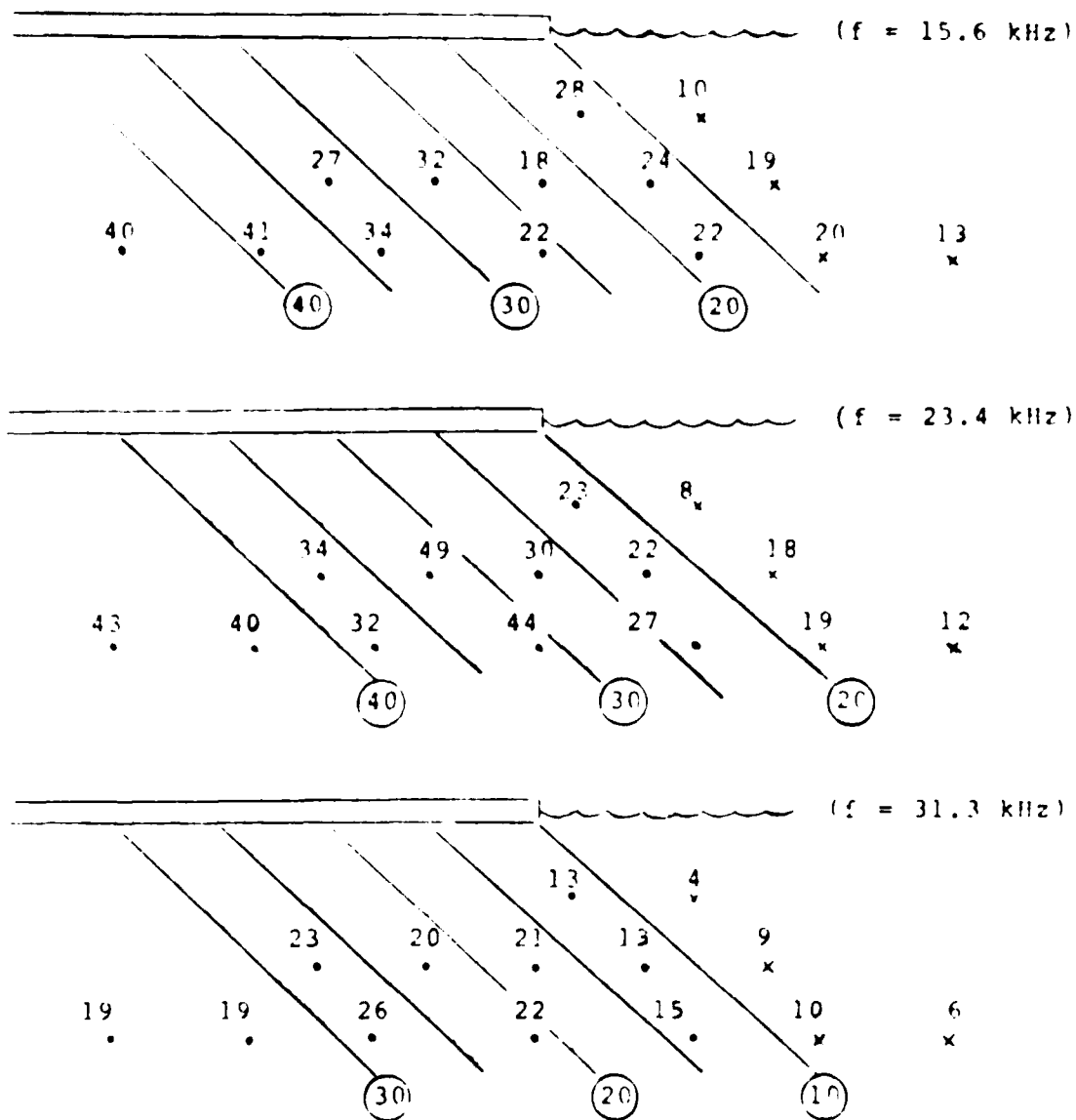


Figure 6.15: Head wave amplitudes (rounded to nearest integer) for mode-conversion experiment at each frequency. Circled values at bottom of each figure represent approximate location of isopressure lines. Receiver positions marked by an 'x' indicate those positions outside of the cone of head wave radiation.

TABLE VI

MEASURED HEAD WAVE AMPLITUDES
(for frequency, $f = 15.6$ kHz)

<u>Receiver Position</u>	<u>Source Angle $\theta_i = 37^\circ$ Amplitude, (V pp) -</u>	<u>Source Angle $\theta_i = 61^\circ$ Amplitude, (V pp)</u>
1	28.30	15.83
2	9.99	7.49
3	27.00	17.27
4	32.50	20.67
5	18.43	11.02
6	23.68	14.15
7	18.86	10.65
8	40.54	25.03
9	40.91	19.42
10	34.19	19.14
11	22.48	18.18
12	22.39	14.07
13	19.93	9.72
14	13.34	7.52

VII. ELEVATION ANGLE DEPENDENCE OF BACKSCATTER FROM A RIDGE

The objective of this experiment was to obtain backscatter measurements from the three acrylic models of different size ice keels in order to determine how the level and the character of backscatter depend on the height and slope of the keel. Measurements were made to show the characteristic behavior of backscatter for grazing and normal incidence, as well as the dependence on frequency and elevation angle.

A. EXPERIMENTAL PROCEDURE

The laboratory measurements of backscatter from the ice pressure ridge models were performed in the Ocean Acoustics Wave Facility tank described in Chapter II. The fabrication process and dimensions of the three pressure ridges are described in Chapter III.

Two LC-10 hydrophones were mounted for monostatic backscatter by extending a single, thin stainless steel rod from the side of the tank. Typical measurements were made with the source/receiver positioned 50 cm from the "ice keel", which prevented plate side diffraction from interfering with the backscattered signal of interest, and also allowed the strong direct signal between source and receiver to decay prior to receiving the backscattered signal.

At shallow grazing angles, the reflection from the overhead plate was well isolated and could be windowed out from the ridge scatter. At steep grazing angles (greater than 50°), the surface reflected signal from the smooth plate directly above the source/receiver, overlapped the backscattered signal of interest. Figure 7.1 illustrates the technique used to overcome this difficulty. Figure 7.1 (a) is a typical waveform for an incident angle of 50° , and shows the strong surface reflection immediately followed by the signal backscattered from the ridge. Moving the plate to increase the propagation path to the ridge results in Figure 7.1 (b), where the backscattered signal has been shifted out of the time window and only overhead reflection remains. Figure 7.1 (c) is an ineffective point-by-point computer subtraction of Figures 7.1 (a) and 7.1 (b); however, to obtain backscatter only, a slightly different depth of plate immersion resulted in a measurable time shift in the reflected arrival sufficient to prevent clean subtraction. Figure 7.1 (d) is the resulting subtracted waveform when the time shift was corrected prior to subtraction, and only the backscattered signal remains.

Four experiments were performed on each of the three pressure ridges:

- (1) A horizontal probe (at the depth of the ridge crest) of the backscattered pressure field due to the ridge at grazing over the range $r = r_0 = 20$ to 70 cm.

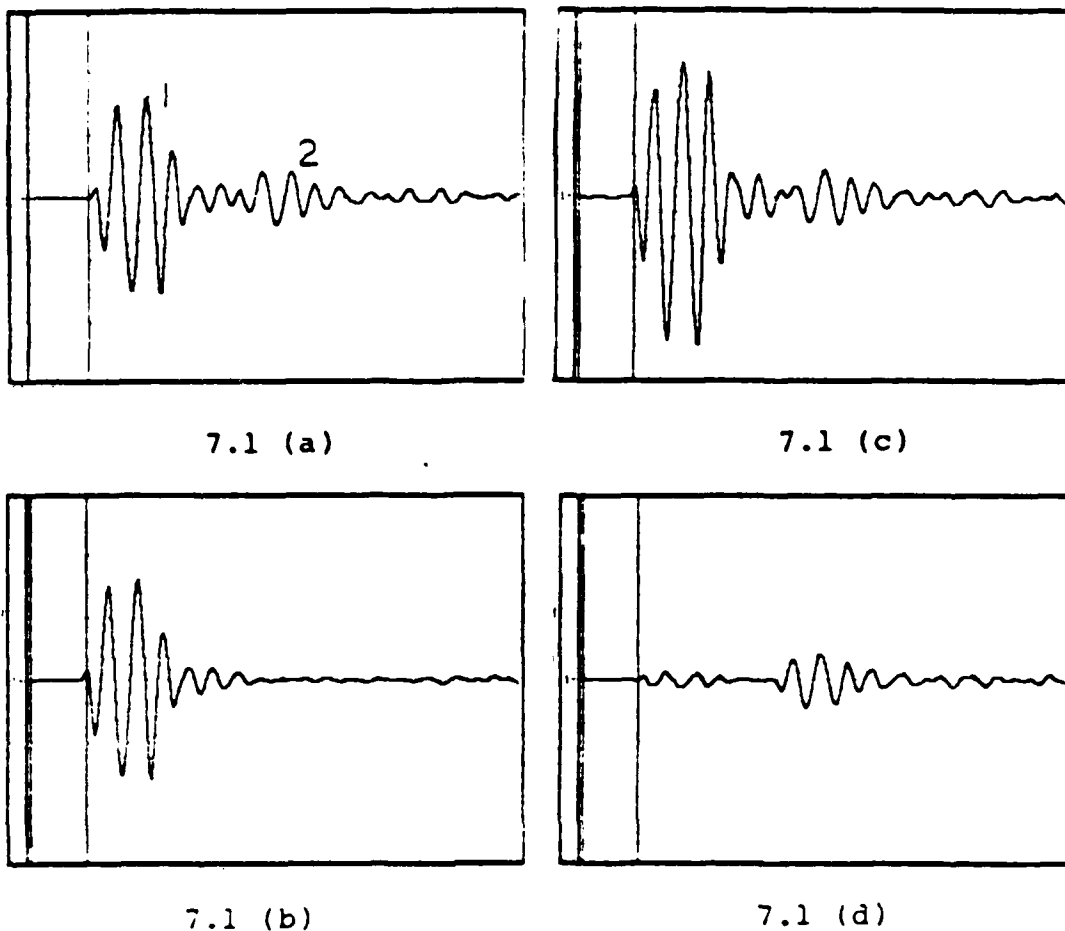


Figure 7.1: Subtraction technique used in backscatter measurements. Grazing angle = 50° , frequency = 62 kHz.

- (a) Plate reflection (1) plus total backscatter (2).
- (b) Plate reflection alone.
- (c) Subtraction of (a) - (b) without time shift to account for the variation in plate immersion depth.
- (d) Subtraction of (a) - (b) using a 4 μ sec time shift to account for the difference in plate immersion depth. The major signal is due to ridge backscatter

- (2) A vertical probe of the backscattered pressure field below the ridge for normal incidence over a depth range $d = d_0 = 10$ to 70 cm.
- (3) A frequency dependence experiment for which the backscatter was measured for nine frequencies at grazing angles $\theta = 10^\circ$ and $\theta = 20^\circ$ from the horizontal.
- (4) An experiment to determine the dependence of backscatter on elevation angle, by holding the source/receiver at a fixed radius $r = r_0 = 50$ cm and probing in elevation angle from $\theta = 0^\circ$ to $\theta_0 = 90^\circ$ to find the "directivity pattern" of the sound scattered from the ridge.

Figure 7.2 shows the source/receiver geometry with respect to the ridge for each of the four experiments. Typical measurements were made driving the source with a 20 volt peak-to-peak pulsed sinusoid of 1, 2 or 3 cycles and 32 μ sec duration. Although the electrical input signal was 32 μ sec, the received acoustic signal was much longer due to mode-converted reverberation in the ridge, and backscatter from different parts of the ridge.

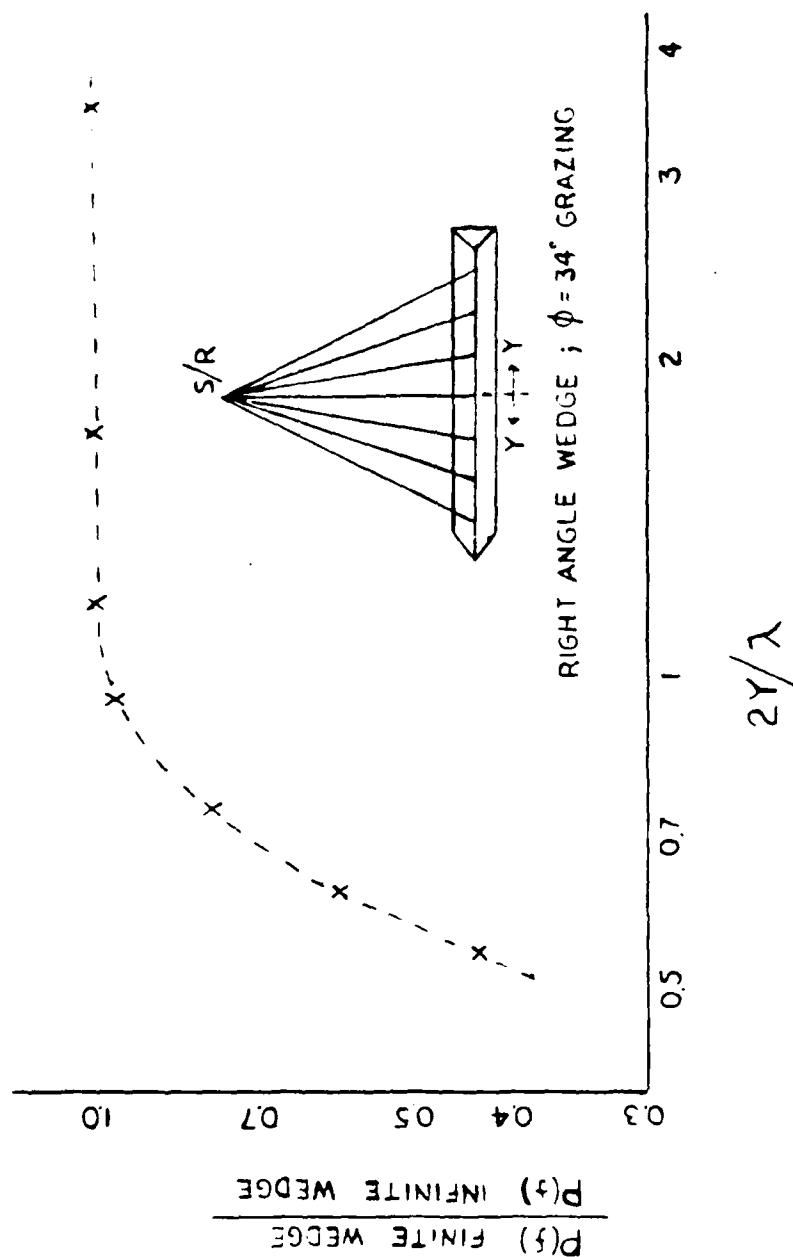
The analysis window chosen was sufficiently long to include all of the backscattered energy, then "zero-padded" with as few extra zero points as possible in order to obtain a power of two (2^n total points, $n = \text{any integer}$) to allow the received signal to be transformed using a Discrete Fourier Transform (DFT) algorithm. The source frequencies used coincided with the bin frequencies from the DFT to minimize the Gibbs' effect (Clay and Medwin, 1977). The backscattered spectral pressure from the ridge was proportional to the magnitude of the response from the DFT, and

all received signals are expressed in decibels, using the backscattering strength (BSS) definition:

$$\text{BSS (dB)} = 10 \log_{10} \frac{P_{BS}^2 \cdot R^{N+2}}{P_0^2 \cdot R_0^N \cdot A}$$

In this equation, P_0 is the reference pressure at range R_0 , P_{BS} is the received backscatter pressure at range R , A is the surface area over which the scattering is measured, and N is the degree of geometrical divergence of the backscatter ($0 \leq N \leq 2$).

The Biot-Tolstoy theory of diffraction predicts the maximum amount of energy which will diffract from an infinite, rigid wedge. When digital signal processing techniques are used, the wedge need not be infinite in length if the analysis time window is closed before sound reaches the ends of the finite wedge. Naturally, if the wedge is not infinite in length, something less than the maximum amount of energy will be diffracted. The calculation of data for Figure 7.3 was provided by Mr. Ken Reitzel and shows the amount of energy which will diffract from various length finite wedges in comparison to the infinite wedge, where the wedge length is $2Y$, centered about the least time point. Notice that only a fraction of the maximum possible energy is diffracted when $2Y$ is less than an acoustic wavelength, and nearly all of the energy is



Spectral response for a finite wedge of length $2Y$ in comparison to the predicted diffraction from an infinite wedge.

AD-A184 693

UNDERWATER ACOUSTIC BACKSCATTER FROM A MODEL OF ARCTIC
ICE OPEN LEADS AND PRESSURE RIDGES(U) NAVAL
POSTGRADUATE SCHOOL MONTEREY CA M J BROWNE

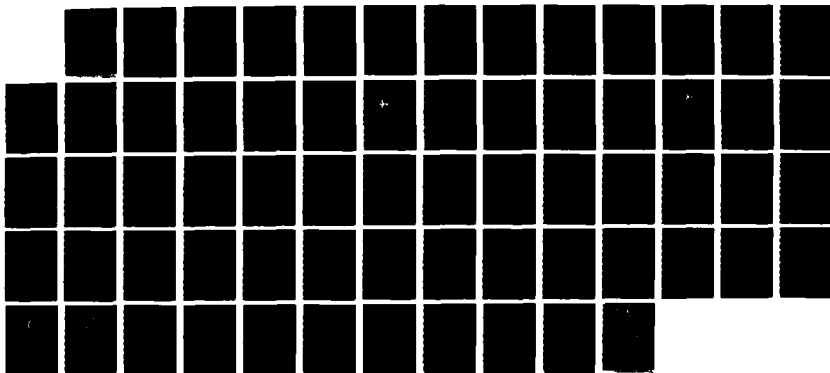
JUN 87

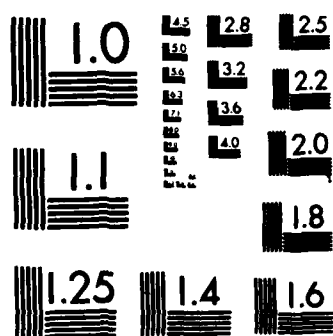
F/G 28/1

2/2

NL

UNCLASSIFIED





MICROCOPY RESOLUTION TEST CHART
NATIONAL BUREAU OF STANDARDS-1963-A

diffracted when $2Y$ is greater than a wavelength. A finite wedge whose length equals one acoustic wavelength will diffract 96% of the maximum possible energy. From another point of view, 96% of the diffracted energy comes from one acoustic wavelength of the ridge in the least time region, and the remainder of the ridge contributes only 4% of the energy. For backscatter at long ranges, a pressure ridge should effectively behave as a point scatterer (since the majority of the energy is diffracted from the least time region), and spherical divergence would be expected. Then, the equation for backscattering strength becomes:

$$\text{BSS (dB)} = 10 \log_{10} \left[\frac{P_{BS}^2 R^4}{P_O^2 R_O^2 A} \right] \quad (7.1)$$

In the case of the vertical probe experiments, the backscattered signal was essentially a reflection from the smooth plate, slightly altered by the presence of the ridges. In that case, the backscatter can also be calculated in terms of dB referenced to a mirror (i.e., perfect reflection):

$$\text{dB (ref mirror)} = 20 \log_{10} \left[\frac{P_{BS} R}{P_O R_O} \right] \quad (7.2)$$

If the backscatter comes from a point, then experimental agreement with theory will be better when Equation (7.1) is used; if the backscatter more closely resembles a reflection, then Equation (7.2) yields the best agreement with theory.

B. "TYPICAL" RIDGE RESULTS

The "typical" ridge used for this experiment was designed to model the typical pressure ridge found in the Central Arctic basin as described in Chapter III. It served as the standard against which the "large" ridge (twice the height) and the "steep" ridge (twice the slope) were compared.

1. Horizontal Probe

For the horizontal probe using the "typical" ridge, the source/receiver were positioned 1.6 cm below the ice plate to correspond with the depth of the ridge crest. Figure 7.4 shows a typical received waveform. The received signals in all cases were composed of the two parts shown: an initial arrival which agreed in time with diffraction from the ridge crest (corresponding to point B) and a second arrival which agreed with the propagation time required for an acoustic signal to be mode-converted into the ridge, reflect from the back facet of the ridge (at point C), and return by the reverse path. There was no measurable backscatter observed from point A of the ridge.

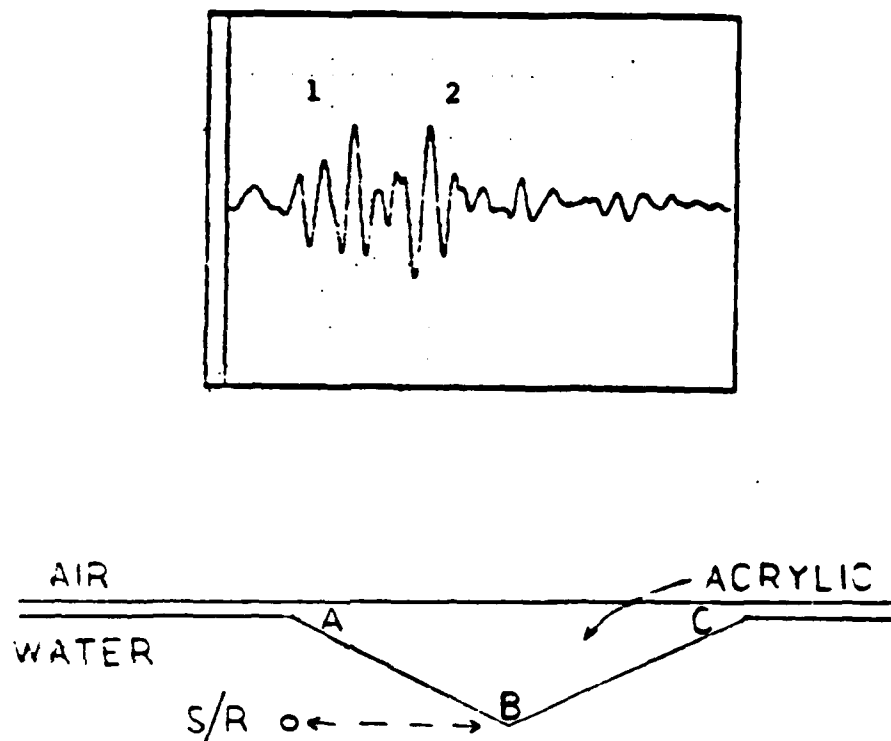


Figure 7.4: Typical received waveform for horizontal probe using the "typical" ridge.

($f = 62.5$ kHz, $N = 2$ cycles, $r = 40$ cm, 500 mV scale)

(1) = diffraction from the ridge crest at point B

(2) = reflection of mode-converted energy from point C

Figure 7.5 shows the divergence characteristic for the horizontal probe from the "typical" ridge. Equation (7.1) was used to calculate the BSS, assuming the backscatter from the ridge diverged spherically. Except for oscillations, the BSS is virtually constant with increasing range, suggesting the ridge must have produced the backscatter from an effective point (corresponding to the least time region on the ridge) for spherical divergence. Since the source/receiver were quite close to the plate, the oscillations of BSS with increasing range are probably due to surface interference of the backscattered sound.

2. Vertical Probe

In the vertical probe experiment on the "typical" ridge, certain effects of the characteristic behavior of the backscatter were apparent, but could only be analyzed qualitatively. It was more obvious in the vertical probe experiment for the "large" ridge, (where signal separation in time was improved due to the larger dimensions), what the various parts of the backscattered signal were due to.

Figure 7.6 shows a typical received waveform for the case where 2 cycles of a 62 kHz sinusoid are used. The direct signal is slightly more than 2 cycles due to hydrophone ringing. There appeared to be three distinct components to each backscattered waveform. The first arrival in time agreed with the path length for diffraction from the

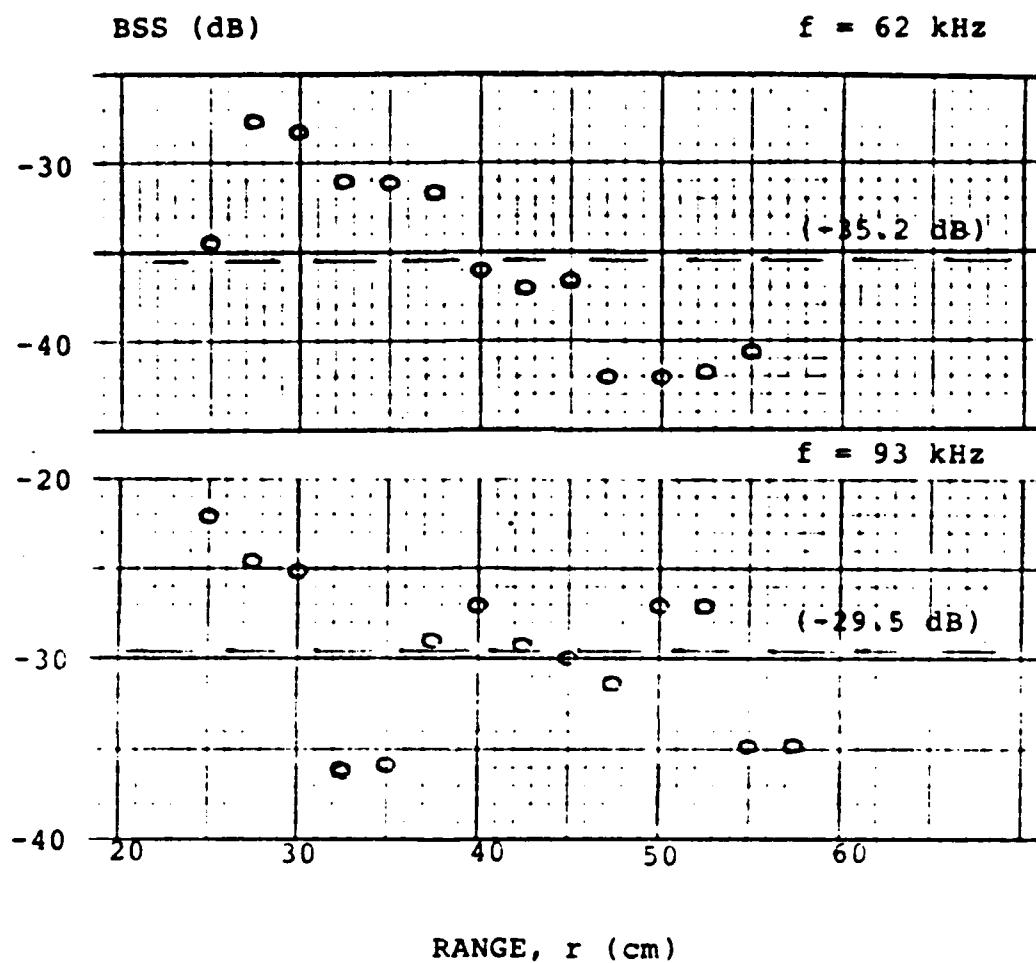


Figure 7.5: Plot of BSS versus range, r (cm), for the horizontal probe experiment using the "typical" ridge. (mean value of BSS in parentheses)

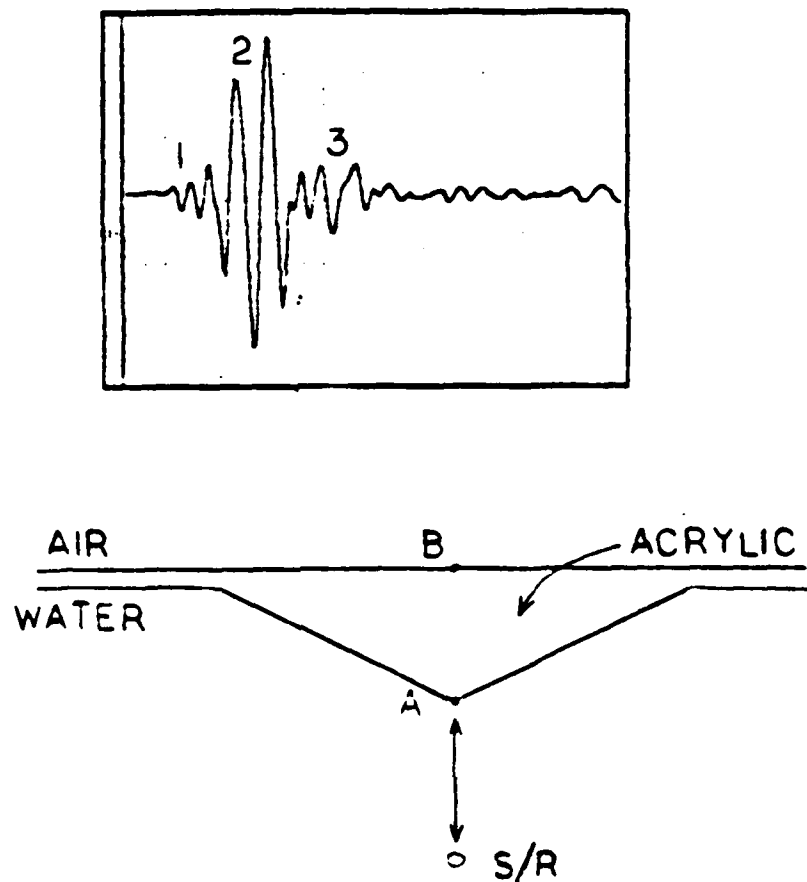


Figure 7.6: Typical received waveform for vertical probe experiment using the "typical" ridge.

($f = 62.5$ kHz, $N = 2$ cycles, $d = 40$ cm, 2.0 V scale)

- (1) = diffraction from crest of ridge
(path S-A-R)
- (2) = reflection from ice-air interface
(path S-A-B-A-R)
- (3) = reradiation of ridge reverberation

crest of the ridge. The second, much larger arrival agreed in time with the path length for an acoustic signal (13 μ sec later) which reflected from the "ice"-air interface before returning by the reverse path. Finally, there appeared to be some energy arriving after the reflection, due to the reverberation of mode-converted sound within the ridge which was then reradiated into the water.

Figure 7.7 is a plot of the BSS versus depth below the ridge for the vertical probe, calculated using Equation (7.1). Since the 31 kHz BSS was nearly independent of depth for range greater than 35 cm, the assumption of spherical divergence from a point on the ridge is evidently valid. At 62 and 93 kHz, the variations of the backscatter about the average value is assumed to be due to interference of the spatially-extended ridge reverberation and reflection from the acrylic-air interface. When the scattering is plotted in terms of dB (ref mirror) as in Figure 7.8, the results were also nearly linear, which implies that the effects of the plate reflection were just as important as the backscatter from the ridge since the experimental agreement with theory is about the same when using either definition.

3. Frequency Dependence

The frequency dependence experiment using the "typical" ridge produced no meaningful results.

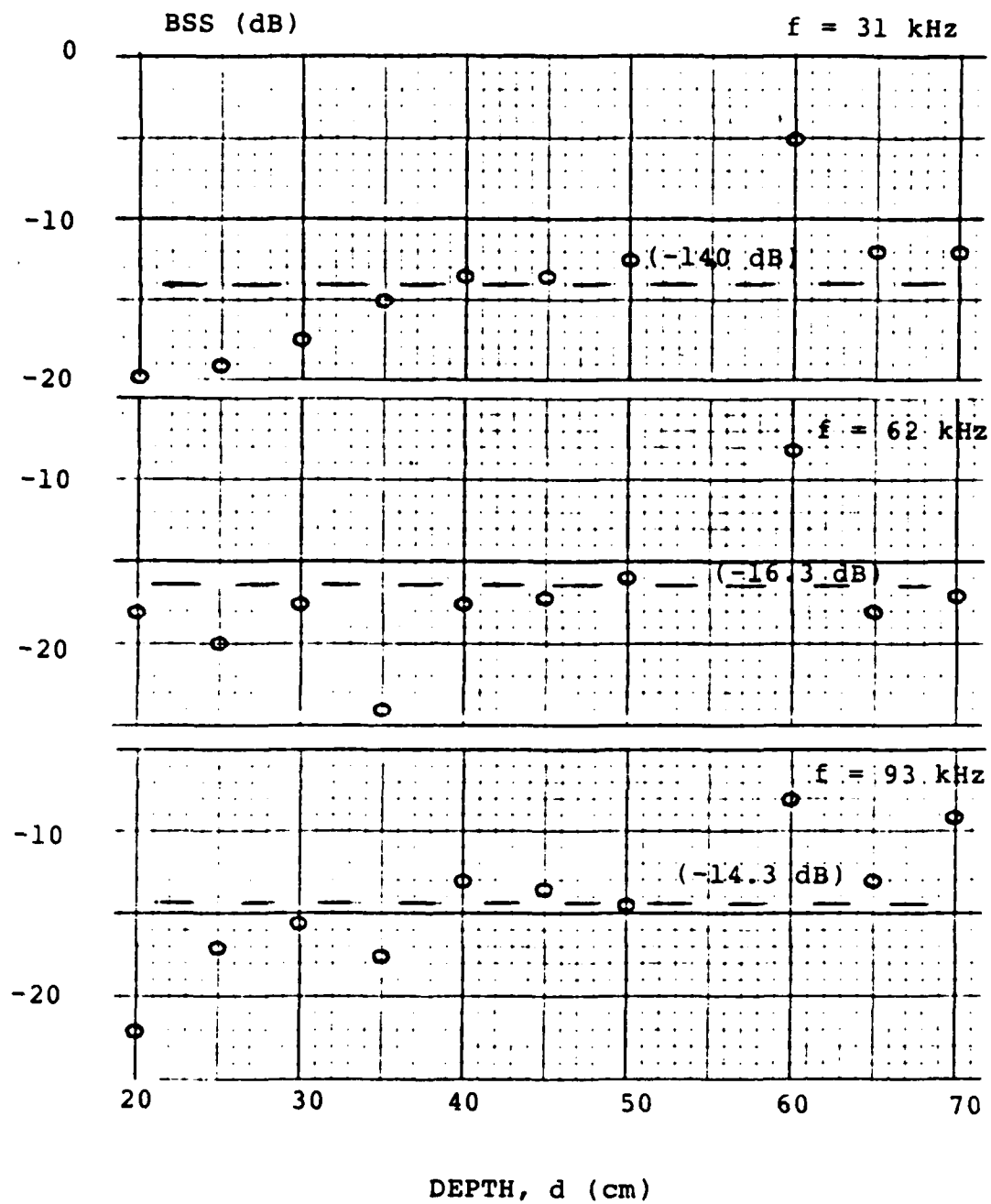


Figure 7.7: Plot of BSS versus depth, d (cm), for the vertical probe experiment using the "typical" ridge. (mean value of BSS in parentheses)

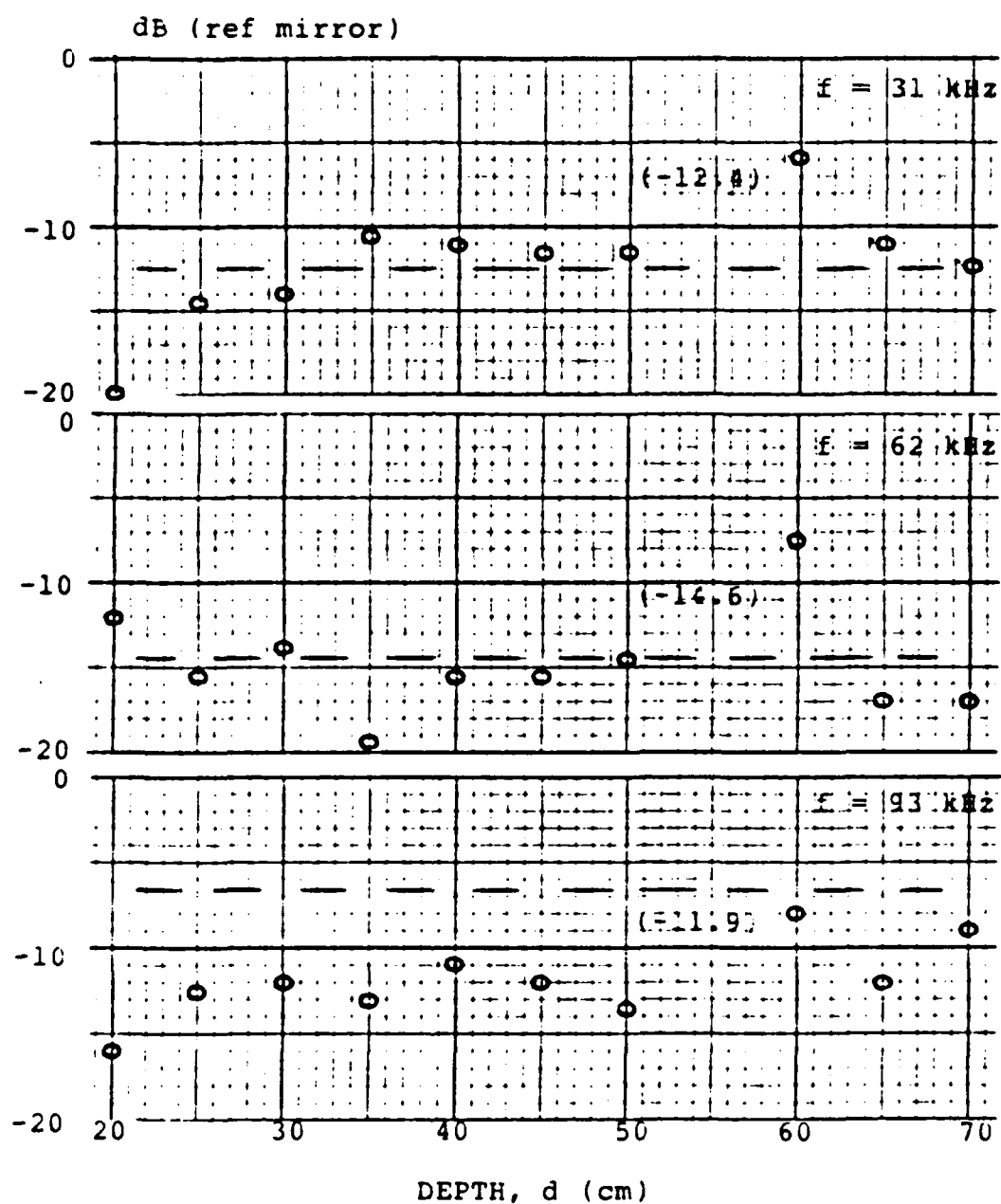


Figure 7.8: Plot of dB (ref mirror) versus depth, d (cm), for the vertical probe experiment using the "typical" ridge. (mean value shown in parentheses)

4. Elevation Angle Dependence

The source and receiver were positioned for monostatic backscatter at a fixed distance $r = r_0 = 50$ cm from the ridge for grazing angles ranging from 0° to 90° . Two source frequencies were used, $f = 62.5$ kHz and $f = 93.9$ kHz, corresponding to $\lambda_1 = 2.37$ cm and $\lambda_2 = 1.58$ cm.

Assuming that the ridge reverberation would radiate from the facets, the ridge was modelled as a finite reflector or aperture, similar to a rectangular piston, infinite in one direction. In the case of the "typical" ridge, the "active" piston face, corresponding to the slant face height, was $H = 3.41$ cm so that

$$H/\lambda_1 = 1.44$$

$$H/\lambda_2 = 2.16.$$

The directivity pattern for the equivalent rectangular piston transducer is given by:

$$D(\phi, \chi) = \frac{\sin\left[\left(\frac{kw}{2}\right)\sin\phi\right]}{\left(\frac{kw}{2}\right)\sin\phi} \cdot \frac{\sin\left[\left(\frac{kH}{2}\right)\sin\chi\right]}{\left(\frac{kH}{2}\right)\sin\chi}$$

where ϕ and χ are the angles shown in Figure 7.9, and W and H are the width and height of the piston. All measurements were taken for source/receiver positions normal to the ridge, so that $\phi = 0^\circ$ and $0^\circ \leq \chi \leq 90^\circ$. The magnitude of the backscattering strength was plotted as a function of angle and compared to the theoretical directivity pattern which was adjusted to a level for best fit as shown in

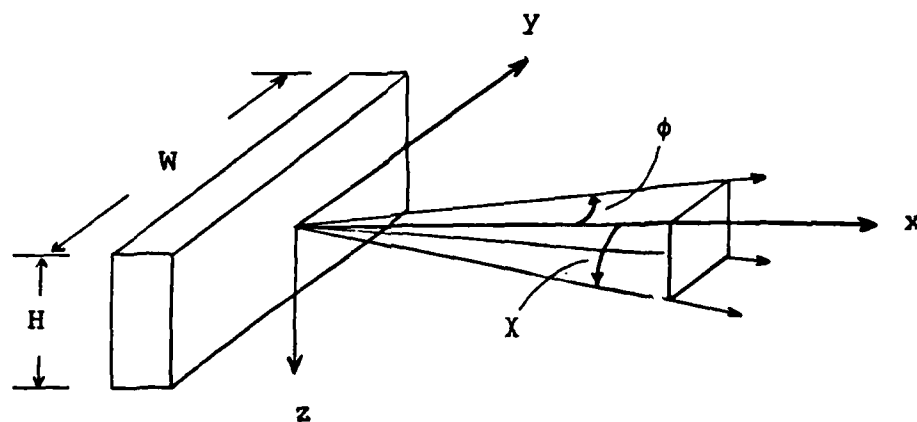


Figure 7.9: Geometry for radiation from a rectangular piston. (Clay and Medwin, 1977)

Figure 7.10. The piston axis, $\chi = 0$, was set to be perpendicular to the facet.

The backscattered data were straightforward to analyze. Backscatter measurements for grazing angles $\theta = 0^\circ$ to 50° could be analyzed directly since there were no interfering signals. For grazing angles, $\theta = 60^\circ$, 70° , and 80° , the specular reflection from the overhead plate interfered with the backscattered signal and was subtracted out using the technique described in the experimental procedure section. At normal incidence ($\theta = 90^\circ$), the plate reflection and backscatter completely overlapped (as in the vertical probe experiment), resulting in a measured value much larger than predicted. It would be meaningless to subtract the reflected portion of the backscattered signal at normal incidence because it is an important part of the scattering characteristic for that geometry, as shown in Figure 7.10.

There was fair agreement between the theoretical curve and the measured backscattering strength as a function of angle for the "typical" ridge. The BSS measurement has two components: the Biot-Tolstoy diffraction from the three corners of the ridge, as well as the radiation from the rectangular apertures. Since the characteristic dimension of the piston was on the same order of magnitude as an acoustic wavelength, the rectangular aperture was not an

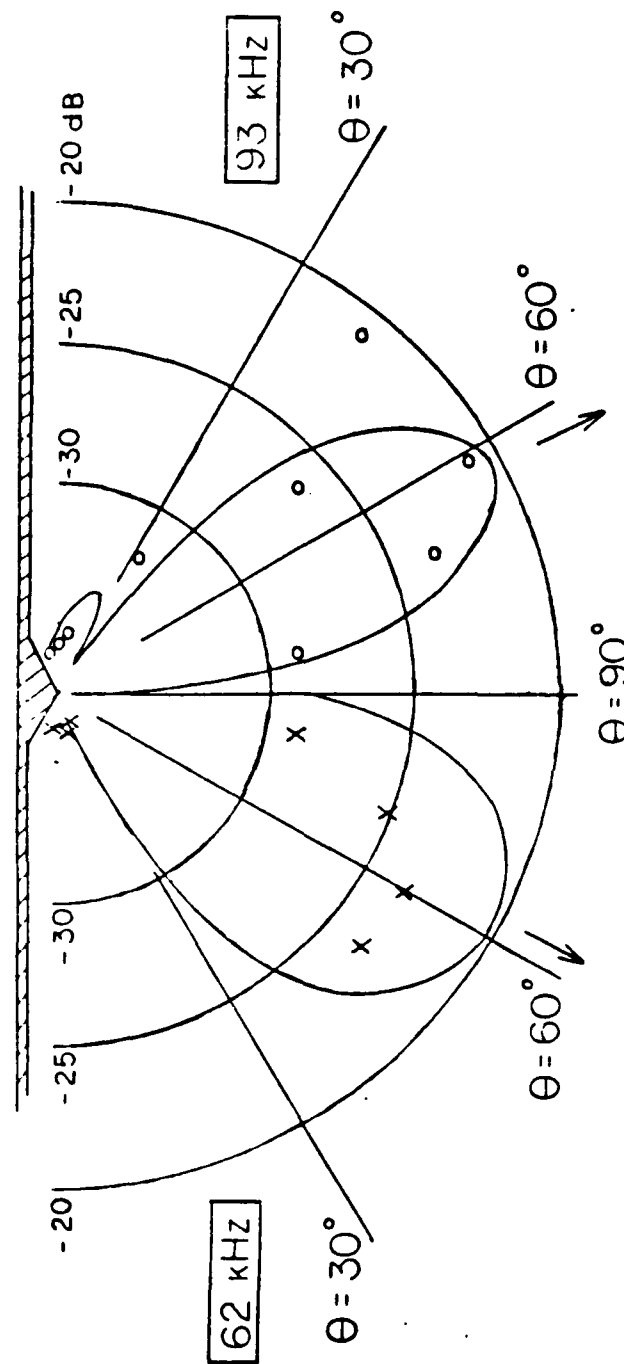


Figure 7.10: Elevation angle dependence of the total backscatter strength for the "typical" ridge compared to the directivity pattern of facet radiation from an equivalent rectangular piston. The arrow shows the piston axis for each ridge facet. (Two frequencies are shown, $r = 50$ cm.)

efficient projector, so neither effect dominated. Consequently, the comparison with the equivalent piston radiation pattern was incomplete, since diffraction from the corners also represented a significant contribution to the BSS.

C. "LARGE" RIDGE RESULTS

The "large" ridge was twice the height but the same slope as the "typical" ridge (see Figure 3.1 and Table III for the dimensions). The experiments using the "large" ridge provided keen insight into the response of an ice keel to an incident acoustic wave; since the dimensions provided greater separation in time of the signals backscattered from various parts of the ridge, and therefore, allowed each effect to be analyzed individually.

1. Horizontal Probe

For the "large" ridge, the source/receiver were positioned 3.2 cm beneath the plate to correspond with the depth of the ridge crest.

Figure 7.11 shows a typical received waveform and the probable paths which combined to yield those results. Notice that diffraction from the crest of the ridge represented the largest contribution to the backscattered signal. When the incident acoustic energy struck the front facet of the ridge, a small amount of energy was diffracted from the discontinuity at point A. Then, the incident wave reached the ridge crest (point B) and a larger amount of energy was

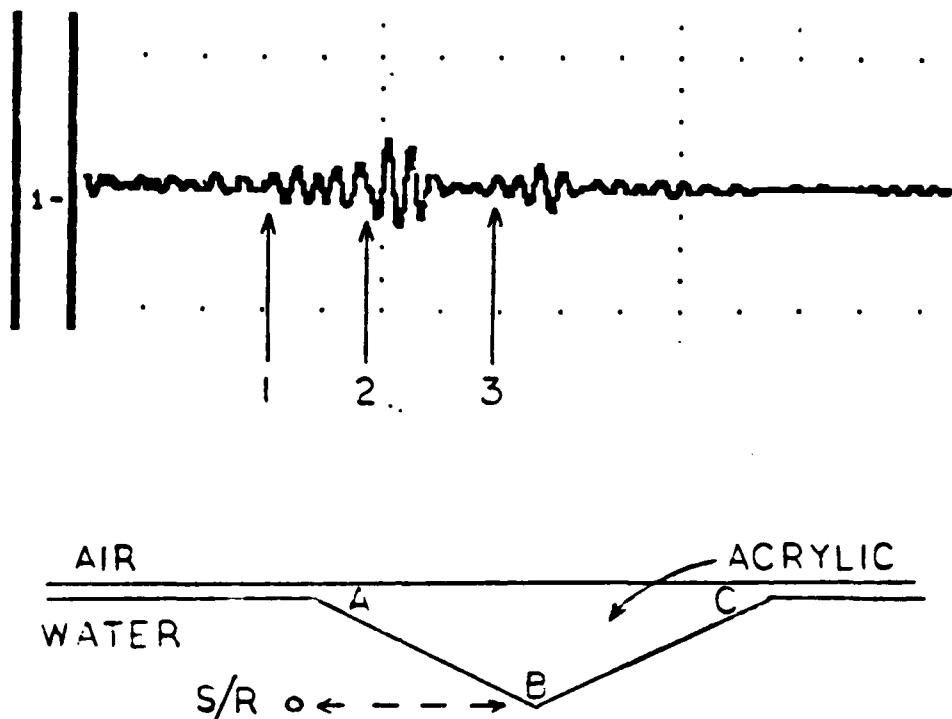


Figure 7.11: Typical received waveform for the horizontal probe experiment using the "large" ridge.

($f = 62.5$ kHz, $N = 2$ cycles, $r = 40$ cm, 2.0 V scale)

- 1 = ridge diffraction from point A
- 2 = diffraction from the ridge crest at point B
- 3 = reflection of mode-converted energy from point C.

diffracted. Finally, some of the energy incident on the front facet was mode-converted into compressional waves in the ridge, propagated through and reflected from the back side of the ridge (point C), and returned to the receiver by the same path to complete the backscatter. Each of the paths described above has been verified by the arrival time using the specific path lengths and appropriate speeds of propagation.

Figure 7.12 shows a typical divergence characteristic for a horizontal probe from the ridge. For spherical divergence of sound from the point source, and spherically diverging backscatter from the ridge, overall divergence of pressure proportional to the inverse square of the range was expected. BSS was calculated using Equation (7.1), where spherical divergence was assumed. The experimental results were in excellent agreement with the inverse square behavior, indicating that the majority of the backscatter occurred from the region on the ridge near the least time, and that the backscattered divergence was spherical.

2. Vertical Probe

In the vertical probe experiment on the "large" ridge, the size again provided relatively long time separations between the different propagation paths to allow each portion of the total backscattered signal to be analyzed individually.

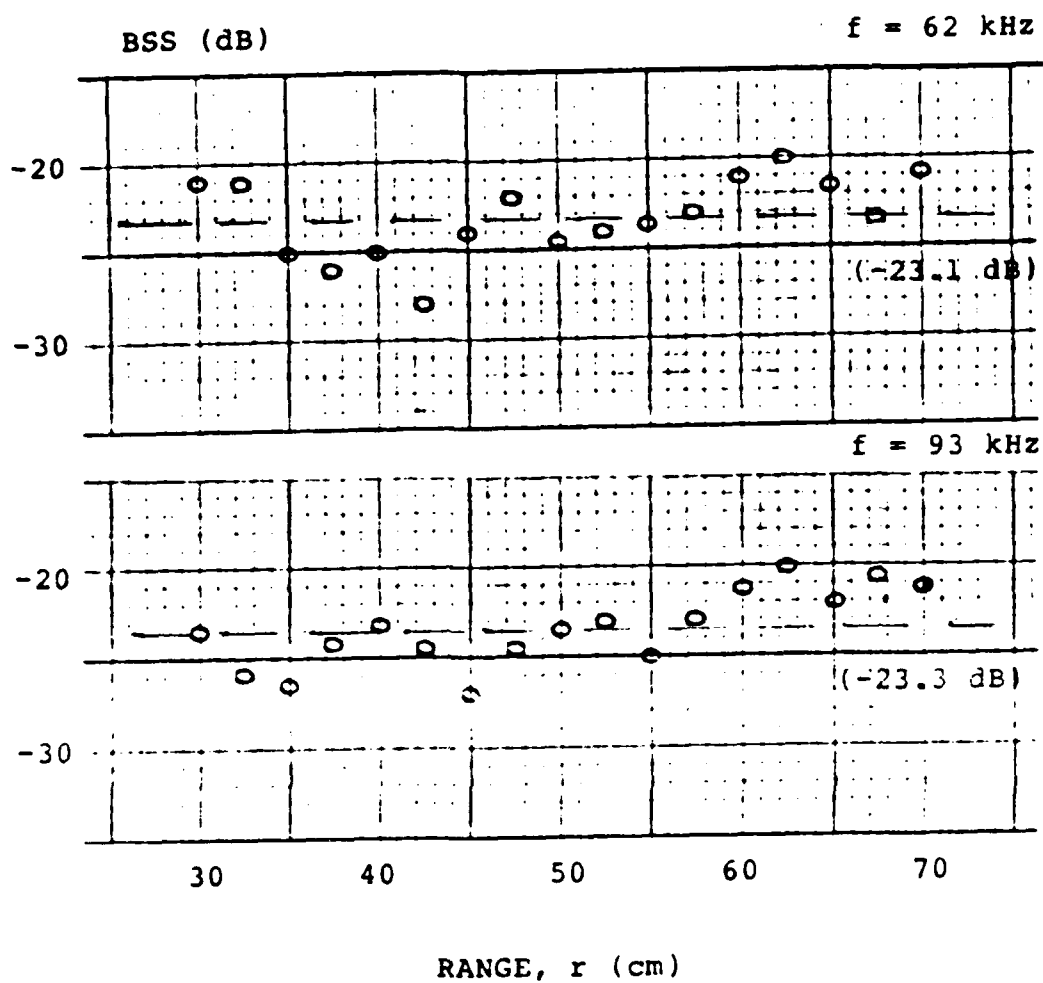


Figure 7.12: Plot of BSS versus range, r (cm), for the horizontal probe experiment using the "large" ridge. (mean value of BSS shown in parentheses)

Figure 7.13 shows a typical received waveform and the probable paths which combined to yield those results. The total backscattered signal is the composite of three distinct contributions: (1) diffraction from the crest of the ridge at point A; (2) reflection from the "ice"-air interface due to the energy which was mode-converted into the ridge, reflected from the surface, and reradiated back into the water (path ABA); and (3) mode-conversion induced reverberation in the ridge, which is seen in the waveform as the decaying energy after the surface reflection and includes the "double reflection" within the ridge (path ABABA).

Figure 7.14 is a plot of the divergence characteristic due to the diffraction from the ridge crest (corresponding to the energy arriving prior to the reflection in Figure 7.13). Since the diffracted signal experiences no interference from other paths, the expected spherical divergence was obtained, and is shown as the inverse square behavior for the round trip energy.

When the total backscattered signal (diffraction plus reflection plus reverberation) is plotted as a function of position, as in Figure 7.15, the inverse square dependence is not obtained due to interference effects. For example, the large difference in the magnitude of the received pressure for a frequency of 93 kHz at 30 and 35 cm below the

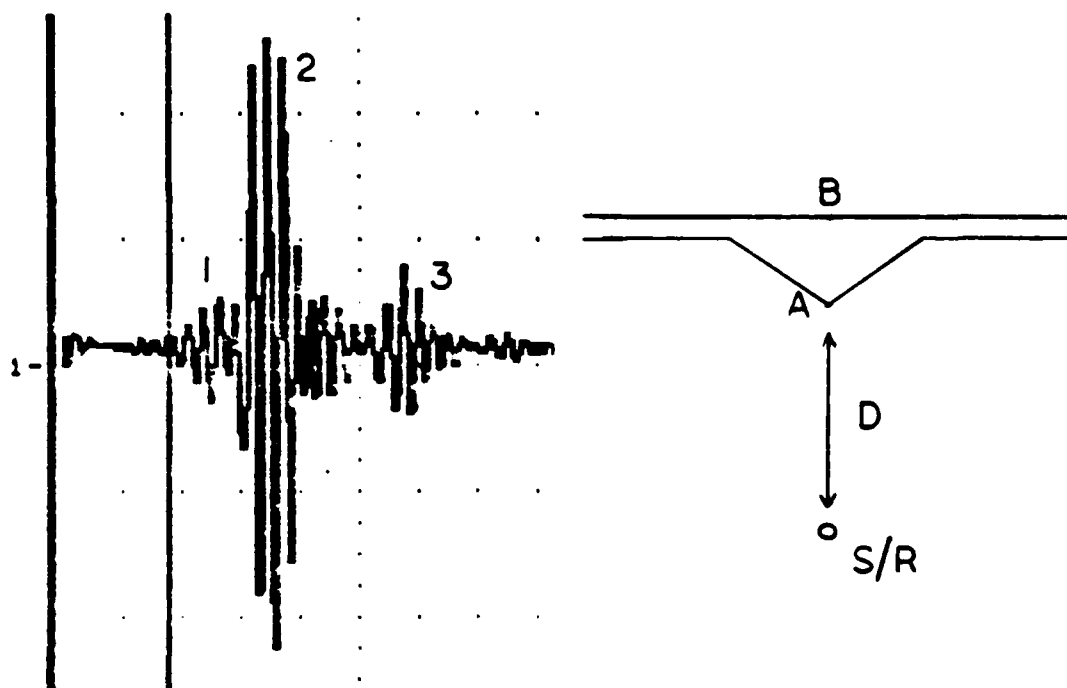


Figure 7.13: Typical received waveform for the vertical probe experiment using the "large" ridge.

($f = 93.9$ kHz, $N = 3$ cycles, $d = 30$ cm, 200 mV scale)

- 1 = diffraction from ridge crest
(path S-A-R)
- 2 = reflection from ice-air interface
(path S-A-B-A-R)
- 3 = double reflection and reradiation
(path S-A-B-A-B-A-R)

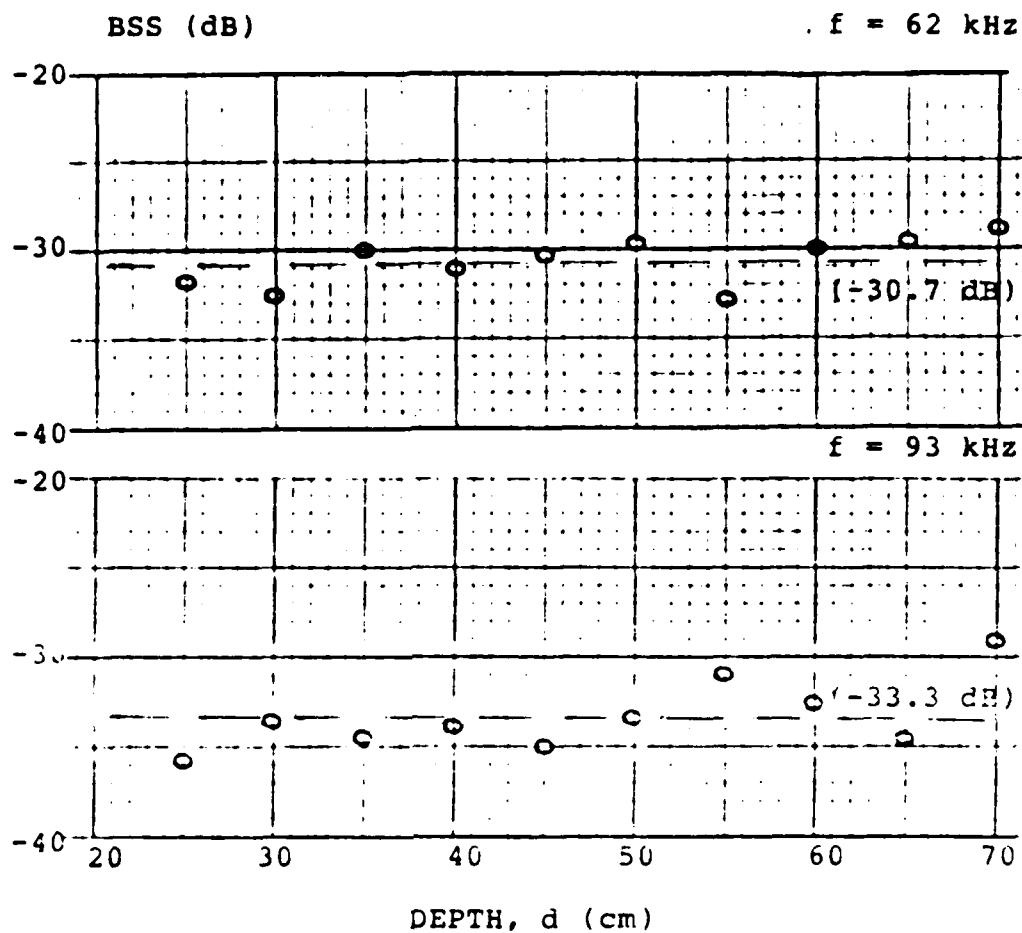


Figure 7.14: Plot of the divergence characteristic due to diffraction from the crest of the "large" ridge as a function of source/receiver depth. (The measured values correspond to energy received prior to the reflection in Figure 7.13.) (mean value of BSS in parentheses)

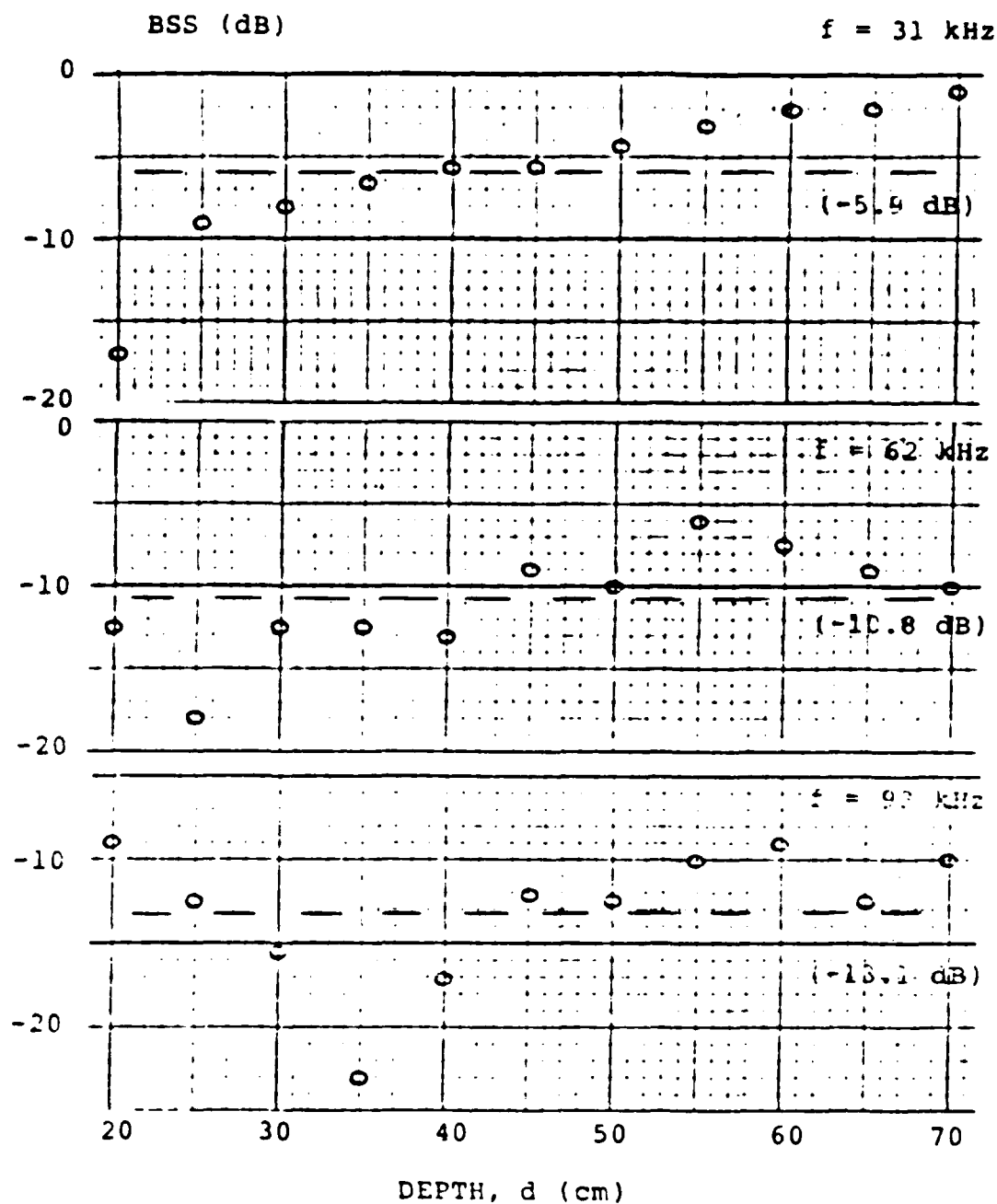


Figure 7.15: Plot of BSS versus depth, d (cm), for the vertical probe experiment using the "large" ridge. (Accounts for all of the backscattered energy.) (mean value of BSS in parentheses)

ridge is made understandable by Figure 7.17, in which the upper waveform is the received signal for $d = d_0 = 30$ cm, and the lower waveform for $d = d_0 = 35$ cm. The character of the diffraction and the double reflection are nearly identical, but the reflected signal is superimposed with the ridge reverberation and can result in constructive or destructive interference. Figure 7.16 shows the backscatter plotted as dB (ref mirror) for the "large" ridge, and the results are not significantly different than in Figure 7.15. At 31 kHz, Figure 7.16 is nearly flat at long ranges implying that reflection is the dominant effect at low frequency, while at 62 and 93 kHz, the curves are not linear, which implies that backscatter from the ridge is just as important as reflection from the smooth plate at higher frequency.

3. Frequency Dependence

The frequency dependence experiment using the "large" ridge produced the only meaningful results. The backscatter was measured for nine frequencies at grazing angles $\theta = 10^\circ$ and $\theta = 20^\circ$ from the horizontal. Typical received waveforms had the same characteristics as the horizontal probe measurements using the "large" ridge (Figure 7.18).

Since the source and receiver were at shallow grazing angles and a range of 50 cm from the ridge crest, the back corner of the ridge (point C on Figure 7.18) was in the

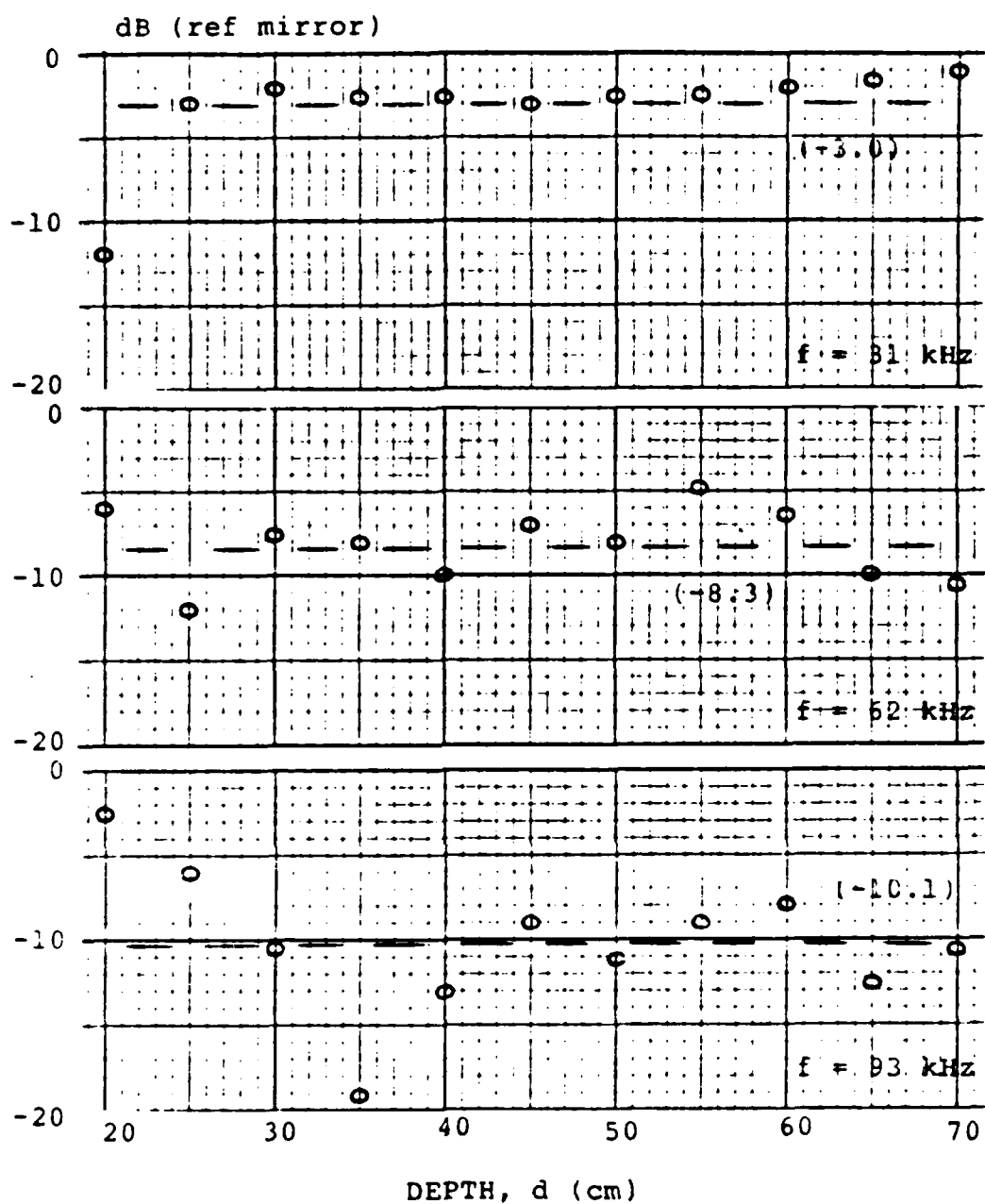


Figure 7.16: Plot of dB (ref mirror) versus depth, d (cm), for the vertical probe experiment using the "large" ridge. (mean value shown in parentheses)

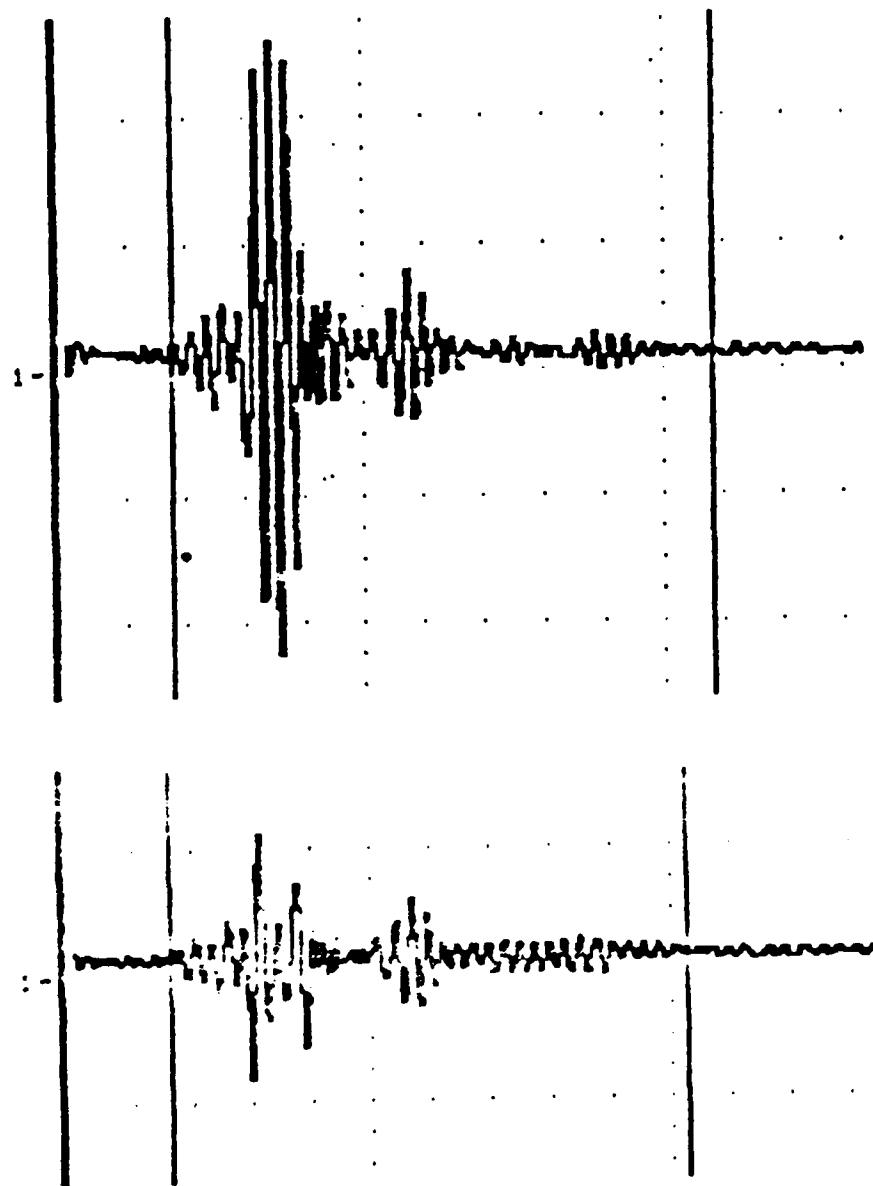


Figure 7.17: Comparison of two waveforms for the vertical probe using the "large" ridge. The upper figure is the same as Figure 7.13, $d = 30$ cm. The lower figure ($d = 35$ cm) shows how the ridge reverberation destructively interferes with the "ice"-air reflection.

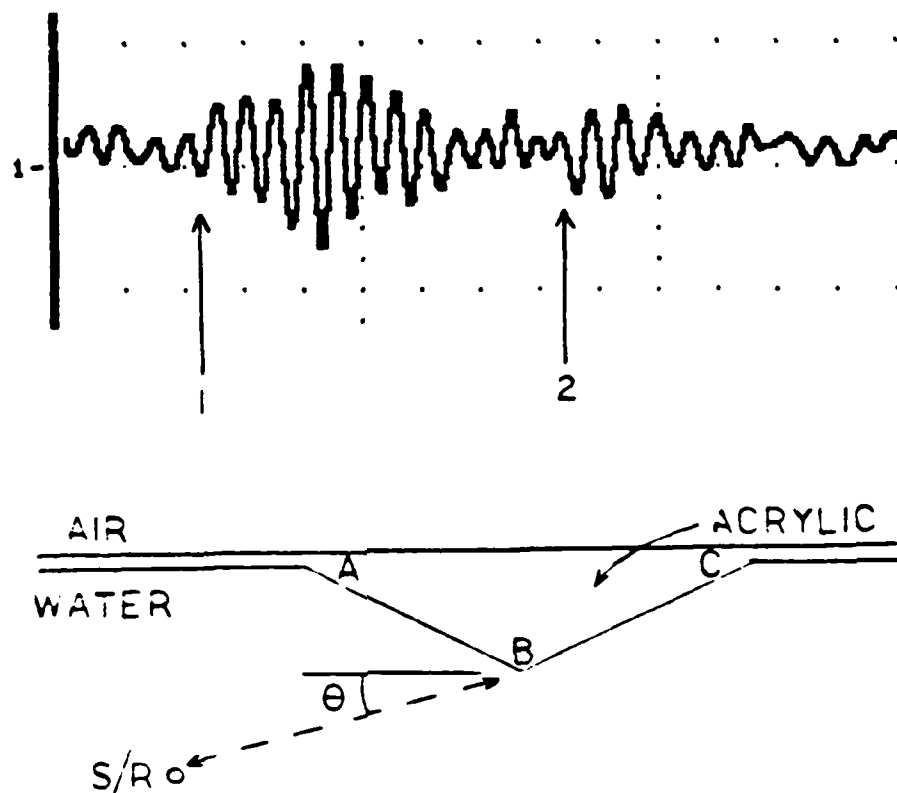


Figure 7.18: Typical received waveform for the frequency dependence experiment using the "large" ridge.

($f = 93$ kHz, $N = 6$ cycles, $r = 50$ cm,
 $\theta = 10^\circ$, 200 mV scale)

(1) = diffraction from the ridge crest
 at point B

(2) = reflection of mode-converted energy
 from point C

geometrical shadow. The backscatter consisted primarily of diffraction from points A and B, and the plot of BSS versus frequency, Figure 7.19, showed an interference pattern due to those two backscattered components. For this source/receiver geometry, the behavior of the BSS can be explained by accounting for the phase difference between the two contributions:

$$\text{phase difference} = kH/\cos\theta = n\pi,$$

where k is the wave number, H = the difference in path length from the source/receiver to point A or B, and θ is the grazing angle. Figure 7.20 shows a plot of BSS versus phase difference, $kH/(\pi\cos\theta)$, and it becomes apparent that the peaks occur approximately for even multiples of π (constructive interference), while the troughs occur at odd multiples of π (destructive interference).

4. Elevation Angle Dependence

The geometry, source frequencies and modelling technique for the "large" ridge were exactly the same as those described for the "typical" ridge. In this case, however, the height of the ridge facet, $H = 6.82$ cm, resulted in height to wavelength ratios of:

$$H/\lambda_1 = 2.9$$

$$H/\lambda_1 = 4.32.$$

The magnitude of the backscattering strength was again plotted as a function of angle and compared to the theoretical

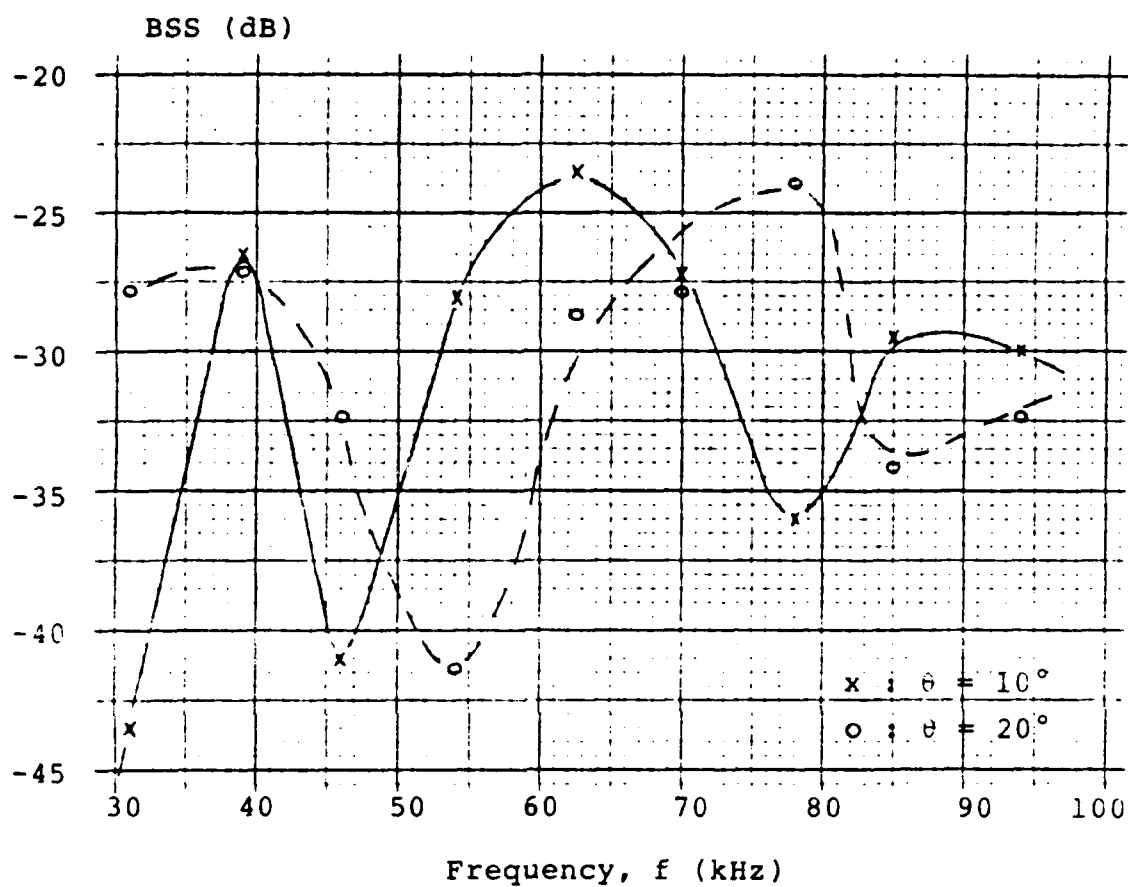


Figure 7.19: Plot of BSS versus frequency, f (kHz), for the frequency dependence experiment using the "large" ridge. ($r = 50$ cm, $\theta = 10^\circ$, 20°)

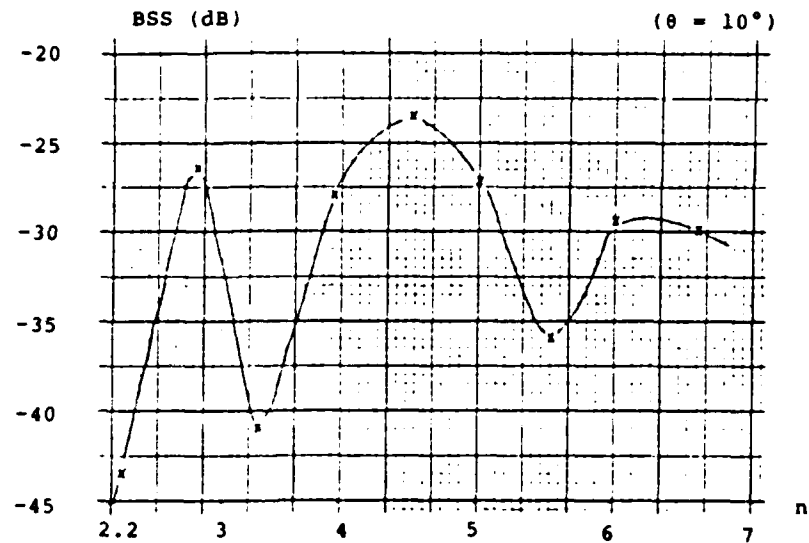


Figure 7.20 (a)

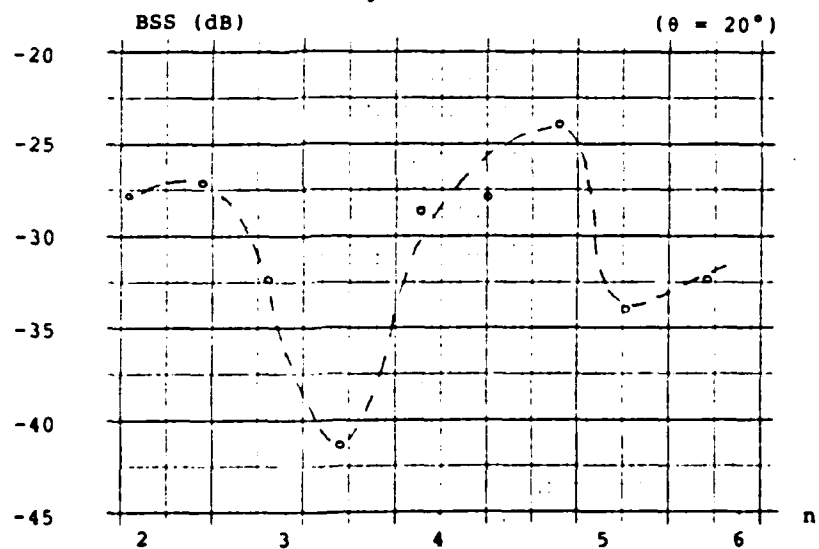


Figure 7.20 (b)

Figure 7.20: Plot of BSS versus phase difference

$$n = \left[\frac{kH}{\pi \cos \theta} \right]$$

for the frequency dependence experiment using the "large" ridge.

directivity pattern for the facet acting as a rectangular piston transducer, as shown in Figure 7.21.

Since the height of the piston face was relatively large compared to a wavelength for the frequencies used, the experimental results were in excellent agreement with the theoretical directivity pattern. Biot-Tolstoy diffraction occurred from the three corners of the ridge, but was small in comparison to the radiation of mode-converted reverberation from the larger rectangular apertures. For the "large" ridge, note that the value of backscatter for $\theta = 90^\circ$ shows good agreement: since the ridge was large in width, it scattered effectively so that the measured backscatter can be attributed primarily to the ridge diffraction instead of reflection from the ice sheet behind the ridge.

D. "STEEP" RIDGE RESULTS

The "steep" ridge used for this experiment was designed to model a possible pressure ridge which could be found in the Central Arctic basin. It was the same height, but twice the slope as the typical ridge, so it was designed to show the dependence of backscatter on ridge slope.

1. Horizontal Probe

For the horizontal probe using the "steep" ridge, the source/receiver were positioned 1.6 cm below the ice plate to correspond with the depth of the ridge crest. Figure 7.22 shows a typical received waveform. The received

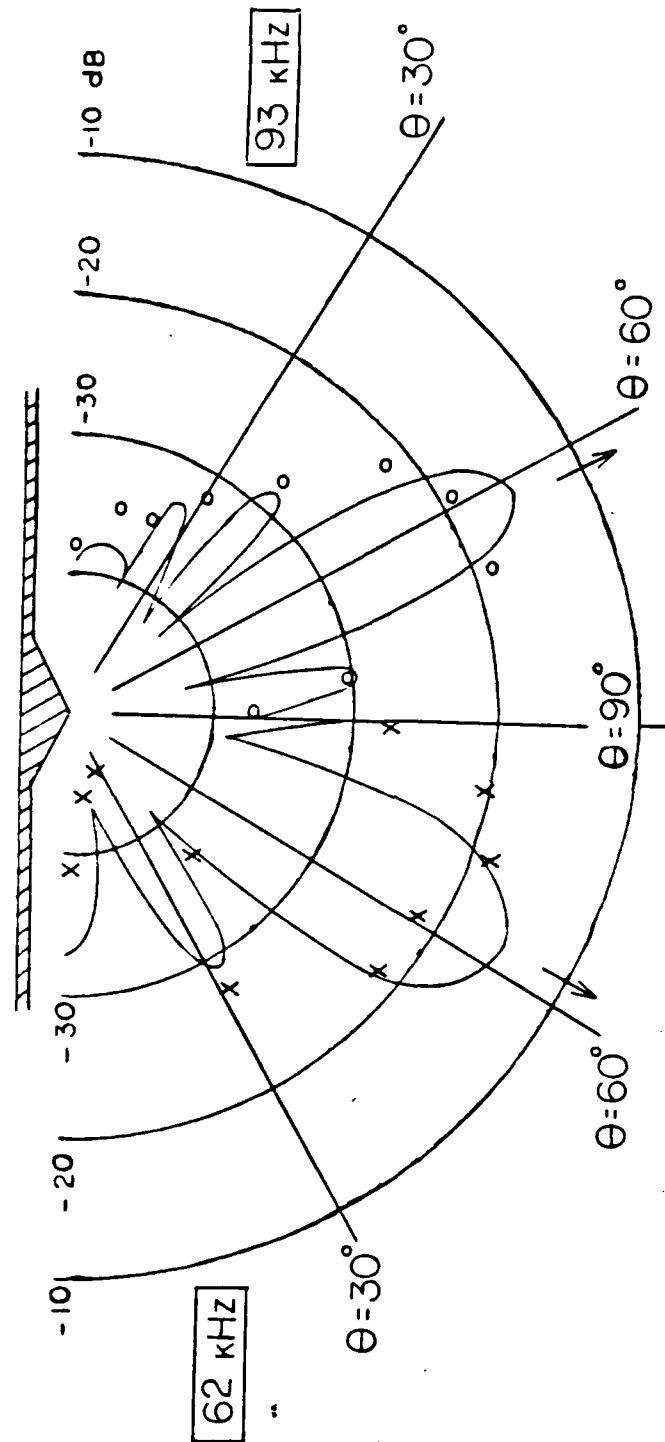


Figure 7.21: Elevation angle dependence of the total backscatter strength for the "large" ridge compared to the directivity pattern of facet radiation from an equivalent rectangular piston. The arrow shows the piston axis for each ridge facet. (Two frequencies are shown, $r = 50$ cm.)

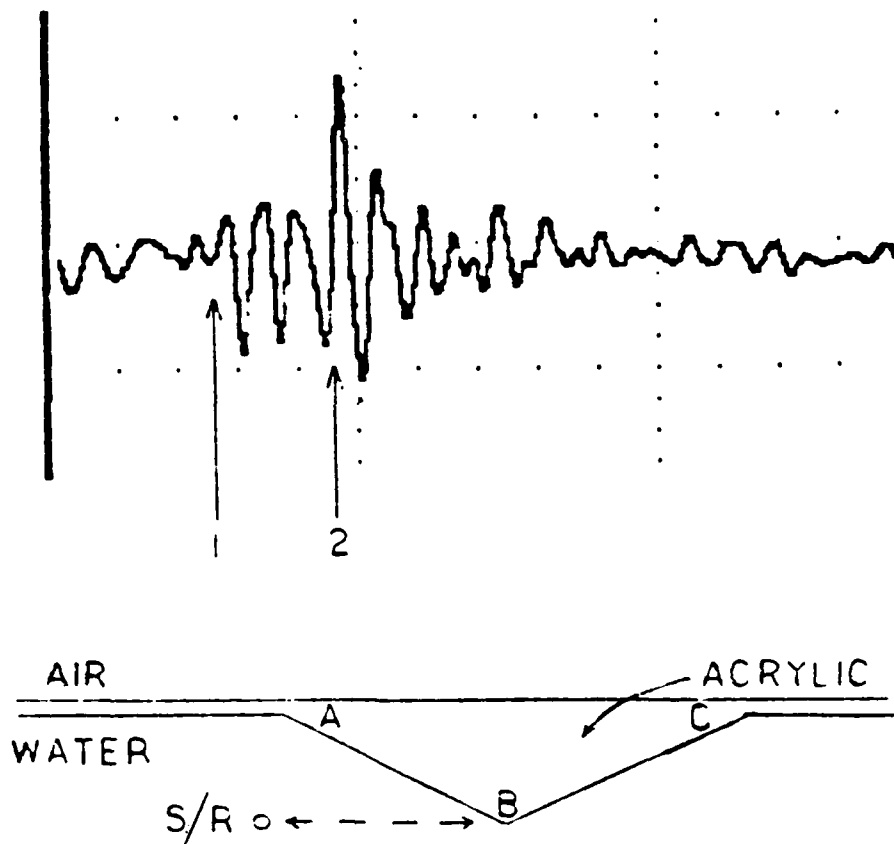


Figure 7.22: Typical received waveform for the horizontal probe experiment using the "steep" ridge.

($f = 62.5$ kHz, $N = 2$ cycles, $r = 40$ cm, 500 mV scale)

(1) = Backscatter from front facet (AB)

(2) = Mode conversion and reflection from back facet (BC)

signals in all cases were composed of the two parts shown: an initial arrival which agreed in time with reflection or diffraction from the ridge facet closest to the source/receiver; and a second arrival which agreed with the propagation time required for an acoustic signal to be mode-converted into the ridge, reflect from the back facet of the ridge, and return by the reverse path. Due to the small dimensions of the "steep" ridge and the positioning error of the source/receiver, it was impossible to positively identify which part of the ridge caused each backscattered component, so the backscatter was generalized to the front facet and the back facet contributions. The signals had similar characteristics to those for the horizontal probe from the "typical" ridge, with the difference that the backscatter from the near and far facets were separated by a smaller time interval in the case of the "steep" ridge.

Figure 7.23 shows the divergence characteristic for the horizontal probe from the "steep" ridge. Equation (7.1) was used to calculate the BSS, assuming the backscatter from the ridge diverged spherically. The curve of BSS versus range shows oscillating and decreasing BSS with increasing range for the "steep" ridge. The source/receiver was the same depth below the plate as for the "typical" ridge horizontal probe, so both show similar surface interference

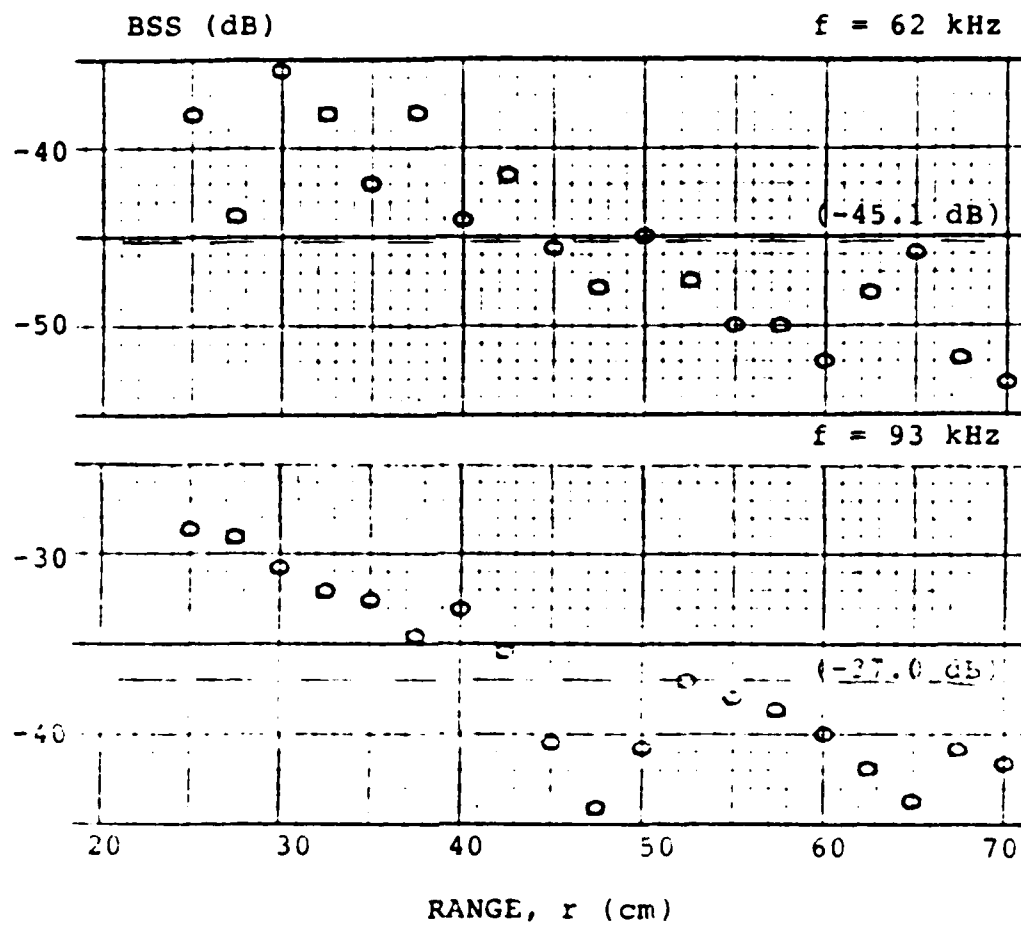


Figure 7.23: Plot of BSS versus range, r (cm), for the horizontal probe experiment using the "steep" ridge. (mean value of BSS in parentheses)

effects. The average values of BSS are lowest for the "steep" ridge and highest for the "large" ridge.

2. Vertical Probe

In the vertical probe experiment on the "steep" ridge, fewer effects of the characteristic behavior of the backscatter were apparent than for the "typical" and the "large" ridge vertical probes. Figure 7.24 shows a received waveform. Notice that the majority of the signal appeared to be reflection from the ice plate. There was no measurable diffraction from the crest of the ridge, and there was significantly less reverberation from the ridge reradiating after the reflected signal.

Figure 7.25 is a plot of the BSS versus depth below the ridge for the vertical probe, calculated using Equation (7.1). Since the BSS was nearly independent of depth, the assumption of spherical divergence from a point on the ridge must have been valid. In this case, since reverberation was not significant, there was less variation of the backscattered values about the mean than was observed for the "typical" ridge. It is noteworthy that the plot of BSS versus depth decreases for shallow depths. Using Equation (7.1) to calculate BSS presupposed that the divergence would be spherical. BSS values less than the average for the shallow depths indicates that the divergence was overcompensated for, and that the actual divergence for the

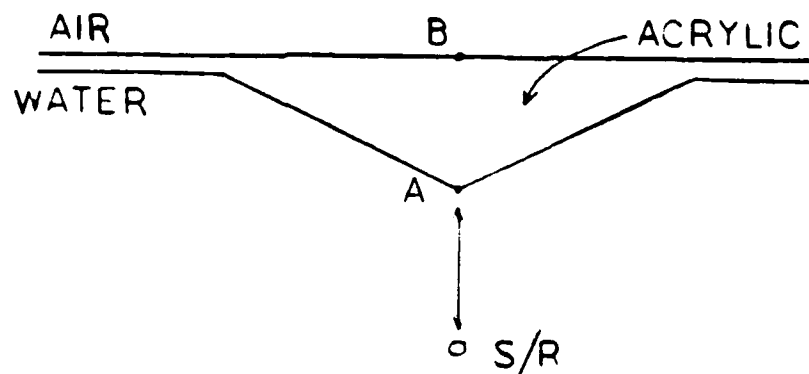
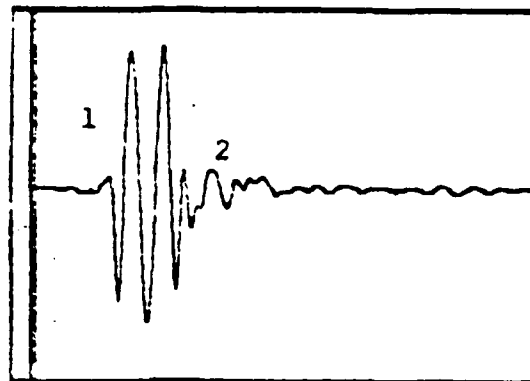


Figure 7.24: Typical received waveform for the vertical probe experiment using the "steep" ridge.

($f = 62.5$ kHz, $N = 2$ cycles, $d = 40$ cm, 2.0 V scale)

1 = reflection from "ice"-air interface (path S-A-B-A-R)

2 = reradiation of ridge reverberation

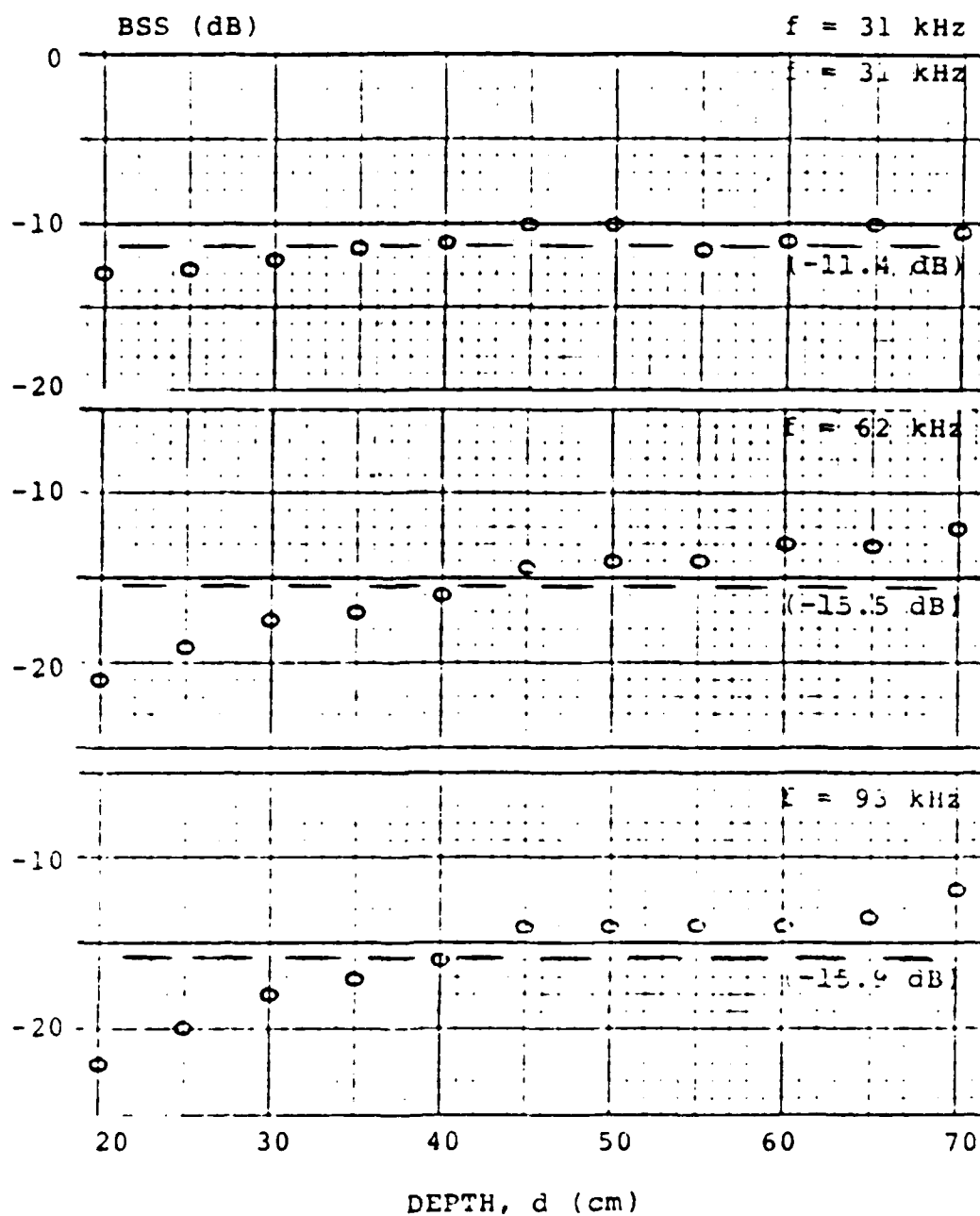


Figure 7.25: Plot of BSS versus depth, d (cm) for the vertical probe experiment using the "steep" ridge. (mean value of BSS in parentheses)

"steep" ridge was probably dominated by reflection. When the scattering was calculated using Equation (7.2) and plotted in terms of dB (ref mirror) as in Figure 7.26, experimental agreement with theory was excellent: the small size of the "steep" ridge resulted in scattering that was dominated by the reflection from the smooth plate.

3. Frequency Dependence

The frequency dependence experiment using the "steep" ridge produced no meaningful results.

4. Elevation Angle Dependence

The geometry, source frequencies and modelling technique were exactly the same as those described for the "typical" ridge. In this case, however, the height of the ridge facet, $H = 1.92$ cm, resulted in height to wavelength ratios of:

$$H/\lambda_1 = 0.81 \qquad H/\lambda_2 = 1.21.$$

The magnitude of the backscattering strength was again plotted as a function of angle and compared to the theoretical directivity pattern for the facet as a rectangular piston transducer, shown in Figure 7.27.

The theoretical directivity pattern and the measured backscattering strength as a function of angle had their poorest agreement in this case of the "steep" ridge. The characteristic dimension of the piston transducer was approximately equal to the wavelength, so the piston behaved

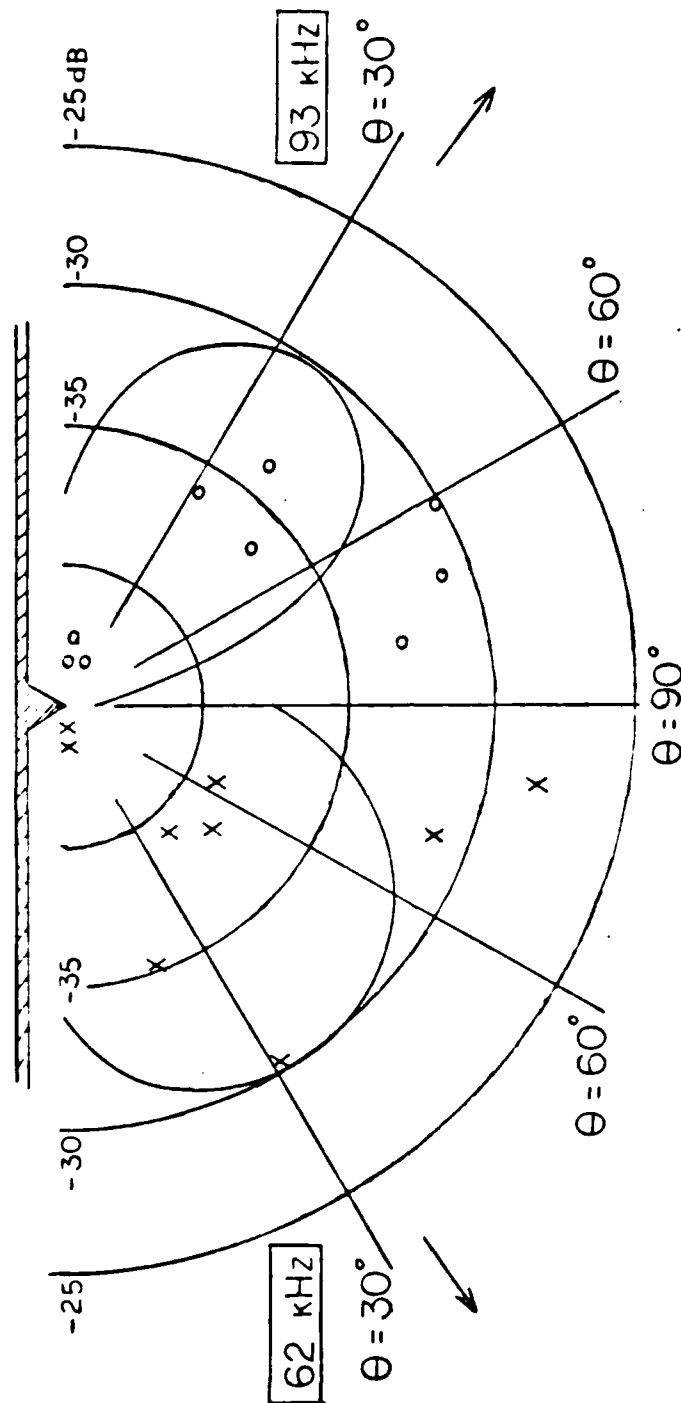


Figure 7.27: Elevation angle dependence of the total backscatter strength for the "steep" ridge compared to the directivity pattern of facet radiation from an equivalent rectangular piston. The arrow shows the piston axis for each ridge facet. (Two frequencies are shown, $r = 50$ cm.)

in a highly non-directional manner. The radiation from the small rectangular apertures was inefficient, and Biot-Tolstoy diffraction which was not accounted for in the theoretical comparison was probably significant.

The backscattered data were analyzed as before, with interfering reflections subtracted at nearly normal grazing angles. At normal incidence ($\theta = 90^\circ$), the plate reflection and ridge backscatter again overlapped, resulting in a measured value much larger than predicted. Just as in the vertical probe experiment for the "steep" ridge, the effective backscatter at normal incidence is insignificant compared to the plate reflection.

E. SUMMARY OF RIDGE RESULTS

Based on the results of the backscatter measurements for the four experiments on each of the three ridges, the following generalizations can be made.

1. Horizontal Probe

For all three ridges, the plot of BSS versus range generally obeyed a spherical divergence characteristic, which indicated that the majority of the backscatter occurred from an effective point on the ridge in the least time region. The "large" ridge produced the highest BSS and the best agreement with spherical divergence. The "typical" and "steep" ridges were both half the height of the "large" ridge, so the source/receiver was positioned closer to the

plate for their horizontal probes, and surface interference problems degraded the agreement with the spherical divergence characteristic in those cases.

2. Vertical Probe

Received waveforms for vertical probe experiments typically consisted of three components: Biot-Tolstoy diffraction from the ridge crest; mode-conversion and reflection from the "ice"-air interface; and a double reflection within the ridge prior to reradiation. The "large" ridge resulted in the greatest separation in time between those three components, so each could be analyzed individually; the "typical" ridge showed evidence of each component, although not well separated in time; and the "steep" ridge only showed signs of reflection, since the size of the diffracted and double reflected signals were negligible. The backscatter from all three ridges generally obeyed a spherical divergence characteristic beyond some critical depth below the ridge. Variation in the divergence characteristic at different source/receiver depths was explained by the destructive interference of the reradiation of mode-conversion induced ridge reverberation with the reflected portion of the backscatter, as shown in Figure 7.17.

With the source/receiver positioned below the ridge, the received signals were a combination of sound scattered

from the ridge, as well as the reflection from the smooth plate. When scattering from the ridge is most important, Equation (7.1) for the backscattering strength is a more appropriate comparison with theory; when reflection from the smooth plate is important, Equation (7.2) for dB referenced to a mirror should be used. In the case of the "large" ridge, scattering was just as important as reflection, so experimental agreement with theory was nearly the same when using either Equation (7.1) or Equation (7.2). At the other extreme, the small size of the "steep" ridge meant that reflection was much more important than backscatter. As a result, experimental agreement with theory was better when plotted in terms of dB ref. mirror.

3. Frequency Dependence

The frequency dependence measurement of the "large" ridge produced the only meaningful results. For the shallow grazing angles of this experiment, diffraction occurred from two corners of the ridge which produced an interference effect due to their slightly different path lengths in comparison to a wavelength. The "typical" and "steep" ridges produced inconsistent results, possibly due to the increased surface interference problems associated with those two ridges for their smaller height.

4. Elevation Angle Dependence

Each of the ridges was modelled as a finite reflector or aperture with a height corresponding to the ridge slant face. The backscatter consisted of the reflection and reradiation of sound energy from the rectangular aperture, as well as diffraction from the corners of the ridge. The BSS was compared to the directivity pattern for an equivalent rectangular piston. Experimental agreement with theory was good for the "large" ridge because radiation from its large aperture (in comparison to a wavelength) dominated the diffraction from the ridge corners. Agreement with theory in the case of the "typical" or "steep" ridge was not as good since the diffraction increased in relative importance as the radiation became less efficient for these smaller rectangular apertures. The BSS was greater for larger ridges: doubling the slope of the "typical" ridge reduced the BSS by 10 dB, while doubling the height of the "typical" ridge increased the BSS by 5 dB.

Finally, it was observed that diffraction theory did not account for all of the energy backscattered from a ridge. During the frequency dependence experiment for a grazing angle of 20° , there were no surface interference effects and no interference of specular reflection from the smooth plate, so the geometry was optimized to measure diffraction alone. The additional energy was due to the

reradiation of mode-conversion induced reverberation from the ridge, as shown in Figure 7.28.

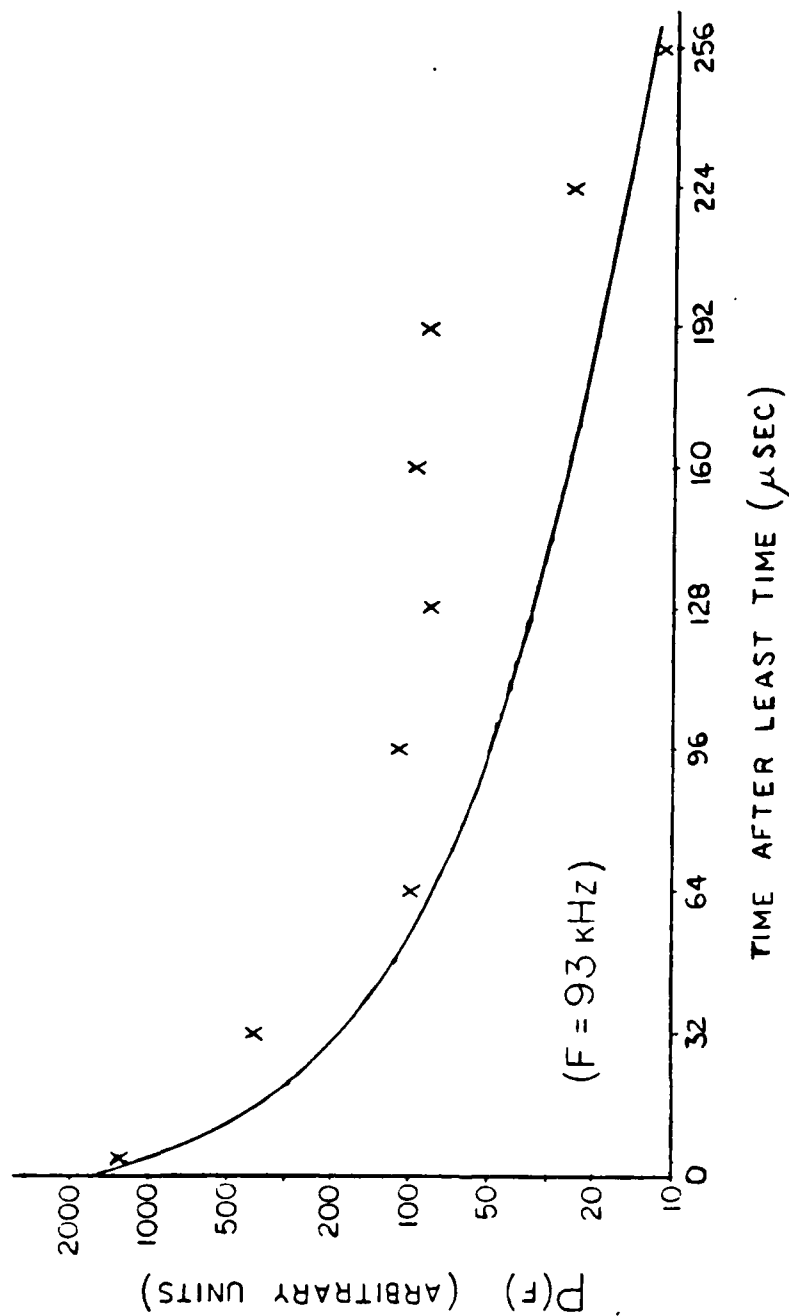


Figure 7.28: Total experimental backscatter compared to diffraction theory for the large wedge. Solid line is rigid wedge diffraction theory.

($f = 93$ kHz, $N = 3$ cycles, $\theta = 20^\circ$, $r = r_0 = 50$ cm)

VIII. CONCLUSIONS

Due to the physical characteristics of the laboratory acrylic model and the ability to scale the laboratory dimension-to-wavelength ratio to match typical Arctic dimension-to-wavelength ratios, it is possible to study the low frequency scattering properties of the Arctic ice canopy under controlled laboratory conditions. These experiments were designed to study the behavior of two particular scattering features of the Arctic: the backscatter from the trailing edge of an open Arctic lead and the backscatter from Arctic pressure ridges.

The results of these experiments can be summarized as follows:

1. The Arctic ice canopy and the laboratory model are acoustically non-rigid, since they do not have an infinite specific acoustic impedance mismatch with water. The consequence is that a significant amount of acoustic energy incident upon such a surface will penetrate and be mode-converted to solid-borne vibrations within the solid material.
2. Due to the effects of mode-conversion, diffraction theory alone is not sufficient to predict the amount of energy which will be backscattered from the

trailing edge of an open lead. Some of the acoustic energy incident on the underside of the Arctic ice canopy will generate solid-borne compressional and shear waves which propagate along the plate and reradiate energy back into the water upon reaching a discontinuity. When superimposed with the diffraction, this reradiated energy results in backscattered signals larger than predicted by diffraction theory alone. Individual components of the backscattered signal were identified by establishing a source/receiver geometry which separated them by time of arrival. Additionally, the presence of head wave radiation from a smooth floating plate was discovered and measured.

3. The backscatter from Arctic pressure ridges is affected by the amount of mode-conversion. Diffraction occurs from the corners of the ridge, but a significant amount of the incident acoustic energy also produces mode-conversion induced reverberation within the ridge which reradiates energy. The majority of the backscatter occurs in the least time region of the ridge. Also, for ridges large compared to an acoustic wavelength, reflection and the reradiation of ridge reverberation dominate the diffracted portion of the backscatter. Consequently, the characteristic

behavior of the backscatter resembles the directivity pattern for rectangular piston radiation from the slant face of the ridge that is ensonified.

APPENDIX A: PLANAR TRANSDUCER FOR MODE CONVERSION STUDY

When the scattering characteristics of sound from the acoustically significant features of the acrylic Arctic ice model are well understood, many of the same experiments will be repeated in a layered waveguide to study the propagation and scattering of sound in a shallow water "Arctic" environment. In preparation for those experiments, it was necessary to build a planar transducer capable of effective transmission of normal modes of vibration in a waveguide. There was also an application for this transducer in the mode conversion study experiment.

A layered waveguide is a water layer which is bounded on the bottom by a half space of sediment, and by a half space of air on top, with the characteristics described by Clay and Medwin (1977). Effective transmission of a single mode in a waveguide is possible if the driving elements are located to reinforce the mode pressure maxima, and if the phase between adjacent maxima is shifted 180° . Typical vertical pressure profiles for the first three normal modes in a layered waveguide are shown in Figure A.1. Since a greater number of transducer elements will provide better control of the pressure profile, a twelve channel amplifier was designed to provide twelve independent channels with separate phase and amplitude control from a single input.

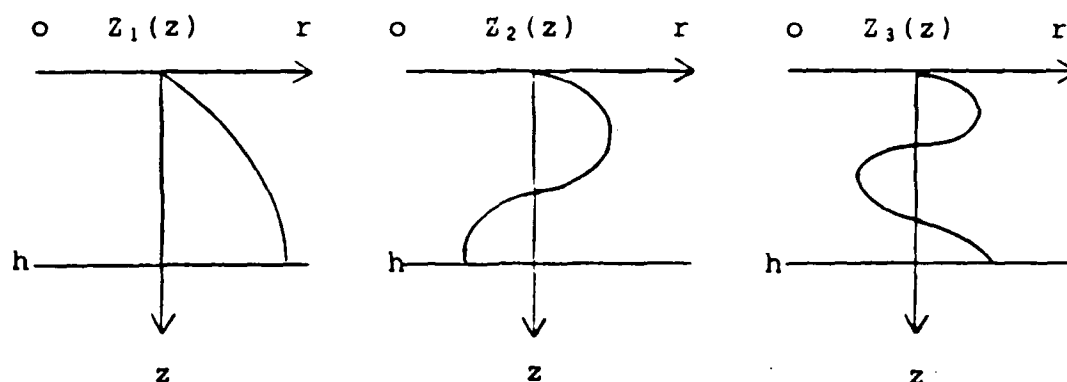
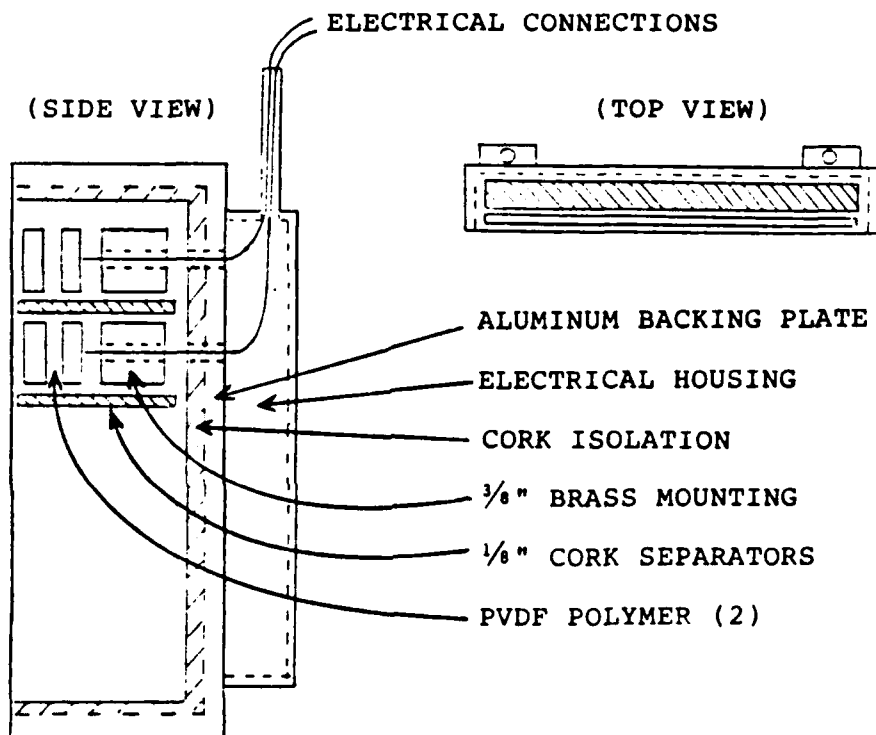
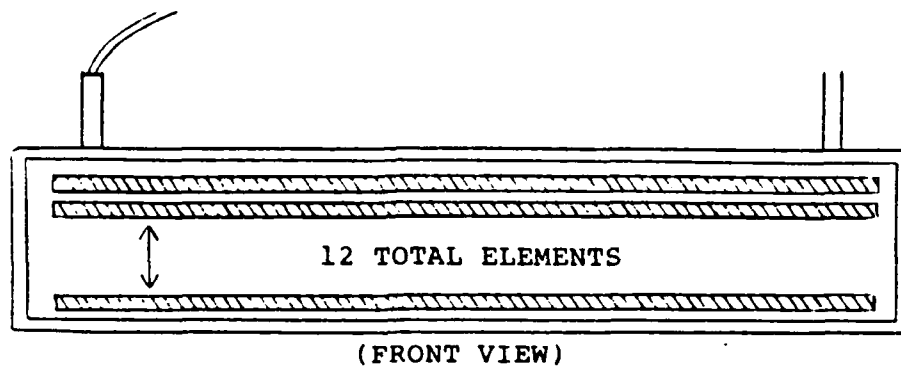


Figure A.1: Vertical pressure profiles, $Z_m(z)$, for the first three normal modes in a layered waveguide. (m is the mode number)

The term "phase" is loosely applied, since only a 180° phase shift is required between elements to produce the necessary excitation. Figure A.2 is an electrical schematic of the amplifier design. The amplifier uses 324C general purpose operational amplifiers (with four opamps per chip). The first chip uses only two of its opamps, and provides the signal to the inverted and non-inverted buses of the amplifier. The 100K potentiometer is used to ensure the voltage on each electrical bus is identical. The second stage amplifiers provide amplitude control via the 250K potentiometer, and phase control via the toggle switch for each channel.

Construction of the transducer was made possible by materials provided by the Raytheon Corporation. The active material for each element is the semicrystalline polymer



DIMENSIONS

CORK INSULATION = $\frac{1}{4}$ "

CORK SEPARATORS = $\frac{1}{8}$ "

BRASS MOUNTING = $\frac{3}{8}$ " x $\frac{3}{8}$ " x 24"

PVDF ELEMENTS = 0.022" x $\frac{3}{8}$ " x 23"

ACTIVE TRANSDUCER

HEIGHT = 5.9"

WIDTH = 23.0"

Figure A.2: Planar Transducer Design

polyvinylidene fluoride (PVDF). It was chosen for its flexibility and toughness, its good acoustic impedance match with water, and for the ease with which it can be cut and handled. Each element was constructed by gluing two strips ($3/8"$ x $24"$ x $0.022"$) of the copper-plated PVDF material to a $3/8"$ brass bar to increase the volume displacement, and therefore the projecting power, of each element. The twelve elements were stacked and glued in an aluminum casing with cork strips positioned to physically isolate elements from the casing and from each other to damp vibrations which might be transmitted between elements. Finally, the entire transducer was sealed with Emerson and Cummings Eccothane 7534, a low viscosity, medium hardness encapsulant to waterproof the transducer. A schematic of the transducer design is shown in Figure A.3.

The performance of the transducer was tested by making near-field pressure response measurements in air, applying the theory of complex apertures described by Ziomek (1985). The complex frequency response in the near-field was measured by positioning a $1/2"$ Bruel and Kjaer condenser microphone at a height of $1/2"$ over 276 uniformly spaced positions across the active face of the transducer. The measurements were repeated for three different frequencies of interest and with various amplifier configurations. The transducer response at 20 kHz for a mode 1 and mode 2

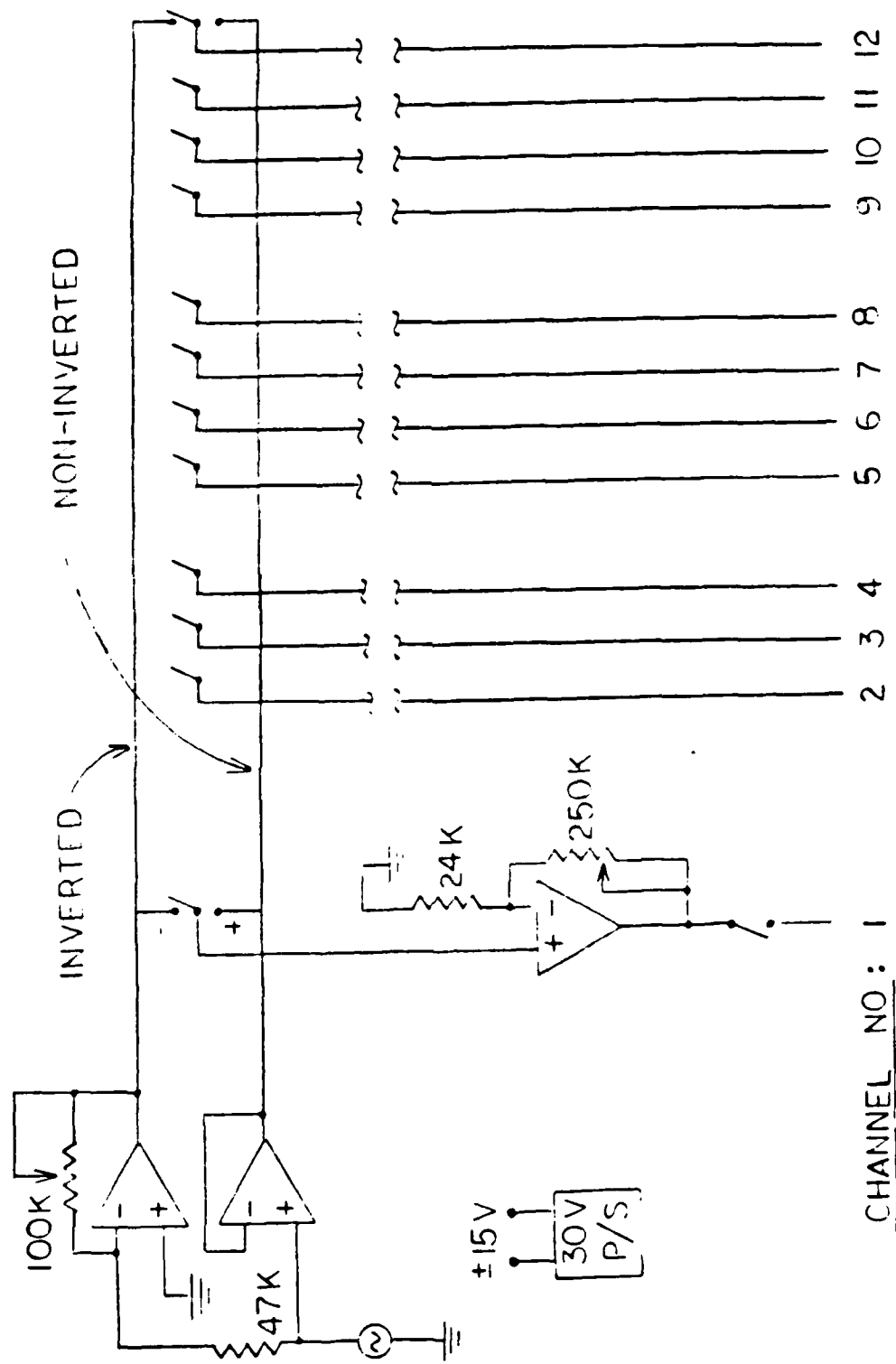


Figure A.3: Twelve channel amplifier design for planar transducer.
(All twelve channels are identical to channel 1.)

excitation is shown in Figures A.4 and A.5. By the theory of complex apertures, if the frequency response can be measured for a given electrical input, then the acoustic response of the transducer is known.

The PVDF transducer was used for an application in the mode conversion study experiment. With all of the elements in phase and equally amplitude weighted, the transducer was positioned below the smooth acrylic plate at the critical angle for compressional wave excitation in the plate. With compressional waves efficiently excited by the plane waves of the source, it was possible to effectively measure the plate compressional wave reradiation into the water from the end of the plate and as head waves from the water-acrylic interface.

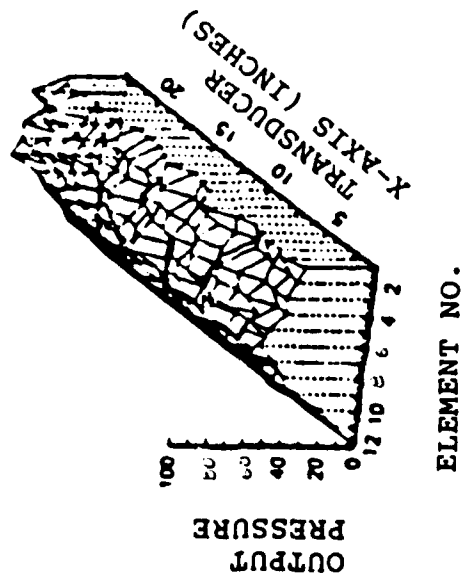
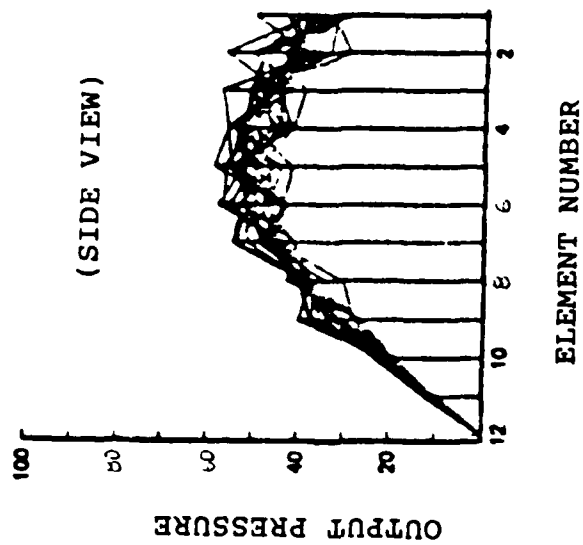


Figure A.4: Planar transducer pressure response with all twelve elements amplitude weighted to excite the first natural mode of vibration in the waveguide. (Pressure in arbitrary units.)

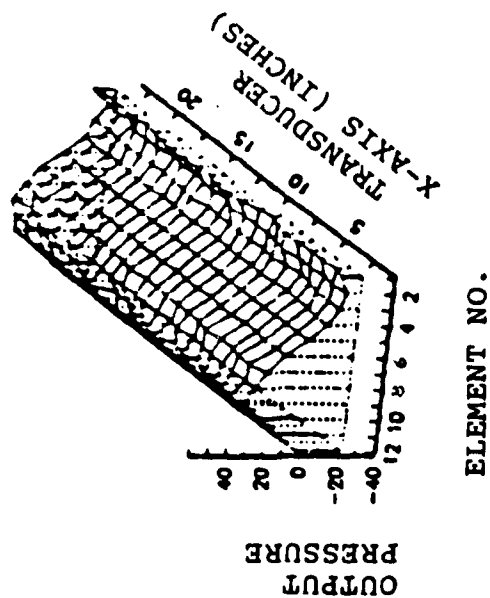
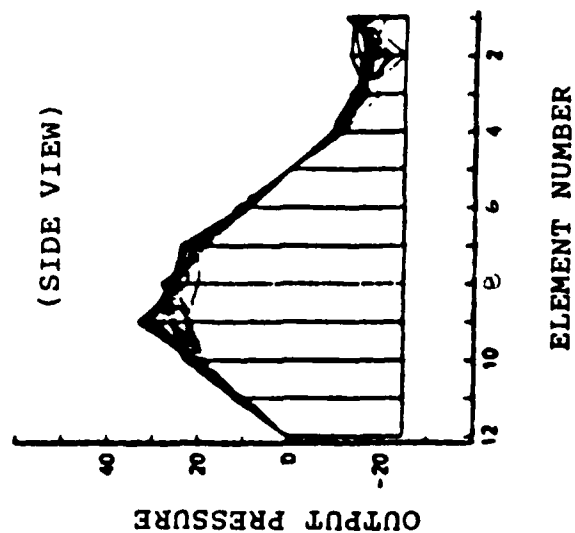


Figure A.5: Planar transducer pressure response with all twelve elements amplitude weighted to excite the second natural mode of vibration in the waveguide. (Pressure in arbitrary units.)

APPENDIX B: FLEXURAL WAVE THEORY

Flexural waves in a plate propagate by a bending motion about the neutral, undistorted axis. Portions of the plate above and below the neutral axis undergo a combination of compressional and shear deformation as the wave propagates. Flexural waves are also known as bending waves. Different frequencies will travel at different speeds, so propagation of flexural waves in a plate is dispersive, and a waveform will change its shape with distance of travel. Flexural waves in a plate will be generated for frequencies $kh < 1$, where k = horizontal wavenumber and h = plate thickness.

According to Ross (1976), when classical elastic theory is applied to solid plates, longitudinal waves have a phase speed given by:

$$C_p = \left[\frac{Y}{\rho(1 - \sigma^2)} \right]^{\frac{1}{2}}$$

The plate longitudinal phase speed depends only on properties of the material. Vibrations in a thick plate are quite complicated, but if frequencies are restricted to the small kh criterion, then the analysis of thin plate vibrations is possible. For a harmonic disturbance in the plate, the Timoshenko equation for beams is used to describe the flexural motion:

$$\frac{\partial^2 y}{\partial t^2} + \frac{c_p^2 h^2}{12} \cdot \nabla^4 y - \frac{(\Gamma_p + 1)h^2}{12} \cdot \nabla^2 \frac{\partial^2 y}{\partial t^2} + \frac{\Gamma_p h^2}{12 c_p^2} \cdot \frac{\partial^4 y}{\partial t^4} = 0$$

where h is the plate thickness (meters), c is the longitudinal or compressional wave speed in the plate, y is the plate displacement perpendicular to the surface, and Γ_p is the shear parameter for the plate. The shear parameter,

$$\Gamma_p = \frac{Y}{KG(1 - \sigma^2)}$$

is a non-dimensional number which relates Young's Modulus (Y) to the Shear Modulus (G). The constant of proportionality for a plate, $K_p = 0.76 (1 + 2/5\sigma)$, accounts for physical distortions in the plate due to the effects of shear. There are four solutions to the Timoshenko equation, two of which are imaginary, and the general solution can be expressed as (Ross 1976):

$$y = [Ae^{-ikx} + Be^{ikx} + Ce^{-ijx} + De^{ijx}] e^{i\omega t}$$

where $\omega = 2\pi f$, k is the flexural wave number ω/v_f , v_f is the flexural wave phase speed, $j = ik$, $i = (-1)^{1/2}$, and A , B , C , and D are the complex coefficients found from the boundary conditions.

The flexural wave group and phase speeds for harmonic excitations of a thin plate can be found by substituting the general harmonic solution into the Timoshenko equation for

thin plates. The resulting equation, when rearranged to form a quadratic equation in terms of radian frequency, ω , is

$$\left(\frac{\Gamma_p h^2}{c_p^2 12} \right) \omega^4 - \left[(\Gamma_p + 1) \left(\frac{h^2}{12} \right) k^2 + 1 \right] \omega^2 + c_p^2 \left(\frac{h^2}{12} \right) k^4 = 0.$$

Solving the quadratic equation for the flexural wave phase speed results in

$$v_f^2 = \frac{1}{2A} \left[-B + \sqrt{B^2 - 4AC} \right] \quad (B.1)$$

$$A = \frac{1}{\omega^2} - \frac{\Gamma_p h^2}{12 c_p^2}$$

$$B = (\Gamma_p + 1) h^2 / 12$$

$$C = -c_p^2 h^2 / 12.$$

It has been shown theoretically by Ross (1976) and experimentally by Denny and Johnson (1986), that in the low frequency limit, the flexural wave phase speed is proportional to the square root of the frequency:

$$v_f = \left[\frac{\omega c_p h}{\sqrt{12}} \right]^{\frac{1}{2}}$$

Also, at high frequencies the flexural wave speed becomes constant, so flexural waves are then non-dispersive:

$$v_f^2 = \frac{c_p^2}{\Gamma_p} \approx 0.92 c_s$$

where c_s = the shear wave speed in the plate. Similarly, when Equation B.1 is solved for the flexural wave group speed, it is seen that the group speed is twice the phase speed at low frequencies:

$$v_g = 2 \cdot \left[\frac{\omega c_p h}{\sqrt{12}} \right]^{\frac{1}{2}}$$

and that group and phase speeds are equal at high frequencies,

$$v_g = v_f = \frac{c_p^2}{\Gamma_p} \approx 0.92 c_s.$$

LIST OF REFERENCES

Ackley, S.F., Cold Regions Research and Engineering Laboratory Report 76-18, Thickness and Roughness Variations of Arctic Multiyear Sea Ice, Table II, p. 9, June 1976.

Beranek, L. L., Noise and Vibration Control, McGraw-Hill Book Company, New York, New York, 1971.

Biot, M. A. and Tolstoy, I., "Formulation of Wave Propagation in Infinite Media by Normal Coordinates with an Application to Diffraction", J. Acoust. Soc. Am., 29, pp. 381-391, 1957.

Bourke, R. H., Department of Oceanography, Naval Postgraduate School, Monterey, California (personal communication).

Clay, C. S. and Medwin, H., Acoustical Oceanography: Principles and Applications, John Wiley & Sons, Inc., New York, New York, 1977.

Denny, P. L. and Johnson, K. R., Underwater Acoustic Scatter from a Model of the Arctic Ice Canopy, M.S. Thesis, Naval Postgraduate School, Monterey, California, December 1986.

Diachok, O. I., Naval Oceanographic Office Technical Note No. 6130-4-74, Effects of Sea Ice Ridge Characteristics on Under-Ice Reflection Loss in Arctic/Subarctic Waters, p. 11, August 1974.

Hibler, W. D. III, Weeks, W. F. and Mock, S. J., "Statistical Aspects of Sea-Ice Ridge Distributions", J. Geophys. Res., 77, pp. 5954-5970, 1972.

Hunkins, K., "Seismic Studies of Sea Ice", Journal of Geophysical Research, 65, pp. 3459-3472, 1960.

Kinsler, L. E., Frey, A. R., Coppens, A. B. and Sanders, J. V., Fundamentals of Acoustics, 3rd ed., John Wiley and Sons, Inc., 1982.

McCammon, D. F. and McDaniel, S. T., "The Influence of the Physical Properties of Ice on Reflectivity", Journal of the Acoustical Society of America, 77, pp. 499-507, 1985.

Medwin, H., "Shadowing by Finite Noise Barriers", Journal of the Acoustical Society of America, 69, pp. 1060-1064, 1981.

Medwin, H., Childs, E. and Jebsen, G. M., "Impulse Studies of Double Diffraction: A Discrete Huygens Interpretation", Journal of the Acoustical Society of America, 72, pp. 1005-1013, 1982.

Medwin, H. and Novarini, J. C., "Backscattering Strength and the Range Dependence of Sound Scattered from the Ocean Surface", Journal of the Acoustical Society of America, 69, pp. 108-111, 1981.

Medwin, H., et al., "Sound Scatter and Shadowing at a Seamount: Hybrid Physical Solutions in Two and Three Dimensions", Journal of the Acoustical Society of America, 75, pp. 1478-1490, 1984.

Myers, J. J., Holme, C. H. and McAllister, R. F., eds., Handbook of Ocean and Underwater Engineering, pp. 1-8, McGraw-Hill Book Co., 1969.

Novarini, J. C. and Medwin, H., "Computer Modeling of Resonant Sound Scattering from a Periodic Assemblage of Wedges: Comparison with Theories of Diffraction Gratings", Journal of the Acoustical Society of America, 77, pp. 1754-1759, 1985.

Ross, D., Mechanics of Underwater Noise, Pergamon Press, New York, New York, 1976.

Schwartz, J. and Weeks, W. F., "Engineering Properties of Sea Ice", Journal of Glaciology, 19, pp. 499-531, 1977.

Wadhams, P., McLaren, A. S. and Weintraub, R., "Ice Thickness Distribution in Davis Strait in February from Submarine Sonar Profiles", Journal of Geophysical Research, 90, pp. 1069-1077, 1985.

Weeks, W. F., Kovacs, A. and Hibler, W. D. III, "Pressure Ridge Characteristics in the Arctic Coastal Environment", Proceedings from the First International Conference on Port and Ocean Engineering under Arctic Conditions, I, pp. 152-183, 1971.

Ziomek, L. J., Underwater Acoustics: A Linear Systems Theory Approach, Academic Press, Inc., Orlando, Florida, 1985.

INITIAL DISTRIBUTION LIST

	No. Copies
1. Defense Technical Information Center Cameron Station Alexandria, Virginia 22304-6145	2
2. Library, Code 0142 Naval Postgraduate School Monterey, California 93943-5002	2
3. Professor H. Medwin, Code 61 Md Department of Physics Naval Postgraduate School Monterey, California 93943	6
4. Prof. R. H. Bourke, Code 68 Bf Department of Oceanography Naval Postgraduate School Monterey, California 93943	1
5. Dr. R. Fitzgerald, Code 4250 A Office of Naval Research 800 N. Quincy Arlington, Virginia 22217	1
6. Mr. R. Obrachta Office of Naval Research 800 N. Quincy Arlington, Virginia 22217	1
7. Capt. Leslie M. Jacobi, USN 20 Eagle Ridge Road Gales Ferry, Connecticut 06335	1
8. Dr. Brad Becken Raytheon Submarine Signal Division P.O. Box 360 Portsmouth, Rhode Island 02871	1
9. Professor C. S. Clay Department of Geology and Geophysics 1215 Dayton St. University of Wisconsin Madison, Wisconsin 53706	1

- | | |
|---------------------------------------------------------------------------------------------------------------------------------------------|---|
| 10. Professor A. B. Baggeroer
Department of Ocean Engineering
Massachusetts Institute of Technology
Cambridge, Massachusetts 02139 | 1 |
| 11. Dr. Warren Denner
Science Applications International Corp.
205 Montecito Avenue
Monterey, California 93940 | 1 |
| 12. Mr. Jacques R. Chamuel
Sonoquest Research
P.O. Box 584
Sudbury, Massachusetts 01776 | 1 |
| 13. Dr. T. C. Yang
Naval Research Lab
3555 Overlook Avenue
Washington, D.C. 20334 | 1 |
| 14. Professor A. A. Atchley
Department of Physics, Code 61 Ay
Naval Postgraduate School
Monterey, California 93940 | 1 |
| 15. Professor S. Garrett, Code 61 Gx
Department of Physics
Naval Postgraduate School
Monterey, California 93943 | 1 |
| 16. Mr. Alfred Rynning
Quality Source Consultants
1484 N. Kraemer Blvd.
P.O. Box 1982
Placentia, California 92670 | 1 |
| 17. Mr. John Browne
189 W. St. Charles Road
Elmhurst, Illinois 60126 | 1 |
| 18. Lt. Michael J. Browne, USN
189 W. St. Charles Road
Elmhurst, Illinois 60126 | 3 |
| 19. Ms. Drue Porter
372 A Bergin Drive
Monterey, California 93940 | 1 |

END

10-87

DTIC